# Theoretical Analysis of A Protected Superconducting Qubit

by

Feiruo Shen

A thesis
presented to the University of Waterloo
in fulfillment of the
thesis requirement for the degree of
Master of Science
in
Physics (Quantum Information)

Waterloo, Ontario, Canada, 2015

I hereby declare that I am the sole author of this thesis. This is a true copy of the thesis, including any required final revisions, as accepted by my examiners.

I understand that my thesis may be made electronically available to the public.

**Abstract**

In the past few decades, quantum computation has become an active area of research due to prospects to execute high-efficiency quantum algorithms. Quantum algorithms promise to accelerate many practical computation problems, but they can not be managed on classical computers. While a vast amount of time and effort has been invested into this field, executing a quantum algorithm is still a difficult task. One major obstacle is decoherence, which can be induced by the environment. To better protect information against noises, designs for a quantum computer have quickly improved. However, many new designs lack systematic analysis.

In the first part of the thesis, we investigate a type of superconducting-circuit-based qubit design proposed recently. The qubit, inspired by the current-mirror effect, is called the "zero-pi qubit". In Chapter 2, we derived an approximated model through concrete mathematical calculations and simulations of the zero-pi qubit. The model is concise and accurately describes the qubit system. Based on the model, we further estimate the decoherence time of the qubit. The dephasing time due to the flux noise and the charge noise exceed 40 s, and the relaxation process is well-protected against flux noise and charge noise.

In the second part of the thesis, Chapter 3, we explore the qubit control in the strong driving regime. Driving a qubit with a strong signal is an approach to shorten the operation time, thus suppressing the influence of the decoherence. We achieve strong driving condition experimentally and observe complicated qubit dynamics, which is not predicted by any conventional model. We then propose a model based on Floquet theory which accurately describes the dynamics of the qubit.

**Acknowledgements**

Firstly, I would like to express my sincere gratitude and thanks to my supervisor Prof. Lupascu for his patience, enthusiasm, as well as his encyclopedic knowledge of the field. He is an example of a prominent researcher, and always drives me to excellence.

Besides my supervisor, I would like to thank the rest of my committee: Prof. Laflamme, Prof. Mariantoni, and Prof. Wilson. They keep me on the right track and inspire me with their insightful comments and questions.

My appreciation also goes to Dr. Deng, Martin Otto, Dr. Forn-Diaz, and Muhammet Yurtalan. They are knowledgeable researchers and warm-hearted friends. Thanks for sharing those sleepless nights and hectic days before deadlines.

At last I want to thanks my parents, and Zimeng Wang. I can not imagine the world without them.

## Dedication

This thesis is dedicated to my parents.

# Table of Contents

# List of Figures

# Chapter 1

# Introduction

The development of the computer brought great changes to our lives in the 20th century. The massive capability of information processing and storage enabled by computers saves enormous time. The development of powerful computation also adds new capabilities to modern science and aids the development of high-end technologies. The computer has been improved at an exponential speed for more than a half century after its birth [1], but the demand for faster computation is continuously growing, and an alternate path has been started towards more powerful computation—quantum computers.

Before we begin the discussion on quantum computers, we will first introduce a few basic ideas about problem-solving. When we have a problem, we have an idea of its difficulty, which can be quantified by the knowledge and the time we need in finding the solution. A similar concept holds for problems for computers, where researchers use the term "complexity" instead of "difficulty". The complexity of a problem is quantified in terms of the time and resources required to solve the problem, and it scales with the problem size. For a certain set of the problems, the complexity scales exponentially with the problem size with best known algorithms run on classical computers. When the problem size grows, the complexity increases so fast that no classical computer can solve it. The strength of quantum computers is the ability to improve the scaling of certain problems with their size, and thus make them solvable.

The theory of quantum computation was initiated in early 1980s [2, 3]. The original proposal was to simulate quantum systems, which is one type of problem with a scaling law that can be greatly lowered using quantum computers. Later, more problems were discovered with a scaling law that can be improved by quantum algorithms [4, 5], which can be applied in many areas of great impact. Yet a practical quantum computer has not

been realized after 30 years of hard work. The designs of quantum computers are based on a variety of systems and their combinations [5, 6]. An example is the application of quantum information protocols using the energy levels induced in the system based on nitrogen vacancy center defects in diamond. Qubits are defined with two of these energy levels and information is propagated by emitted photons. Another example is a trapped ion quantum computer that stores quantum information in the electronic states of each ion and uses laser pulses to manipulate them. There are also many other quantum computer candidates on different physical system such as NMR, linear optics, quantum dots or the system of interest of this thesis–superconducting circuits.

In this thesis, we focus on the superconducting circuits for applications on quantum computation, which relies on fundamental quantum properties of superconducting materials. When circuit elements are carefully designed, a two-level system can be well isolated and carry one bit of quantum information, forming a qubit. Superconducting circuits have good potential for scalability [7, 8]. However, a single qubit is difficult to control. A superconducting qubit involves billions of electrons to carry the information. Such large number of particles is sensitive to environmental fluctuations caused by several sources of noise, which can erase the information in a few microseconds or even less. To mitigate the effects of noise, two strategies can be combined. On the one hand, efforts are pursued to reduce the strength of noise [9, 10] and its coupling to the qubit [11, 12]. On the other hand, the time required for qubit operations can be reduced [13, 14]. In this thesis, we present our results on both aspects by studying a protected superconducting circuit and the qubit evolution under a strong driving signal.

In the rest of this chapter the fundamental theoretical concepts are introduced, and examples of superconducting qubits are presented. In Chapter 2, a superconducting circuit called the zero-pi qubit is investigated. The design of this new qubit emphasizes the protection of the qubit states, while keeping a high anharmonicity. Its Hamiltonian and its eigenstates are studied, as well as its decoherence processes. In Chapter 3, the attention is turned to the fast qubit control. The qubit evolution under strong driving is explored. Driving a qubit strongly is a way to achieve fast quantum operations. However, the dynamics become complex and deviate significantly from typical qubit behaviour using the standard description. Under strong driving conditions, the standard description breaks down and understanding the optimal qubit operations becomes difficult. Thus, a model based on Floquet theory is built in order to describe the dynamics, and it is applied to the experimental results. In the last chapter the results are summarized and their importance as well as prospects for future research are are discussed.

## 1.1 Quantum computation

This section contains a very brief introduction to the formalism of quantum computation. A complete description can be found in [5]. Quantum computation represents information processing based on the quantum evolution of physical systems. The information in a quantum computer corresponds to the combined configuration of many two-state systems. We use $|0\rangle$ and $|1\rangle$ to represent the states of each two-state system. As any quantum states, they can be built into superpositions,

$$|\psi\rangle = \alpha\,|0\rangle + \beta\,|1\rangle\,. \tag{1.1}$$

Here, $|\psi\rangle$ is the state information stored in the qubit. The coefficients $\alpha$ and $\beta$ are complex scalars. The phase difference $\phi$ between $\alpha$ and $\beta$ is an important nonclassical channel to store information. The state is usually expressed by a vector

$$|\psi\rangle = \begin{pmatrix}\alpha\\ \beta\end{pmatrix}. \tag{1.2}$$

The basis of this representation is $\{|0\rangle\,, |1\rangle\}$.

The information manipulation is accomplished by quantum gates. In matrix form, qubit gates are represented by unitary matrices. Some commonly used qubit gates are:

1. Hadamard gate:
$$H = \frac{1}{\sqrt{2}}\begin{pmatrix}1 & 1\\ 1 & -1\end{pmatrix}. \tag{1.3}$$

2. Pauli-X, -Y, -Z gates:
$$X = \begin{pmatrix}0 & 1\\ 1 & 0\end{pmatrix}, Y = \begin{pmatrix}0 & -i\\ i & 0\end{pmatrix}, Z = \begin{pmatrix}1 & 0\\ 0 & -1\end{pmatrix}. \tag{1.4}$$

3. Phase shift gates:
$$R_\phi = \begin{pmatrix}1 & 0\\ 0 & e^{i\phi}\end{pmatrix}. \tag{1.5}$$

However, single qubit gates are not sufficient to accomplish quantum computation. Gates involving two or more qubits are required for universal quantum computation. Some commonly used multi-qubit gates are:

1. Controlled-NOT gate

$$\text{CNOT} = \begin{pmatrix} 1 & 0 & 0 & 0 \\ 0 & 1 & 0 & 0 \\ 0 & 0 & 0 & 1 \\ 0 & 0 & 1 & 0 \end{pmatrix}. \tag{1.6}$$

2. Controlled-PHASE gate

$$\text{CPHASE} = \begin{pmatrix} 1 & 0 & 0 & 0 \\ 0 & 1 & 0 & 0 \\ 0 & 0 & 1 & 0 \\ 0 & 0 & 0 & -1 \end{pmatrix}. \tag{1.7}$$

3. Control unitary gate

$$\text{C}(U) = \begin{pmatrix} 1 & 0 & 0 & 0 \\ 0 & 1 & 0 & 0 \\ 0 & 0 & u_{00} & u_{01} \\ 0 & 0 & u_{10} & u_{11} \end{pmatrix}. \tag{1.8}$$

4. The Toffoli gate

$$T = \begin{pmatrix} 1 & 0 & 0 & 0 & 0 & 0 & 0 & 0 \\ 0 & 1 & 0 & 0 & 0 & 0 & 0 & 0 \\ 0 & 0 & 1 & 0 & 0 & 0 & 0 & 0 \\ 0 & 0 & 0 & 1 & 0 & 0 & 0 & 0 \\ 0 & 0 & 0 & 0 & 1 & 0 & 0 & 0 \\ 0 & 0 & 0 & 0 & 0 & 1 & 0 & 0 \\ 0 & 0 & 0 & 0 & 0 & 0 & 0 & 1 \\ 0 & 0 & 0 & 0 & 0 & 0 & 1 & 0 \end{pmatrix}. \tag{1.9}$$

The matrix representation of the operators has dimension $d = 2^n$ where $n$ is the number of involved qubits. For those operators involving multiple qubits, we take the direct product of each qubit Hilbert space to obtain the full Hilbert space. For example, matrices with dimension 4 have basis $\{|0\rangle|0\rangle, |0\rangle|1\rangle, |1\rangle|0\rangle, |1\rangle|1\rangle\}$.

An important result in quantum computing is the Solovay-Kitaev theorem [15]. The theorem guarantees that any quantum operation on a set of qubits can be decomposed into a set of the gates presented above. We do not discuss further how to perform quantum algorithms by these quantum gates in detail. Nevertheless, we want to emphasize that quantum computer is built by many basic qubit gates. We have to make efforts to ensure that every qubit gate performs as designed.

Although we have all the ingredients to build a quantum computer, we are still far from the success because of the effect of errors. In superconducting circuits, errors can arise due to imperfect circuit fabrication, Cooper-pair number and surface spin fluctuation, quasiparticle tunneling and many other sources of noise. Each error source impacts the qubit in a particular way. Some sources cause dephasing of the qubit state, inducing the loss of the phase information $\phi$. Some sources induce relaxation processes, turning the system to the equilibrium state and erase all the information. The operations can also be affected by errors. For example, imperfect time control can lead to errors in state evolution. One systematic way to describe the error is to insert an additional term in the Hamiltonian,

$$H = H_0 + \Delta H. \tag{1.10}$$

Here, $H_0$ is the ideal Hamiltonian, and $\Delta H$ is the error term. If the qubit is a two-level system with energy gap $\Delta$, we can write the Hamiltonian in the energy eigenbasis as

$$H_0 = -\frac{\Delta}{2}\sigma_z, \tag{1.11}$$

where $\sigma_z$ is the Pauli matrix. Dephasing of the qubit is given by

$$\Delta H_{\text{dephasing}} = N_1(t)\sigma_z. \tag{1.12}$$

The function $N(t)$ is time-dependent. The noise term disturbs the energy level splitting of the qubit, thus shifting the phase of $|0\rangle$ and $|1\rangle$ after a period of time. Eventually, although the information stored in the modulus of the coefficients is unchanged, the phase information is lost. Thus this process is called dephasing process.

The other type of noise can be written as

$$\Delta H_{\text{relaxation}} = N_2(t)\sigma_x. \tag{1.13}$$

Again, $N_2(t)$ is a noisy function and $\sigma_x$ is a Pauli matrix. The operator $\sigma_x$ causes a transition between the two qubit states, thus erasing the information stored in the amplitudes of the states. This process is known as relaxation. Note that relaxation is always accompanied by the loss of phase information. The time of relaxation and dephasing are very important to characterize the decoherence process of a qubit.

## 1.2 Superconducting circuits

In this section we discuss the field of superconducting circuits. A complete review of superconductivity can be found in [16, 17]. Information about superconducting circuits and quantum electrodynamics (QED) can be found in [18].

The number of atoms in a superconducting circuit is on the order of $\sim 10^8$ or larger, and therefore it is impractical to describe the state of each atom individually. Instead, we use a macroscopic wave function [16] $\Psi(r) = |\Psi|e^{i\varphi}$ that describes the ground state of the entire system in the superconducting state. In superconducting circuits, the macroscopic phase of the wavefunction is useful to depict the dynamics of the system. Generally in any circuit it is possible to define the flux in a node from the voltage at that node by [19]

$$\Phi(t) = \int_{-\infty}^{t} V(t')\mathrm{d}t'. \tag{1.14}$$

For an isolated block of superconducting material, also known as a superconducting island, the node flux $\Phi$ can be related to the macroscopic phase of the superconductor by $\varphi = \Phi/\varphi_0$, so that the above equation can be rewritten as

$$\varphi_0\dot{\varphi} = V, \tag{1.15}$$

where $\varphi_0 = \hbar/2e$ is the reduced magnetic flux quantum with $\hbar = h/2\pi$ the reduced Planck constant.

The simplest circuit elements are the inductor $L$ and capacitor $C$. In an inductor $L$, current and flux are related by $\Phi/L = I$, while in a capacitor $C$ voltage and charge are related by $q = CV$. These equations can be written for the superconducting phase,

$$\frac{\varphi_0\varphi}{L} = \dot{q}, \tag{1.16}$$

and

$$\varphi_0\dot{\varphi}C = q. \tag{1.17}$$

The Lagrangian of an inductor and a capacitor can therefore be written as

$$\mathcal{L} = \frac{\varphi_0^2}{2C}\dot{\varphi}^2 - \frac{\varphi_0^2}{2L}\varphi^2. \tag{1.18}$$

The phase across the inductor $\varphi$ is a canonically conjugate variable to the Cooper-pair number on the capacitor $n = q/2e = \partial\mathcal{L}/\partial\hbar\dot{\varphi}$, obeying the commutation relation of conjugate operators

$$[\varphi, n] = i. \tag{1.19}$$

Another important circuit element is the Josephson junction [20]. A Josephson junction consists of two superconducting islands and a link between them. The superconductivity is weakened at the link. The suppression of superconductivity can be caused by the presence

of a non-superconducting metal, a narrowed superconducting wire, a misalignment of the superconductor crystal, among other approaches. In practice, the insulating barrier is used most commonly. This type of junction is also known as superconductor-insulator-superconductor (S-I-S) Josephson junction. Its advantages are the fabrication reliability and well-understood theory compared to the other types. The current that flows through the junction follows the first Josephson relation [20]

$$I = I_c \sin(\delta\varphi). \tag{1.20}$$

Here $I$ is the current flowing through the junction and $\delta\varphi$ is the superconducting phase difference between the two superconducting islands on each side of the junction. The critical current $I_c$ is the maximum supercurrent that can flow through the junction. When $\varphi$ is small, we can take the first order approximation of the current-phase relation

$$I = I_c \delta\varphi. \tag{1.21}$$

This shows that when the phase difference is small, the junction behaves as an inductor. However, when the phase difference increases this relation becomes non-linear. The non-linearity plays a crucial role in superconducting qubits: it breaks the harmonic levels in in a simple $LC$ circuit formed by a Josephson junction and a capacitor, therefore creating an artificial atom. Most superconducting circuits are built by inductors, capacitors, and Josephson junctions. We give examples in the next section.

## 1.3 Superconducting qubits

Superconducting circuits provide very large flexibility in designing an artificial atom. The intrinsic level splitting can be achieved in a wide range to match the designated parameters. In this section we discuss three well-established types of superconducting qubits together with their advantages and disadvantages.

### 1.3.1 The charge qubit

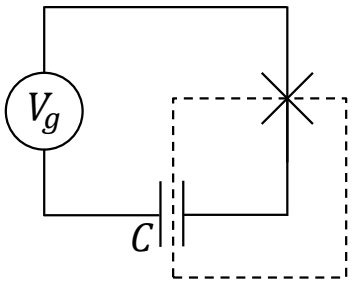


Figure 1.1: The circuit model of a charge qubit. The cross symbol represents the Josephson junction. The dashed box shows a superconducting island which is connected to the circuit through the Josephson junction and a capacitor $C$.

The charge qubit is one of the simplest superconducting qubits. It has one small superconducting island and a larger island known as the reservoir [21, 22]. The small island and the reservoir are coupled by a Josephson junction and a gate capacitor. The small island is also known as Cooper-pair-box, and the number of Cooper pairs on the island determines the qubit state. Figure 1.1 shows the circuit diagram of a charge qubit. The Hamiltonian of a charge qubit can be written as

$$H = \frac{1}{2}E_C(n - n_g)^2 - E_J \cos(\delta\varphi), \tag{1.22}$$

where $E_C$ is the capacitance energy defined as $E_C = \frac{(2e)^2}{C_J+C}$ with the parasitic capacitance of the junction $C_J$ and the capacitance of the capacitor in the circuit $C$. The Josephson energy $E_J$ is defined as $I_c\varphi_0$. The operator $n$ is the number operator of Cooper pairs. The gate charge $n_g = CV_g/2e$ represents the induced charge on the small island by the gate voltage $V_g$. The gate voltage $V_g$ consists of a static voltage and an additional noisy term, which represents the charge noise. In the charge qubit, the capacitance energy is much larger than the Josephson energy, making the Cooper-pair number a good quantum number. We plot the energy spectrum versus gate charges in figure 1.2. The circuit parameters are $E_J/h = 12.52$ GHz and $E_C/h = 226.32$ GHz, the same as the parameters in [21].

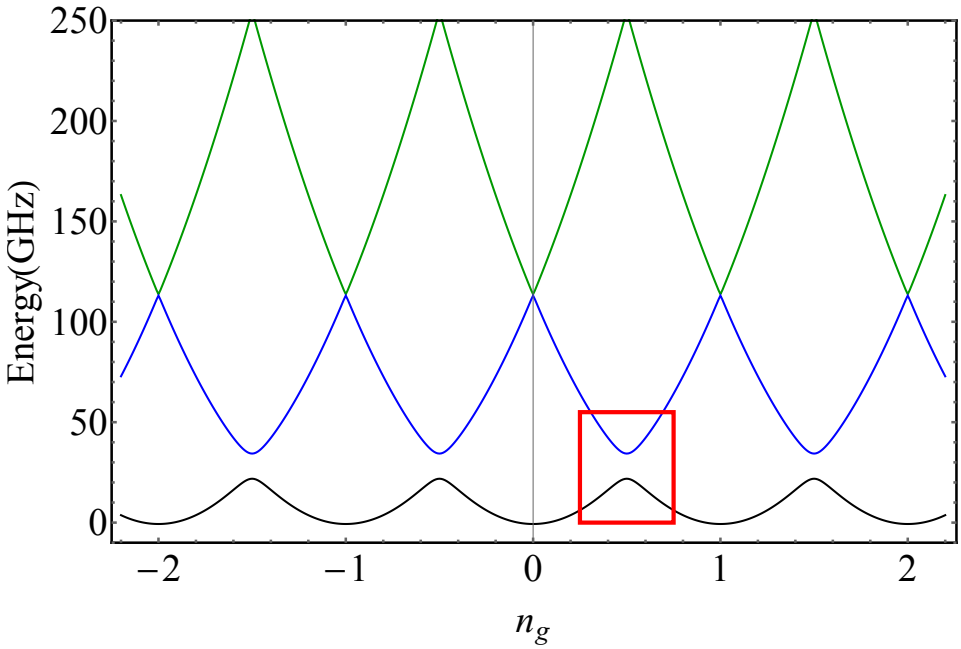


Figure 1.2: A typical energy spectrum of the charge qubit. The red box shows the qubit area, where the sensitivity to charge noise is maximally suppressed.

By varying the gate charge, the energy difference between the lowest states of the system changes. Usually, the gate charge is tuned to a half-integer, such that the energy gap is insensitive to first order to gate charge fluctuations. Assuming the gate charge is $n_g = 0.5$, the avoided-level crossing between $|n = 0\rangle$ and $|n = 1\rangle$ defines the two-level system of the qubit,

$$|0\rangle = \frac{1}{2}\left(|n = 0\rangle - |n = 1\rangle\right) \tag{1.23}$$

and

$$|1\rangle = \frac{1}{2}\left(|n = 0\rangle + |n = 1\rangle\right). \tag{1.24}$$

Although the influence of gate charge on the energy gap is eliminated to first order at $n_g = 0.5$, the fluctuation of the gate charge can still cause serious relaxation and dephasing. Koch *et al.* [11] proposed a modification of the charge qubit in which the relation of $E_C$ and $E_J$ is reversed. In this case the qubit is insensitive to the offset charge. A more detailed account of this will be given later.

### 1.3.2 The flux qubit

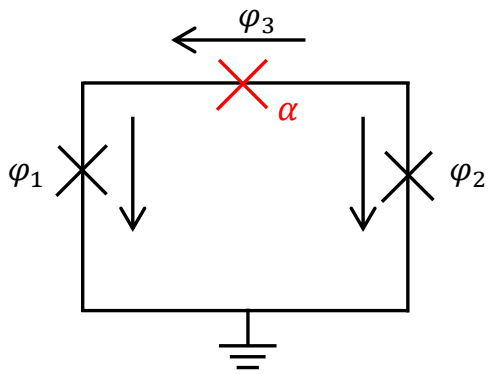


Figure 1.3: The circuit model of a flux qubit. The circuit consists of two identical junctions and an alpha junction which is plotted in red (*indicate with "$\alpha$" in the drawing which one it is*). The alpha junction differs in size to the other junctions. The arrows indicate the direction of phase drop.

A flux qubit consists of three Josephson junctions in a loop. Two junctions are identical while the third one, which is called the alpha junction, is smaller by a factor $\alpha \approx 0.8$ [23]. In contrast to the charge qubit, the Josephson energy of the junctions is larger than the charging energy thus making the phase difference across each junction a good quantum number. The Hamiltonian of the flux qubit is

$$H = \frac{1}{2}\frac{(2e)^2}{2C}\vec{P}^T M^{-1}\vec{P} + E_J\left(2+\alpha-\cos\varphi_1-\cos\varphi_2-\alpha\cos(2\pi f_x+\varphi_1+\varphi_2)\right). \quad (1.25)$$

Here, the vector $\vec{P} = (n_1, n_2)^T$, with Cooper-pair number operators $n_1$ and $n_2$, representing the Cooper pair number on junction 1 and junction 2 respectively, where $\varphi_i$ represents the phase difference across junction $i$. $f_x = \Phi_x/\varphi_0$ is the normalized applied magnetic flux. In the above equation phase quantization [16] has been applied $\varphi_\alpha = \varphi_1 + \varphi_2 + 2\pi f_x$. The matrix $M$ is determined by the ratios of the capacitances in the system:

$$M = \begin{pmatrix} 1+\alpha & -\alpha \\ -\alpha & 1+\alpha \end{pmatrix}. \quad (1.26)$$

In the Hamiltonian, $f_x$ reflects the magnetic flux penetrating the loop. We plot the potential energy as a function of $\varphi_1$ and $\varphi_2$ in figure 1.4. We use the same parameters as the circuit in [24].

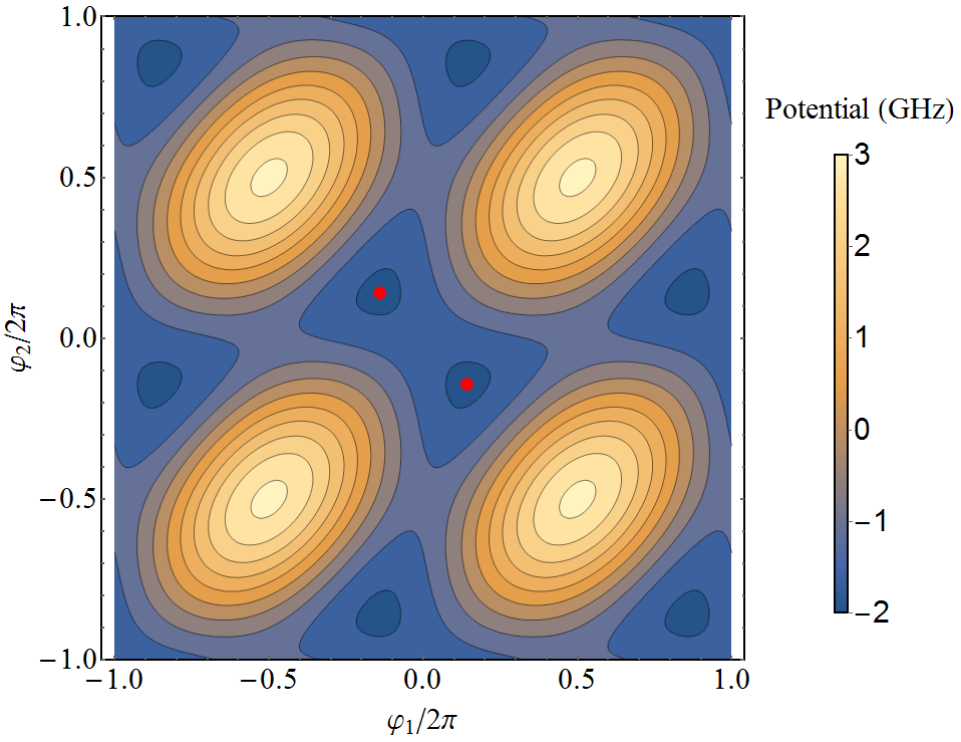


Figure 1.4: The potential energy of a flux qubit. The red dots indicate the bottom of the well.

Within each $2\pi$ period of the potential, there are two wells, and we denote the ground states as $|\uparrow\rangle$ and $|\downarrow\rangle$ for the states in the upper-left and lower-right wells respectively (*show in the plot which is which*). The eigenstates of the flux qubit correspond to superpositions of $|\uparrow\rangle$ and $|\downarrow\rangle$. State $|\uparrow\rangle$ represents current flowing clockwise in the loop, while state $|\downarrow\rangle$ represents current flowing counterclockwise. When $f_x = 0.5$ the eigenstates are $(|\uparrow\rangle \pm |\downarrow\rangle)/\sqrt{2}$ and the qubit generates no net flux. Away from $f_x = 0.5$ the system presents a non-zero current in each of its states, with opposite sign for the ground/excited state. Thus the flux qubit is also known as the persistent current qubit. The energy spectrum is plotted in figure 1.5. The circuit parameters are $E_J/h = 259$ GHz, $E_C/h = 59.2$ GHz, and $\alpha = 0.8$, the same parameters as the circuit in [24].

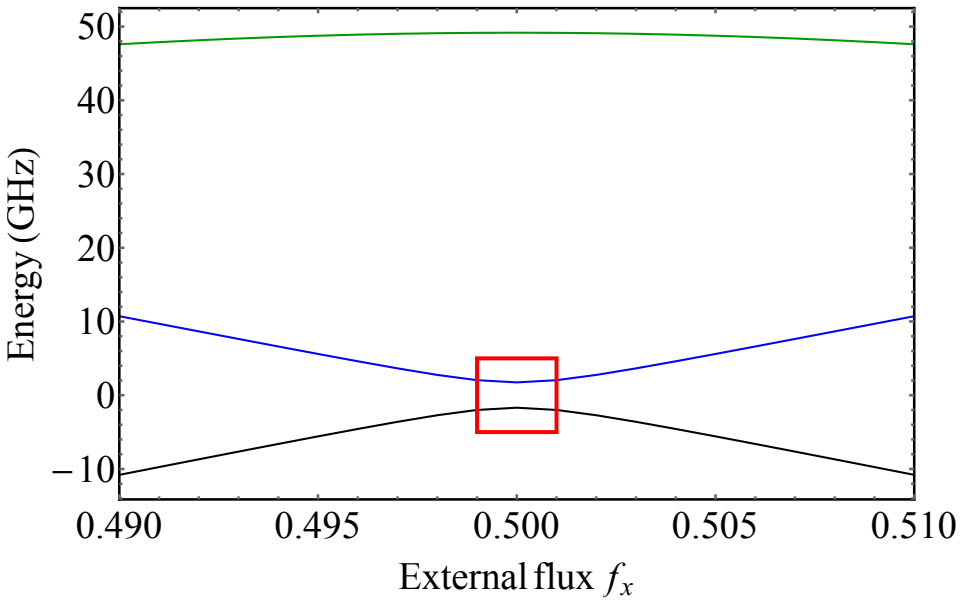


Figure 1.5: The spectrum of a flux qubit. The red box shows the symmetry point $f_x = 0.5$ and its vicinity. In this area, the energy splitting of the qubit levels has minimal sensitivity to the magnetic noise. Notice the difference in energy to the third qubit level shown in green.

The flux qubit is mostly insensitive to gate charges, but the potential energy is affected by the external magnetic flux $f_x$. The fluctuations of the flux can cause dephasing and relaxation of the qubit.

### 1.3.3 The transmon qubit

The transmon qubit is developed based on the charge qubit [11, 25]. The transmon qubit is design to be insensitive to both charge noise and flux noise. The transmon qubit shares the same circuit diagram with the charge qubit, but it decreases the ratio of $E_C/E_J$, by shunting the Josephson junction with a large capacitor. The Hamiltonian of a transmon qubit is

$$H = \frac{1}{2}E_C(n - n_g)^2 - E_J \cos\varphi. \tag{1.27}$$

Here, we have the capacitance energy $E_C = (2e)^2/(C + C_J)$, with $C$ the capacitor shunting the junction and $C_J$ the parasitic capacitor of the junction. $n$ is the number operator and

$\varphi$ the phase difference across the junction. $n_g$ is the gate charge. Because in the transmon qubit we have $E_J > E_C$, the dependence of the charge is suppressed. We plot the energy against the gate charge in figure 1.6. The circuit parameters are $E_J = 17.45/h$ GHz, $E_C/h = 3.088$ GHz, with the same parameters as [26].

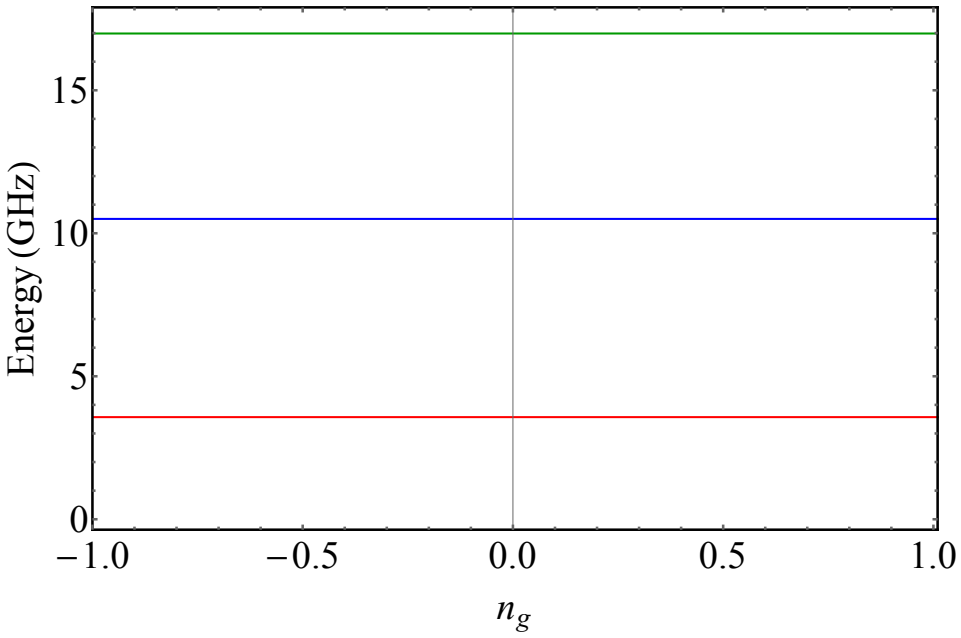


Figure 1.6: The spectrum of a transmon qubit. Compared to the spectrum in figure 1.2, the dependence on the gate charge is greatly suppressed. In other words, the qubit spectrum is insensitive to charge noise.

However, the dependence on the charge is not totally eliminated. We plot the energy difference of the ground state and the first excited state in figure 1.7

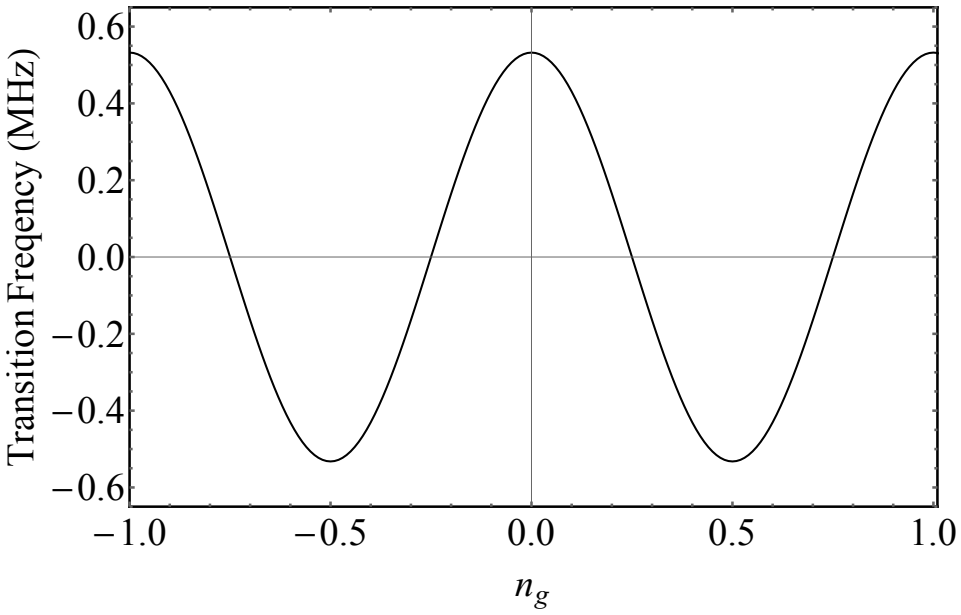


Figure 1.7: The spectrum transition frequency between the ground state and the first excited. The dependence on the gate charge is weak but not zero.

The transmon qubit is not affected by the external flux, and is mostly insensitive to the charge noise, but it is still not perfect. The increasing ratio of $E_J/E_C$ suppresses the anharmonicity of the qubit, leading to a similar energy gap between the ground state to the first excited state, and the first excited state to the second excited state. Because of the low anharmonicity, the signal which drives the transition between $|0\rangle \leftrightarrow |1\rangle$ also drives $|1\rangle \leftrightarrow |2\rangle$, leading to information loss to noncoding space. In order to suppress leakage, slow pulses with specific shapes must be applied, which require specific electronics to be generated [27]. Slow pulses also imply that qubit state control is slower and gate times are increased, reducing the efficiency of each qubit gate.

## 1.4 Noise in superconducting qubits

We have introduced several types of superconducting qubits in the previous section. We have seen that the noise is a very important factor in qubit design. Understanding the noise is important to improve the qubit performance. In this section, we introduce the charge noise and the flux noise, which are considered as two major sources of decoherence.

### 1.4.1 Charge noise

The charge distribution in a superconducting circuit can be described by a time-dependent function. However, the function fluctuates due to charge noise. The fluctuations can have a complicated form, but we usually assume it is Gaussian noise [25, 28]. Moreover, it has been observed in experiments that charge noise has a $1/f$ character [29], meaning its power spectral density is inversely proportional to frequency, $S_{\text{charge}}(f) \propto 1/f$ regardless of geometry or material.

The physics of the charge noise is not completely understood, but the model of gate charge is usually sufficient to simulate it. A superconducting device usually consists of three parts: the circuit, a layer of substrate, and a layer of ground plane. The circuit is isolated from the superconducting ground plane [25, 30], and generates a parasitic capacitance between them. In the ground plane, the charge distribution has some randomness and can attract a positive or negative charge in the nearby circuit island. This effect can lead to the charge noise we observed in the experiment.

### 1.4.2 Flux noise

If the qubit circuit has a loop, the magnetic field penetrating the loop modifies the superconducting phase due to phase quantization. The fluctuation of the magnetic flux is called flux noise. Similar to charge noise, flux noise is assumed to be Gaussian noise with $1/f$ character [31]. The origin of the flux noise is not fully understood. Some research proposed spin disorder on the superconducting surface [32] as one of the candidates to explain flux noise.

# Chapter 2

# Noise Analysis of the Zero-Pi Superconducting Qubit

In this chapter, we investigate the properties of the zero-pi superconducting qubit. The zero-pi qubit was proposed by Kitaev [33], based on the current-mirror-effect [34]. Dempster *et al.* analyzed this qubit based on numerical simulations in [35], and Brook *et al.* designed a protected qubit gate based for the zero-pi qubit [36]. The zero-pi qubit features two nearly degenerate low energy states and has good protection against charge and flux. In the original proposal, Kitaev provides a series of arguments on the robust noise protection of the zero-pi qubit [33]. Here we present an extensive analysis of the properties of the zero-pi qubit starting with the circuit model. The effective Hamiltonian for the ground state doublet is then derived using a combination of the Born-Oppenheimer approximation, tight-binding band calculations, and perturbation theory. Based on the analytic result, we investigate the role of charge and flux noise. Numerical techniques are used to verify the validity of the analytical approximations.

A full description of the zero-pi qubit relies on three degrees of freedom. One of the three is decoupled and merely two degrees of freedom are relevant. The two degrees of freedom are characterized by widely different frequencies. Therefore, we can apply the Born-Oppenheimer approximation to further eliminate a degree of freedom, which leads to a one-dimensional problem. The Schrödinger equation for the one-dimensional problem is identical to a particle in a $\pi$-periodic potential, which determines the qubit levels.

We firstly analyze the effect of gate charges coupled to the inductor in a radio-frequency superconducting quantum interference device (RF-SQUID) in Section 2.1, which provides a result important for the analysis of the zero-pi qubit. We then analyze the circuit model of

the zero-pi qubit and show that only two out of three variables are relevant in Section 2.2. Next, we use the Born-Oppenheimer approximation to obtain a one-dimensional Hamiltonian in Section 2.3 and we apply the tight-binding approximation in Section 2.4. We compare our result with numerical simulations in Section 2.5. We discuss the error contributed by the charge and the flux noises in Section 2.6. The conclusion of the work is presented in Section 2.7. A strict mathematical derivation of the Born-Oppenheimer approximation can be found in Appendices.

## 2.1 Charge noise in RF-SQUID

In this section, we discuss the dynamics of the charge noise in an inductor in an RF-SQUID circuit. The charge noise analysis for the RF-SQUID directly contributes to the later analysis on the zero-pi qubit. The model is similar to a fluxonium qubit [12], which consists of an inductively shunted Josephson junction. The qubit dynamics and noise effects for the fluxonium have been studied both theoretically and experimentally [12, 37, 38]. Here we draw attention to the mechanism of through which the charge noise coupled at different points in the inductor affects the system. This mechanism helps us understand the role played by inductors in the zero-pi qubit.

### 2.1.1 Circuit model of a single gate charge source

An RF-SQUID is a superconducting circuit consisting of a Josephson junction and an inductor. To simulate the effect of the charge noise, we couple the system to a noisy voltage source through a gate capacitor. The gate capacitor should be sufficiently small so that it does not significantly change the dynamics of the system. Since we are particularly interested in the effect of charge noise in the inductor, the attachment point of the gate capacitor is chosen in the inductor, as shown in figure 2.1. The attachment point separates the inductor into two parts, with inductances $L_1$ and $L_2$ respectively, satisfying $L_1+L_2 = L$, where $L$ is the total inductance. We define $\alpha = L_1/L$ with $0 < \alpha < 1$. The Hamiltonian, which depends on $\alpha$, is given by

$$H_\alpha = \frac{1}{2}E_C n_\varphi^2 + \frac{1}{2}E_{C_g}(n_\gamma + n_g)^2 - E_J \cos\varphi + \frac{1}{2}\frac{E_L}{\alpha}\gamma^2 + \frac{1}{2}\frac{E_L}{1-\alpha}(\varphi - f_x - \gamma)^2. \qquad (2.1)$$

Here, $\varphi$ corresponds to the superconducting phase difference on the junction and $n_\varphi = q_\varphi/2e$, with $q_\varphi$ the junction capacitor charge. They obey the canonical conjugation relation $[\varphi, n_\varphi] = i$. Another pair of canonically conjugate operators are $\gamma$ and $n_\gamma$, which are the

superconducting phase difference on $L_1$ and its canonically conjugate momentum. We also introduce the gate charge $n_g = C_g V_g/2e$ and the dimensionless external magnetic flux through the RF-SQUID loop $f_x = \Phi/(\hbar/2e)$. The four energy scales characterizing the circuit are the charging energy of junction capacitance $E_C = (2e)^2/C$, the charging energy of gate capacitor $E_{C_g} = (2e)^2/C$, the Josephson energy $E_J$, and the inductive energy $E_L = (\hbar/2e)^2/L$.

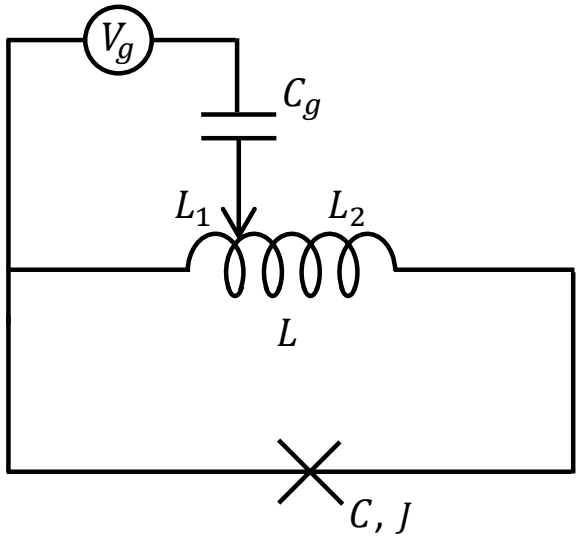


Figure 2.1: The circuit diagram of an RF-SQUID with a gate voltage coupling. The coupling point separates the inductor into two parts with inductances $L_1$ and $L_2$.

It is useful to compare the Hamiltonian in 2.1 with the Hamiltonian of an RF-SQUID without gate capacitors, given by [17]

$$H_{\text{RF-SQUID}} = \frac{1}{2}E_C n_\varphi^2 - E_J \cos\varphi + \frac{1}{2}E_L(\varphi - f_x)^2. \tag{2.2}$$

We rewrite the Hamiltonian in 2.1 as

$$H_\alpha = H_{\text{RF-SQUID}} + \frac{1}{2}E_{C_g}(n_\gamma + n_g)^2 + \frac{1}{2}\frac{E_L}{\alpha(1-\alpha)}\left(\gamma - \alpha(f_x - \varphi)\right)^2. \tag{2.3}$$

The gate charge $n_g$ and the external frustration $f_x$ are time-dependent quantities. They consist of a static term and a random term due to device noise. For example, $n_g(t) =$

$n_g(0) + \delta n_g(t)$, where $\delta n_g(t)$ is a small time-dependent fluctuation. The static part can be eliminated by the transformation $\tilde{f} = e^{-in_g\gamma} f$ and $\tilde{f}(\gamma) = f(\gamma + \alpha(f_x - \varphi))$, where $\tilde{f}$ and $f$ are the transformed and the original wavefunctions. Thus we can set $n_g(0) = 0$ and $f_x(0) = 0$, and the Hamiltonian only depends on the small fluctuations $\delta n_g(t)$ and $\delta f_x(t)$. In this section, we neglect the effect of the fluctuations. We will analyze the effect of fluctuations, using perturbation theory, in the next section.

The relation expressed in equation 2.3 shows that the Hamiltonian of the system is that of an RF-SQUID coupled to a harmonic oscillator through the superconducting phase. Moreover, because the gate capacitance is small compared to the capacitance of the junction, we are in the regime $E_{C_g} \gg E_C$, and the dynamics of $\gamma$ and $\varphi$ is therefore analog to electron-nuclear problem. The dynamics of $\gamma$ plays the role of the position of the moving electron, and $\varphi$ behaves like the nucleus. Following an approach commonly used in quantum chemistry and molecular physics, we apply the Born-Oppenheimer (BO) approximation. The key to the BO approximation is to identify a rapid part and an inertial part in the system. The rapid part remains in the instantaneous ground-state configuration scale while the inertial part barely changes. In a first step, the Schrödinger equation of the rapid part has to be solved by neglecting the kinetic energy of the inertial part. The eigenenergies to the Schrödinger equation are known as potential energy surfaces in the BO approximation. In the second step the kinetic energy of inertia part is reintroduced. Together with the potential energy surfaces, they determine the Schrödinger equation of the inertial part. More details about the approximation can be found in Appendix A, see also reference [39].

We start by introducing a basis

$$\psi_{nk}(\varphi, \gamma) = F_{nk}(\varphi) f_k(\gamma; \varphi), \tag{2.4}$$

where $\varphi$ and $\gamma$ are the variables of the inertial part and the rapid part respectively. The wavefunction $f_k(\gamma; \varphi)$ is the $k^{\text{th}}$ eigenstate of the Hamiltonian

$$H_\gamma = \frac{1}{2} E_{C_g} n_\gamma^2 + \frac{1}{2} \frac{E_L}{\alpha(1-\alpha)} \gamma^2, \tag{2.5}$$

describing the state of the rapid part, with eigenenergies $\mathcal{E}_k(\varphi)$. The Hamiltonian of the rapid part takes the form of a harmonic oscillator Hamiltonian with generalized momentum $n_\gamma$ and generalized position $\gamma$. The noise terms $n_g$ and $f_x$ do not appear in the Hamiltonian due to the transformation introduced previously. This fact dramatically simplifies the problem in the following aspects. Firstly, the matrix element $\langle f_l | O | f_k \rangle$ is independent on $\varphi$ or $n_g$ unless the operator $O$ explicitly depends on $f_x$ or $n_g$. Secondly, the spectrum of

the rapid part, i.e. $\mathcal{E}_k(\varphi)$, is independent on $\varphi$. Hence, we neglect the $\varphi$ dependence by writing the eigenenergy as a constant $\mathcal{E}_k$. The energy $\mathcal{E}_k$ is also known as an energy surface [39]. With the energy surface we can obtain the inertial part wavefunction $F_{nk}(\varphi)$, which is the $n^{\text{th}}$ eigenstate with eigenenergy $E_{nk}$ of the Hamiltonian

$$H_\varphi = H_{\text{RF-SQUID}} + \mathcal{E}_k. \tag{2.6}$$

Since $\mathcal{E}_k$ does not depend on $\varphi$, the wavefunction is $k$ independent: $|F_{nk}\rangle = |F_n\rangle$.

The basis $\{\psi_{nk}\}$ does not diagonalize the full Hamiltonian. However, we will see that the basis diagonalizes a part of the Hamiltonian and left with a term that can be treated with perturbation theory. The matrix elements of the exact Hamiltonian for states $|\psi_{ml}\rangle$ and $|\psi_{nk}\rangle$ is given by

$$\langle\psi_{ml}| H_\alpha |\psi_{nk}\rangle = E_{nk}\delta_{mn}\delta_{lk} + \langle\psi_{ml}| H_{\text{corr}} |\psi_{nk}\rangle , \tag{2.7}$$

where $\delta_{mn}$ is Kronecker delta symbol. The matrix elements of $H_{\text{corr}}$ are

$$\langle\psi_{ml}| H_{\text{corr}} |\psi_{nk}\rangle = -\frac{1}{2}E_C \left( 2 \langle F_m| \frac{\partial}{\partial\varphi} |F_n\rangle \langle f_l| \frac{\partial}{\partial\varphi} |f_k\rangle + \langle F_m|F_n\rangle \langle f_l| \frac{\partial^2}{\partial\varphi^2} |f_k\rangle \right). \tag{2.8}$$

It is straightforward to evaluate $\langle f_l| \frac{\partial}{\partial\varphi} |f_k\rangle$ and $\langle f_l| \frac{\partial^2}{\partial\varphi^2} |f_k\rangle$ by replacing $\partial_\varphi$ by $\alpha\partial_\gamma = i\alpha n_\gamma$. Nevertheless, before the calculation we can tell $\langle f_l| \frac{\partial}{\partial\varphi} |f_k\rangle$ and $\langle f_l| \frac{\partial^2}{\partial\varphi^2} |f_k\rangle$ are $n_g$ independent, and $|F_n\rangle$ are also $n_g$ independent. Consequently, $H_{\text{corr}}$ determines a $n_g$-independent correction to the full Hamiltonian. In other words, the static charge offset does not modify the energy spectrum. We conclude that the energy spectrum of an RF-SQUID is invariant with respect to different static offset charge on the inductor. However, we can not conclude anything about the non-static gate charge effect. In fact, in the next subsection we will see that the dynamical effect of charge noise is important.

Note that introducing the gate capacitor *does* change the energy spectrum, as $H_{\text{corr}}$ is non-zero. This contribution scales with the gate of capacitance and, therefore, it can be neglected.

### 2.1.2 Dynamics of charge noise

The static offset charge has no influence the spectrum. However, the dynamics of the charge noise stimulate transitions between different levels and causes energy relaxation and dephasing. The transition rate between different states induced by charge noise can be

calculated using time-dependent perturbation theory. The theory is introduced in many textbooks, see for example [40]. We start by rewriting the full Hamiltonian in 2.1 as a function of $n_g(t)$:

$$H_\alpha(n_g) = H_\alpha(0) + H_t(n_g). \tag{2.9}$$

Here, we set the offset charge at time $t = 0$ to be $n_g(0) = 0$ to simplify the calculation, and define $H_t(n_g) = E_{C_g} n_\gamma n_g$. A nonzero offset charge at time $t = 0$ can be eliminated by a gauge transformation $\tilde{\psi} = e^{-in_g(0)\gamma}\psi$. The term $E_{C_g} n_g^2/2$ is neglected since it gives a uniform energy shift and does not change the dynamics of the system.

Before applying time-dependent perturbation theory, we derive the wavefunctions in the Born-Oppenheimer approximation. It is convenient to introduce two quantities: $D_\varphi^{mn} = \langle F_m | \frac{\partial}{\partial\varphi} | F_n \rangle$ and $\beta = \frac{E_L}{\alpha(1-\alpha)E_{C_g}}$. The eigenenergies of $H_\gamma$, which are defined by equation 2.5, can be thus given by $E_{C_g}\beta^{\frac{1}{2}}$. The ground state up to the first order correction is

$$|\Psi_0\rangle \approx |\psi_{00}\rangle + \sum_{nk} \frac{\langle \psi_{nk}| H_{\text{corr}} |\psi_{00}\rangle}{E_{00} - E_{nk}} |\psi_{nk}\rangle \tag{2.10}$$

$$= |\psi_{00}\rangle - E_C \left( \sum_{n\geq 0} \frac{\sqrt{2}}{2} \frac{\alpha\beta^{\frac{1}{4}} D_\varphi^{n0} |\psi_{n1}\rangle}{E_{n1} - E_{00}} + \frac{\sqrt{2}}{4} \frac{\alpha^2\beta^{\frac{1}{2}} |\psi_{02}\rangle}{E_{00} - E_{02}} \right), \tag{2.11}$$

where $|\psi_{nk}(\varphi,\gamma)\rangle = |F_{nk}(\varphi)\rangle |f_k(\gamma;\varphi)\rangle$ are the basis states we used in the previous section (see equation 2.4). The validity of the approximation is guaranteed by the smallness of the correction coefficients,

$$\frac{\alpha\beta^{\frac{1}{4}}}{E_{n1} - E_{00}} \leq \frac{\alpha E_C}{E_{C_g}\beta^{\frac{1}{2}}} = \left( \frac{\alpha^5(1-\alpha)E_C^4}{E_{C_g}^3 E_L} \right)^{\frac{1}{4}} \ll 1, \tag{2.12}$$

and

$$\frac{E_C\alpha^2\beta^{\frac{1}{2}}}{E_{00} - E_{02}} = \frac{\alpha^2 E_C}{2E_{C_g}} \ll 1. \tag{2.13}$$

Here, we use the relation $E_{C_g} \gg E_C$ and $E_{C_g}/E_C > E_C/E_L$ based on the general consideration that $C_g$ is sufficiently small. Similarly, the corrected wavefunction of the first excited state is given by

$$|\Psi_1\rangle \approx |\psi_{10}\rangle - E_C \left( \sum_{n\geq 0} \frac{\sqrt{2}}{2} \frac{\alpha\beta^{\frac{1}{4}} D_\varphi^{n0} |\psi_{n1}\rangle}{E_{n1} - E_{10}} + \frac{\sqrt{2}}{4} \frac{\alpha^2\beta^{\frac{1}{2}} |\psi_{12}\rangle}{E_{10} - E_{12}} \right). \tag{2.14}$$

The energies up to the first order correction are

$$E_0 = E_{00} + \langle \psi_{00} | H_{\text{corr}} | \psi_{00} \rangle = E_{00} + \frac{E_C}{4} \alpha^2 \beta^{\frac{1}{2}}, \tag{2.15}$$

$$E_1 = E_{10} + \langle \psi_{10} | H_{\text{corr}} | \psi_{10} \rangle = E_{10} + \frac{E_C}{4} \alpha^2 \beta^{\frac{1}{2}}, \tag{2.16}$$

where we denote the ground energy by $E_0$ and the energy of first excited state by $E_1$.

We then apply the time-dependent perturbation to the system. Assume the initial state is the ground state $|\Psi(0)\rangle = |\Psi_0\rangle$. At time $t$ and to the first order, the transition probability from $|\Psi_0\rangle$ to the first excited state $|\Psi_1\rangle$ is given by,

$$p_{01} = |\langle \Psi_1 | U_1(t) | \Psi_0 \rangle|^2 , \tag{2.17}$$

where $U_1(t)$ is the first term of Dyson series [40] $U_1(t) = -iE_{C_g} \int e^{iH_0 t} n_\gamma e^{-iH_0 t} n_g dt$. Neglecting the second and higher orders of $\frac{E_C}{E_{C_g}}$ in the result, we obtain

$$p_{01} = \left| \alpha E_C D_\varphi^{01} \int e^{i(E_1 - E_0)t} n_g(t) dt \right|^2 . \tag{2.18}$$

This is the expression describing the dynamical effect of the charge noise. This expression shows that the dynamical effect of the charge noise in the inductor is equivalent to the dynamical effect of charge noise on the island suppressed by a factor $\alpha$. When $\alpha = 1$, the expression reduces to the island coupled case as expected. Note that the conclusion does not depend on the specific form of the wavefunction $|F_n(\varphi)\rangle$. Hence the conclusion is also valid if we replace the Josephson junction with other systems.

### 2.1.3 Linearity

To better model the charge noise, we analyze the case where the system is coupled to multiple charge noise sources. Generally all charge noise sources must be calculated simultaneously. In this section, we prove that the effect of multiple noise sources can be calculated is combined in a linear fashion. Therefore, one representative noise source is sufficient for the analysis. We consider a model with two gate charge sources, as shown in 2.2.

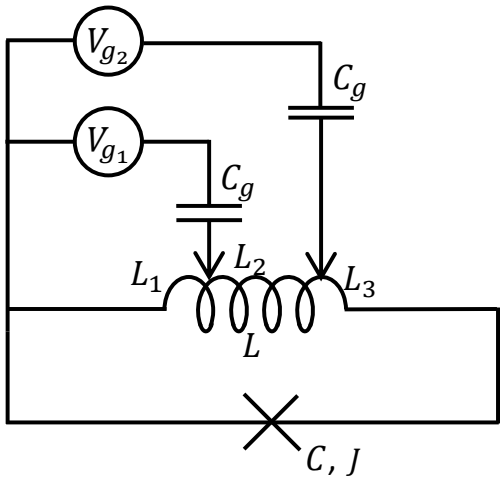


Figure 2.2: The circuit diagram of an RF-SQUID with two coupled gate voltage sources. The coupling points separate the inductor into three parts.

The Hamiltonian of the system is,

$$H = H_{\text{RF-SQUID}} + \frac{1}{2}E_{C_g}\left((n_{\gamma_1} - n_{g,1})^2 + (n_{\gamma_2} - n_{g,2})^2\right) + \\ + \frac{1}{2}E_L\left(\frac{\gamma_1^2}{\alpha_1} + \frac{(\gamma_1 - \gamma_2)^2}{\alpha_2 - \alpha_1} + \frac{(\gamma_2 - (\varphi - f_x))^2}{1 - \alpha_2} - (\varphi - f_x)^2\right). \quad (2.19)$$

The key to our analysis is finding a away to decouple the variables. We apply the transformation $\{\gamma_1, \gamma_2\} \to \{x_1, x_2\}$ such that $x_1$ and $x_2$ are decoupled. To find out the proper transformation, we write the quadratic phases terms in matrix form,

$$\frac{\gamma_1^2}{\alpha_1} + \frac{(\gamma_1 - \gamma_2)^2}{\alpha_2 - \alpha_1} + \frac{(\gamma_2 - (\varphi - f_x))^2}{1 - \alpha_2} - (\varphi - f_x)^2 = \vec{v}^T M \vec{v}, \quad (2.20)$$

where $\vec{v} = (\gamma_1, \gamma_2, \varphi - f_x)^T$ and

$$M = \begin{pmatrix} \frac{1}{\alpha_1} + \frac{1}{\alpha_2 - \alpha_1} & -\frac{1}{\alpha_2 - \alpha_1} & 0 \\ -\frac{1}{\alpha_2 - \alpha_1} & \frac{1}{1-\alpha_2} + \frac{1}{\alpha_2 - \alpha_1} & -\frac{1}{1-\alpha_2} \\ 0 & -\frac{1}{1-\alpha_2} & \frac{\alpha_2}{1-\alpha_2} \end{pmatrix}. \quad (2.21)$$

We select the new basis $\{x_1, x_2\}$ such that it diagonalize the upper-left $2 \times 2$ subspace with eigenvalues $\lambda_1$ and $\lambda_2$. For simplicity we define $\theta = \cot^{-1}\left(\frac{1}{2}\left(\frac{\alpha_2}{\alpha_1} - \frac{1-\alpha_1}{1-\alpha_2}\right)\right)$. Then we

can write the new basis as $x_1 = \gamma_1 \cos(\theta/2) - \gamma_2 \sin(\theta/2)$ and $x_2 = \gamma_1 \sin(\theta/2) + \gamma_2 \cos(\theta/2)$. The variables in the new basis are decoupled from each other while they both couple to $\varphi$. Following the same procedure as in the previous section based on time-dependent perturbation, we obtain the transition probability for two noise sources, given by

$$p_{01} = \left| E_C D_\varphi^{01} \int e^{i(E_1 - E_0)t} \left( \frac{\sin(\theta/2)}{\lambda_1(1-\alpha_2)} n_{g,x_1} - \frac{\cos(\theta/2)}{\lambda_2(1-\alpha_2)} n_{g,x_2} \right) dt \right|^2, \tag{2.22}$$

where $n_{g,1} = n_{\gamma,1} \cos(\theta/2) - n_{\gamma,2} \sin(\theta/2)$ and $n_{g,2} = n_{\gamma,1} \sin(\theta/2) + n_{\gamma,2} \cos(\theta/2)$ are transformed gate charges. Through some tedious but straightforward calculations, we find that these two noise source are combined linearly:

$$p_{01} = \left| E_C D_\varphi^{01} \int e^{i(E_1 - E_0)t} \left( \alpha_1 n_{g,1} + \alpha_2 n_{g,1} \right) dt \right|^2. \tag{2.23}$$

The linearity of the combined effect for more than two sources can be proved along the same lines.

In this section we proved that static charge noise does not affect the system, and the dynamical effect the charge noise is equivalent to the charge noise on the island with a suppression factor $\alpha$. Moreover, independent sources can be added linearly.

## 2.2 Circuit analysis of the zero-pi qubit

In this section we develop the circuit model of the zero-pi qubit. We will discuss the dynamics of the zero-pi qubit and the protection against the charge and flux noises. A good way to visualize the circuit is to place each circuit element on the edge of a tetrahedron figure 2.3. The circuit consists of a pair of identical Josephson junctions, a pair of identical capacitors, and a pair of identical inductors. The elements in each identical pair are on the opposite edges of the tetrahedron. When the system is in its ground state doublet space, the superconducting phase difference of the ends of each edges with the capacitor is a superposition of 0 or $\pi$. This is also why the qubit is called "zero-pi qubit". The zero-pi qubit is interesting for two reasons. Firstly, it was predicted that the zero-pi qubit has a high immunity to noise [35, 33]. Secondly, the possibility exist to implement protected quantum gates [36]. These properties are very important for building reliable qubits.

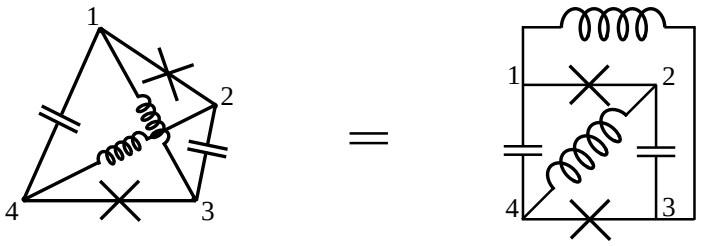


Figure 2.3: The circuit diagram of a zero-pi qubit, including a tetrahedron style (left) and a plain style (right).

To develop a systematic theory of the zero-pi qubit, we begin with the standard circuit model. We will keep as much as possible the same notion as in the previous sections. Definitions will be given for symbols that have different meaning. We label the nodes as 1,2,3,4 taken in clockwise orientation, see figure 2.3. Then we denote the superconducting phase on each node by $\varphi_j$, where $j = 1, ..., 4$. However, because only the difference of the phases is relevant, the number of degrees of freedom is three. One of the variable depends on the other three variables, but we will only discard it after the transformation. To model the charge noise effect we couple nodes 2, 3, 4 with gate voltages and gate capacitors. We can express the kinetic and potential contributions to the Lagrangian as

$$\begin{aligned} T = \frac{\varphi_0^2}{2}\left(C_J\left((\dot{\varphi}_1-\dot{\varphi}_2)^2+(\dot{\varphi}_4-\dot{\varphi}_3)^2\right)+C_0\left((\dot{\varphi}_4-\dot{\varphi}_1)^2+(\dot{\varphi}_3-\dot{\varphi}_2)^2\right)\right) \\ +\frac{C_g}{2}\left((\varphi_0(\dot{\varphi}_2-\dot{\varphi}_1)-V_{g_2})^2+(\varphi_0(\dot{\varphi}_3-\dot{\varphi}_1)-V_{g_3})^2+(\varphi_0(\dot{\varphi}_4-\dot{\varphi}_1)-V_{g_4})^2\right) \end{aligned} \quad (2.24)$$

and

$$\begin{aligned} V = -E_J(\cos(\varphi_2-\varphi_1)+\cos(\varphi_3-\varphi_4)) \\ +\frac{1}{2}E_L\left((\varphi_4-\varphi_2-f_x-\delta f_x)^2+(\varphi_1-\varphi_3-f_x/2+\delta f_x)^2\right) \end{aligned} \quad (2.25)$$

respectively. Here, we focus on the ideal symmetric circuit. The effect of disorder on the circuit elements is discussed in [35]. In the kinetic part $T$, the three capacitances are the parasitic capacitor of Josephson junctions $C_J$, the capacitors in the circuit $C_0$, and the gate capacitors $C_g$. The reduced dimensionless flux quantum is denoted by $\varphi_0 = \hbar/2e$. In the potential part $V$, the two energy scales are the Josephson energy $E_J$ and the inductive energy $E_L = \varphi_0^2/L$, where $L$ is the inductance of each inductor. The external magnetic flux

penetrating the loop is $\Phi_x$. In the following we will express the external flux as $\Phi_x = 2f_x\varphi_0$, with $f_x$ a reduced flux variable accounting for the flux through half of the loop formed of the two Josephson junctions and the two inductors.

The next step is to apply the transformation,

$$\gamma_+ = \frac{1}{2}\left(\varphi_1 - \varphi_2 - \varphi_3 + \varphi_4\right), \tag{2.26}$$

$$\gamma_- = \frac{1}{2}\left(\varphi_1 - \varphi_2 + \varphi_3 - \varphi_4\right), \tag{2.27}$$

$$\gamma_{\mathrm{ho}} = \frac{1}{2}\left(\varphi_1 + \varphi_2 - \varphi_3 - \varphi_4\right), \tag{2.28}$$

$$\gamma_{\mathrm{re}} = \frac{1}{2}\left(\varphi_1 + \varphi_2 + \varphi_3 + \varphi_4\right). \tag{2.29}$$

The subscript "ho" stands for "harmonic oscillator", "re" stands for redundant. Their meaning will be clarified shortly. We express the transformed $T$ in the matrix form,

$$T = \varphi_0^2 \dot{\vec{\gamma}}^T C \dot{\vec{\gamma}} + \varphi_0 \dot{\vec{\gamma}}^T S \vec{V_g}, \tag{2.30}$$

where $\vec{\gamma} = (\gamma_+, \gamma_-, \gamma_{\mathrm{ho}})^T$ and $\vec{V_g} = (V_{g2}, V_{g2}, V_{g3})^T$. The matrices are,

$$C = \begin{pmatrix} C_J & & \\ & C_J + C_0 & \\ & & C_0 \end{pmatrix} + C_g \begin{pmatrix} 1 & 1 & 0 \\ 1 & 1 & 1 \\ 0 & 1 & 1 \end{pmatrix}, \tag{2.31}$$

and

$$S = C_g \begin{pmatrix} 1 & 1 & 0 \\ 1 & 0 & 1 \\ 0 & 1 & 1 \end{pmatrix}. \tag{2.32}$$

With this transformation, the potential energy becomes

$$V = -2E_J\left(\cos\gamma_- \cos\gamma_+\right) + E_L\left((\gamma_+ - f_x)^2 + \gamma_{\mathrm{ho}}^2\right). \tag{2.33}$$

We clearly see that the variable $\gamma_{\mathrm{re}}$ is the redundant variable which is decoupled from the system. Three degrees of freedom are left. We keep using the matrix form and calculate the vector of conjugate operators $\vec{P_\gamma} = (p_+, p_-, p_{\mathrm{ho}})^T$, with

$$\vec{P_\gamma} = \frac{\partial L}{\partial \dot{\vec{\varphi}}} = 2\varphi_0^2 C \dot{\vec{\gamma}} + \varphi_0 S \dot{\vec{V_g}}, \tag{2.34}$$

from which we can determine the Hamiltonian of the zero-pi qubit, given by

$$H = \frac{1}{4\varphi_0^2}(\vec{P}_\gamma - \varphi_0 S\vec{V}_g)^T C^{-1}(\vec{P}_\gamma - \varphi_0 S\vec{V}_g) - 2E_J \cos\gamma_- \cos\gamma_+ + E_L\left((\gamma_+ - f_x)^2 + \gamma_{\text{ho}}^2\right). \tag{2.35}$$

Because we have assumed that $C_g$ is small compared with the capacitances in the system, we simply omit its correction to the capacitance matrix. Moreover, we define $E_{C_0} = (2e)^2/C_0$, $E_{C_J} = (2e)^2/C_J$. Note that our definition has a factor of $1/8$ difference from a more commonly used definition of the charging energy, $E_C' = e^2/(2C)$. Then we rewrite the Hamiltonian as,

$$\begin{aligned} H = {} & \frac{1}{4}E_{C_J}(n_+ - n_{g_2} - n_{g_3})^2 + \frac{1}{4}\frac{E_{C_J}E_{C_0}}{E_{C_J}+E_{C_0}}(n_- - n_{g_2} - n_{g_4})^2 \\ & + E_L(\gamma_+ - f_x)^2 - 2E_J\cos\gamma_-\cos\gamma_+ + \frac{1}{4}E_{C_0}(n_{\text{ho}} - n_{g_3} - n_{g_4})^2 + E_L\gamma_{\text{ho}}^2, \end{aligned} \tag{2.36}$$

where $n_\alpha = p_\alpha/(\varphi_0 2e)$ with $\alpha = \{+, -, \text{ho}\}$. Specifically, $n_+$ stands for the difference of Cooper pair numbers of islands $2, 3$ and $1, 4$, $n_-$ stands for the difference of islands $1, 3$ and $2, 4$, and $n_{\text{ho}}$ stands for the difference of islands $1, 2$ and $3, 4$. The gate charge is denoted by $n_{g_j} = -V_{g_i}C_g/2e$ where $j = 2, 3, 4$.

The Hamiltonian can be separated into two parts. One part involves merely variables $\gamma_-$ and $\gamma_+$; the other part is a harmonic oscillation with of $\gamma_{\text{ho}}$. The $\gamma_{\text{ho}}$ part captures the resonance frequency of the LC circuit of the inductors and the capacitors and is decoupled to the rest part of the system. The $\gamma_-$ and $\gamma_+$ part is where the qubit levels emerge and we will analyze in the next sections. For convenience we define the part of the transformed Hamiltonian related to $\gamma_-$ and $\gamma_+$ as

$$H_{+-} = \frac{1}{4}E_{C_J}(n_+ - n_{g+})^2 + \frac{1}{4}E_{C_-}(n_- - n_{g-})^2 + E_L(\gamma_+ - f_x)^2 - 2E_J\cos\gamma_-\cos\gamma_+, \tag{2.37}$$

where $n_{g+} = n_{g_2} + n_{g_3}$ and $n_{g-} = n_{g_2} + n_{g_4}$, and $E_{C_-} = \frac{E_{C_J}E_{C_0}}{E_{C_J}+E_{C_0}}$.

## 2.3 Born-Oppenheimer Approximation

Starting with this section we study the energy spectrum and wavefunctions of the lowest levels of the Hamiltonian $H_{+-}$ given in equation 2.37. The approach relies on exploiting the relation between the different energy scales in the problem for a good approximation to the solutions. In this section we show that the Born-Oppenheimer approximation results

in a one-dimensional problem. Next we us perturbation theory to derive the key properties of the system. In the next section we will focus on the one-dimensional problem resulting after we apply the BO approximation.

The circuit of the zero-pi qubit has have large inductors, large capacitors, and small Josephson junctions. Their energy scales satisfy the relation $E_{C_J} \gg E_J \gg E_L, E_{C_0}$. The kinetic energy of $\gamma_+$, which is $E_{C_J}/2$, is much larger than the kinetic energy of $\gamma_-$, which is $E_{C_-} \approx E_{C_0}$. Therefore it is suitable to apply the Born-Oppenheimer approximation. We treat the $\gamma_+$ part as the rapid part in the Born-Oppenheimer approximation. We take $\gamma_-$ as a parameter and solve the Schrödinger equation of $\gamma_+$. With the eigenenergies $\mathcal{E}_k(\gamma_-)$, which are also known as the energy surfaces, the problem reduces to a one-dimensional problem. More details of the Born-Oppenheimer approximation can be found in Appendix A and [39]. Following the steps in the recipe discussed in the appendix, we choose the basis

$$\Psi_{nk}(\gamma_+, \gamma_-) = \psi_{nk}(\gamma_-) f_k(\gamma_+; \gamma_-), \tag{2.38}$$

where the wavefunctions $f_k(\gamma_+; \gamma_-)$ describes the rapid part as a function of $\gamma_+$. The variable $\gamma_-$ enters these functions as a parameter. The wavefunctions $\psi_{nk}(\gamma_-)$ describes the inertial part. The rapid part wavefunctions are defined as the eigenstates of the Hamiltonian

$$H_+ = \frac{1}{4} E_{C_J} (n_+ - n_{g+})^2 + E_L (\gamma_+ - f_x)^2 - (2E_J \cos\gamma_-) \cos\gamma_+. \tag{2.39}$$

The eigenenergy corresponding to the state $k$ is $\mathcal{E}_k(\gamma_-)$. The wavefunctions of the inertial part are the eigenstates of the Hamiltonian

$$H_- = \frac{1}{4} E_{C_-} (n_- - n_{g-})^2 + \mathcal{E}_k(\gamma_-), \tag{2.40}$$

with eigenenergies given $E_{nk}$. The basis 2.38 diagonalizes only a part of the full Hamiltonian. However, we are content to drop the reminder of the Hamiltonian because the corrections are negligible. We will come back to a discussion of the corrections after the analysis of the wavefunctions. Nevertheless, for completeness we give the matrix representation for the dropped terms in the Hamiltonian here:

$$\langle \Psi_{ml} | H_{\text{drop}} | \Psi_{nk} \rangle = -\frac{E_{C_-}}{4} \left( 2 \langle \psi_{ml} | \langle f_l | \frac{\partial}{\partial \gamma_-} | f_k \rangle \frac{\partial}{\partial \gamma_-} | \psi_{nk} \rangle + \langle \psi_{ml} | \langle f_l | \frac{\partial^2}{\partial \gamma_-^2} | f_k \rangle | \psi_{nk} \rangle \right). \tag{2.41}$$

A detailed derivation of the dropped Hamiltonian can be found in appendix A. Next we apply perturbation theory on the Hamiltonian in equation 2.39 to obtain the approximation of the wavefunction $f_k(\gamma_+; \gamma_-)$. We represent the wavefunctions in Fock basis $\{|n\rangle\}$, which

contains the eigenstates of the Hamiltonian $H = \frac{1}{4}E_{C_J}(n_+ - n_{g+})^2 + E_L(\gamma_+ - f_x)^2$. For simplicity we define $\hbar\omega_c = \sqrt{E_{C_J}E_L}$ and $A = (E_{C_J}/E_L)^{1/4}/2$. We can express the operators $\gamma_+$ and $n_+$ by the ladder operators in the Fock basis

$$\gamma_+ - f_x = A(a + a^\dagger) \tag{2.42}$$

$$n_+ - n_{g+} = i\frac{A}{2}(a^\dagger - a). \tag{2.43}$$

We next rewrite the Hamiltonian in the Fock representation:

$$H_+ = \hbar\omega_c a^\dagger a - E_J \cos\gamma_-(D(iA)e^{if_x} + D(-iA)e^{-if_x}). \tag{2.44}$$

Here, we used the equation $\cos\gamma_+ = (e^{\gamma_+} + e^{-\gamma_+})/2$ and $D(\alpha)$ is the displacement operator defined by $D(\alpha) = \exp(\alpha a - \alpha^* a^\dagger)$. The displacement operator is an unitary operator and obeys $D(\alpha)D(\alpha)^\dagger = 1$. When a displacement operator acting on a Fock state gives a displaced Fock state [41]:

$$D(\alpha)\left|n\right\rangle = \left|n,\alpha\right\rangle = \sum_{m=0}^{\infty}\left(\frac{n!}{m!}\right)^{\frac{1}{2}}\alpha^{m-n}e^{-\frac{|\alpha|^2}{2}}\mathcal{L}_n^{m-n}\left|m\right\rangle, \tag{2.45}$$

where $\mathcal{L}_m^n(x)$ are the associate Laguerre polynomials, see [42]. In equation 2.44 a constant term has been omitted. The first term is diagonal in the Fock basis, while the second term leads to non-zero off-diagonal terms as well as corrections to the diagonal terms. We treat the second term as a perturbation to the first term. Since we are only concerned with the the lowest orders corrections to the ground state, the validity of the perturbation is verified by the smallness of first order correction on the state, which we will discuss in the following derivations. Before doing the calculation, we write the Hamiltonian in a compact form as

$$H_+ = H_+^{(0)} + g(\gamma_-)V_+, \tag{2.46}$$

where $H_+^{(0)} = \omega_c a^\dagger a$ is the zero-th order Hamiltonian, $g(\gamma_-) = -E_J\cos\gamma_-$, and $V = D(iA)e^{if_x} + D(-iA)e^{-if_x}$. Moreover, we denote the $i^{\text{th}}$ order correction to $|k\rangle$ in the wavefunction as $|k^{(i)}\rangle$, and the corresponding order correction to the energy as $E_k^{(i)}$. The first order correction to the ground state energy is

$$E_0^{(1)} = g(\gamma_-)\left\langle 0^{(0)}\right| V_+ \left|0^{(0)}\right\rangle = -2g(\gamma_-)\cos f_x e^{-\frac{A^2}{2}}, \tag{2.47}$$

where we used the property of the displacement operator in equation 2.45. Based on the same property, the first order correction to the ground state wavefunction is

$$\left|0^{(1)}\right\rangle = \sum_{n=1}^{\infty}\frac{\left\langle n^{(0)}\right| V \left|0^{(0)}\right\rangle}{E_0^{(0)} - E_n^{(0)}}\left|n^{(0)}\right\rangle = -\frac{2g(\gamma_-)}{\hbar\omega_c}\sum_{n=1}^{\infty}\cos\left(\frac{n\pi}{2} + f_x\right)\frac{e^{-\frac{A^2}{2}}A^n}{n\sqrt{n!}}\left|n^{(0)}\right\rangle. \tag{2.48}$$

Next we calculate the second order correction on the energy, given by

$$E_0^{(2)} = \langle 0^{(0)}| V_+ |0^{(1)}\rangle = -\frac{4g(\gamma_-)^2}{\hbar\omega_c}\sum_{n=1}^{\infty}\cos^2\left(\frac{n\pi}{2}+f_x\right)\frac{e^{-A^2}A^{2n}}{n\cdot n!}. \tag{2.49}$$

The series can be simplified to a compact form using Mathematica symbolic calculation [43]:

$$E_0^{(2)} = -\frac{2g(\gamma_-)^2}{\hbar\omega_c}e^{-A^2}\left(2\cos^2\varphi(\gamma_{\text{Eu}}+2\log(A)) + \Re(\Gamma(0,-A^2)+\cos(2f_x)\Gamma(0,A^2))\right), \tag{2.50}$$

where the Euler constant $\gamma_{\text{Eu}} \approx 0.577$, and the incomplete gamma function is defined as [44]

$$\Gamma(a,x) \equiv \int_x^{\infty} t^{a-1}e^{-t}dt. \tag{2.51}$$

In the regime of large $A$, the factor $e^{-A^2}$ leads to a significant suppression of $E_0^{(2)}$. In the bracket, we can safely omit the terms that are in the order of $\mathcal{O}(\log(A))$ or less. As a result, the main contribution to $E_0^{(2)}$ is $2g(\gamma_-)^2e^{-A^2}\Re(\Gamma(0,-A^2))/\hbar\omega_c$. A good estimation on the incomplete gamma function is given by

$$\Re(\Gamma(0,-A^2)) = -\int_{-A^2}^{\infty}\frac{e^{-t}}{t}dt = -\int_0^{\infty}e^{A^2}\frac{e^{-u}}{u+A^2}du \approx -\frac{e^{A^2}}{A^2}. \tag{2.52}$$

Accordingly we estimate

$$E_0^{(2)} \approx -\frac{2g(\gamma_-)^2}{\hbar\omega_c A^2} = -\frac{8E_J^2}{E_{C_J}}\cos^2\gamma_-. \tag{2.53}$$

The estimation can be used for a quick rough calculation. For the comparison with the simulation in section 2.5 we keep using equation 2.50. The first and the second order energy corrections are sufficient for the further analysis. Nevertheless, we continue to the second order state correction and the third order energy correction for a better understanding of the system. The second order correction of the state is formally given by

$$|0^{(2)}\rangle = \sum_{n=1}^{\infty}\frac{|n^{(0)}\rangle}{E_0^{(0)}-E_n^{(0)}}\left(\langle n^{(0)}| V_+ |0^{(1)}\rangle + E_0^{(1)}\langle n^{(0)}|0^{(1)}\rangle\right) - \frac{1}{2}\langle 0^{(1)}|0^{(1)}\rangle|0^{(0)}\rangle. \tag{2.54}$$

We now evaluate the first term in the bracket:

$$\begin{aligned}
&\langle n^{(0)}|\, V_+ \,|0^{(1)}\rangle \qquad (2.55)\\
&= \sum_{m=1}^{\infty} \frac{1}{E_0^{(0)} - E_m^{(0)}} \langle n^{(0)}|\, V_+ \,|m^{(0)}\rangle \langle m^{(0)}|\, V_+ \,|0^{(0)}\rangle \\
&= -\sum_{m=1}^{\infty} \frac{1}{\hbar\omega_c m} \left(e^{if_x} \langle n^{(0)}|m^{(0)}, iA\rangle + e^{-if_x} \langle n^{(0)}|m^{(0)}, -iA\rangle\right) \langle m^{(0)}|\, V_+ \,|0^{(0)}\rangle \\
&= -\sum_{m=1}^{\infty} \frac{4e^{-A^2}A^n}{\hbar\omega_c m\sqrt{n!}} \cos\left((n-m)\frac{\pi}{2} + f_x\right) \cos\left(\frac{m\pi}{2} + f_x\right) \mathcal{L}_m^{n-m}(A^2). \qquad (2.56)
\end{aligned}$$

The evaluation of the other terms is relatively easy. We apply the property of the displacement operator in equation 2.45 and the result of the first order correction. The second order correction to the ground state is,

$$\begin{aligned}
|0^{(2)}\rangle = \frac{2g(\gamma_-)^2 e^{-A^2}}{\omega_c^2} \Bigg\{ &\sum_{n=1}^{\infty} \left(\frac{2A^n}{n^2\sqrt{n!}}\right) \times \\
&\left(\sum_{m=1}^{\infty} \frac{n}{m} \cos\left((n-m)\frac{\pi}{2} + f_x\right) \cos\left(\frac{m\pi}{2} + f_x\right) \mathcal{L}_m^{n-m}(A^2) \right. \\
&\left. + \cos\left(\frac{n\pi}{2} + f_x\right) \cos f_x \right) |n^{(0)}\rangle - \sum_{m=1}^{\infty} \frac{A^{2m}}{m^2 m!} \cos^2\left(\frac{m\pi}{2} + f_x\right) |0\rangle^{(0)} \Bigg\}. \qquad (2.57)
\end{aligned}$$

Finally, the third order energy correction can be calculated as,

$$\begin{aligned}
E_0^{(3)} &= \langle 0^{(0)}|\, V_+ \,|0^{(2)}\rangle - E_0^{(1)} \langle 0^{(0)}|0^{(2)}\rangle - E_0^{(2)} \langle 0^{(0)}|0^{(1)}\rangle \\
&= -\sum_{n=0}^{\infty} 2g(\gamma_-) \cos\left(\frac{n\pi}{2} + f_x\right) \frac{e^{-\frac{A^2}{2}} A^n}{\sqrt{n!}} \langle n^{(0)}|0^{(2)}\rangle\,. \qquad (2.58)
\end{aligned}$$

We make a few remarks. First, the $i^{\text{th}}$ order energy correction is $\mathcal{O}(g(\gamma)^i)$, therefore $\mathcal{O}(\cos(\gamma_-)^i)$, which means these energy corrections are closely related to the Fourier coefficient of the potential energy surface. Second, the first order energy correction is suppressed by $\exp(-\frac{A^2}{2})$, while the second order energy correction is not. More generally, the corrections in odd orders are suppressed, while the even orders are not. Hence, the potential energy surface is basically $\pi$-periodic with a small $2\pi$-periodic correction. We exclusively study the properties of this type of potential in the next section.

At the end of this section, for a complete understanding to the system, we solve the perturbation problem from another perspective. We choose the coherent states basis $\{|n(iA)\rangle\}$, where $n$ is an integer and $i$ is the imaginary unit, and we neglect the overlaps between the states, which is in order of $\mathcal{O}(\exp(-A^2/2))$. This method misses some subtle structure because it approximate an overcomplete basis as a complete basis. However, it provides an intuitive picture to the problem. In the coherent state basis, we rewrite the Hamiltonian in equation 2.44,

$$H_{+,\mathrm{co}} = \sum_{n=-\infty}^{\infty} \left\{ n^2 \hbar\omega_c A^2 \left|n(iA)\right\rangle \left\langle n(iA)\right| \right. \\ \left. -E_J \cos\gamma_- \left( \left|n(iA)\right\rangle \left\langle (n-1)iA\right| e^{if_x} + \left|n(iA)\right\rangle \left\langle (n+1)iA\right| e^{-if_x} \right) \right\}. \quad (2.59)$$

The Hamiltonian is identical to the Hamiltonian of a Josephson junction, where the coherent state $|n(iA)\rangle$ corresponds to the Cooper pair number state $|n\rangle$. The Hamiltonian is similar to the Hamiltonian of a Josephson junction, where the capacitance energy is $2A^2\hbar\omega_c$ and the Josephson energy is $E_J \cos\gamma_-$. Because $2\hbar\omega_c A^2 = E_{C_J}/2 \gg E_J$, the spectrum of the system is the typical spectrum of a Cooper pair box qubit. The ground state energy of the Cooper pair box is given by the eigenvalue of Mathieu function [45]. The first eigenvalue can be expanded in terms of $E_J/(\hbar\omega_c A^2)$ as

$$E_{0,\mathrm{co}} = \hbar\omega_c A^2 \left( 2 \left( \frac{E_J \cos\gamma_-}{\hbar\omega_c A^2} \right)^2 + \frac{7}{2} \left( \frac{E_J \cos\gamma_-}{\hbar\omega_c A^2} \right)^4 + \mathcal{O}\left( \left( \frac{E_J \cos\gamma_-}{\hbar\omega_c A^2} \right)^6 \right) \right). \quad (2.60)$$

If we only take the lowest nonzero order, the energy reduces the result in equation 2.53. Note that the expansion of the energies does not contain the odd orders, because those terms correspond to the overlaps of the coherent states. The odd orders of the energy expansion are small compared to nearby even order expansion coefficients, but they play a very important role in the spectrum of the zero-pi qubit, which we will discuss in the next section. The disappearance of the odd orders makes this method unsuitable for further analysis.

In conclusion, we applied the BO approximation and used perturbation theory to calculate the energy surface. We reduced the system to a one-dimensional problem specified by

$$H_- = \frac{1}{4} E_{C_-} (n_- - n_{g_-})^2 + V_-(\gamma_-), \quad (2.61)$$

where $V_-(\gamma_-) = \sum_{n=0}^{\infty} E_0^{(n)}$. The energy coefficient $E_0^{(n)}$ is the $n^{\mathrm{th}}$ order correction to the energy derived from perturbation theory.

## 2.4 Tight-Binding model

In the previous section we used the BO approximation to effectively reduce the system to a one-dimensional problem, described by equation 2.61. In this section, we study the properties of this one-dimensional problem and find the spectrum structure of the zero-pi qubit.

The potential of the one-dimensional system consists of a sum of energy corrections. The sequence has two important properties. Firstly, the $i^{\text{th}}$ order correction is associated with $(\cos\gamma_-)^i$. Secondly, the coefficients of odd orders are much smaller than coefficients of even orders. To capture the major character of the potential while not making the calculation too complicated, we keep the potential up to the second order. This is equivalent to keeping the lowest two nonzero Fourier components of the potential. We refer to the approximate Hamiltonian as a truncated Hamiltonian,

$$H_{-,\text{truncated}} = \frac{1}{4}E_{C_-}(n_- - n_{g_-})^2 + V_{-,1}\cos\gamma_- + V_{-,2}\cos(2\gamma_-), \tag{2.62}$$

where $V_{-,1} = E_0^{(1)}/\cos\gamma_-$, $V_{-,2} = E_0^{(2)}/(2\cos^2\gamma_-)$, and we have neglected the constant term generated in the transformation $2\cos^2(\gamma_-) = \cos(2\gamma_-)+1$. Because we have $|V_{-,1}| \ll |V_{-,2}|$, the potential is mostly $\pi$-periodic and is modified by a $2\pi$-periodic correction. Thus we solve the problem starting with the $\pi$-periodic component of the potential, followed by considering the $2\pi$-periodic part. The solution is obtained using the tight-binding model.

The tight-binding approximation is widely used in condensed matter physics for solving for Bloch wavefunction in the periodic potential of crystal. The approximation exploits the property of small tunneling between wells, and assumes the Bloch wave is simply the superposition of localized states of each well. More information of the tight-binding model can be found in [46].

### 2.4.1 Pi periodic potential and WKB approximation

In this subsection we solve a simplified version of the problem where we set $V_{-,1} = 0$ in equation 2.62. The Hamiltonian of this problem is given by

$$H_{-,\text{simplified}} = \frac{1}{4}E_{C_-}(n_- - n_{g_-})^2 + V_{-,2}\cos(2\gamma_-). \tag{2.63}$$

The potential is in the form of simple sinusoidal function, as shown in figure 2.4. We expect Bloch wave solutions form a band structure. The periodicity of the potential is $\pi$. Based on the properties of Bloch functions [47], the edges of the first Brillouin zone are $\pm 1$.

The circuit elements satisfy the relation $4E_J^2/E_{C_J} \gg \frac{1}{2}E_{C_0}$, which means the barrier between wells in significantly larger than the kinetic energy of lowest states. The wavefunctions for the lowest states are localized within the wells and it is suitable to apply the tight-binding approximation. The band structure is then derived from taking the overlap of neighboring wavefunctions as a perturbation.

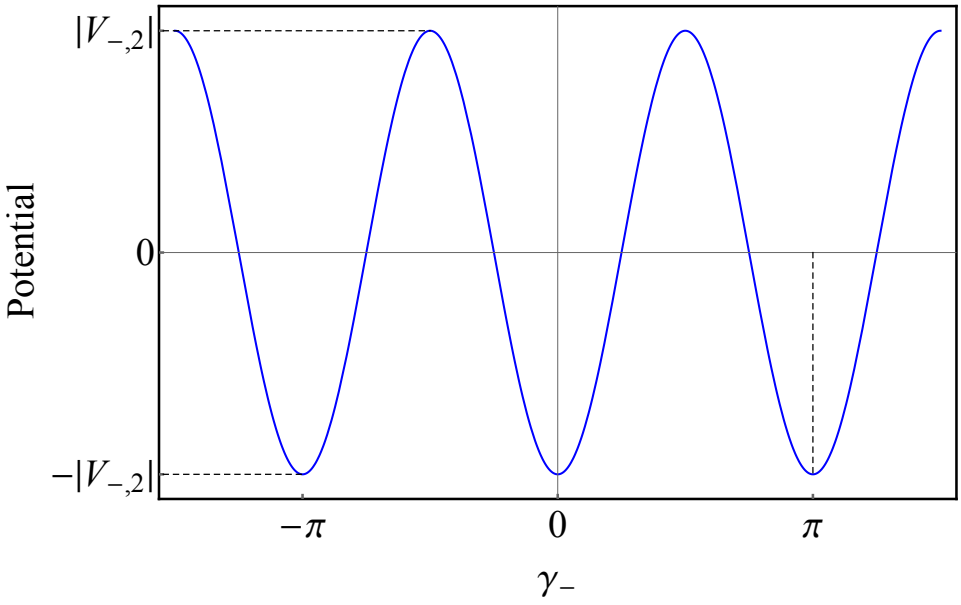


Figure 2.4: The figure depicts the potential in the equation 2.63. The potential is $\pi$-periodic.

Firstly we solve the single well problem to obtain the wavefunction. We select the single well as shown in the figure 2.5, which is described by the potential function,

$$V^R_{-,\text{single}}(\gamma_-) = \begin{cases} V_{-,2}\cos(2\gamma_-), & |\gamma_- - R| \leq \pi/2, \\ -V_{-,2}, & \text{elsewhere}, \end{cases} \tag{2.64}$$

with $R = n\pi$ and $n$ an integer. Note that $V_{-,2} < 0$. To find the wavefunction in this well, we take the WKB semi-classical approximation [48]. We divide the potential into five parts, as shown 2.5. In the center part (III), the potential is close to a quadratic function, and thus the wavefunction is close to the solution to a harmonic oscillator, which we use as a starting point of the perturbation approximation. In the region II and IV, where we refer as shoulders, the potential is significantly deviate from quadratic and the

wavefunction deviates from the harmonic oscillator solution. The connecting points of the center and the shoulders are referred as $\pm\gamma_{\text{connect}}$. We use the WKB approximated solution in shoulder regions and connect them to the solution in the center to fulfill the continuity. Outside the well, where $|\gamma_- - R| > \pi$, the potential is flat and the wavefunction becomes a simple exponential decay function.

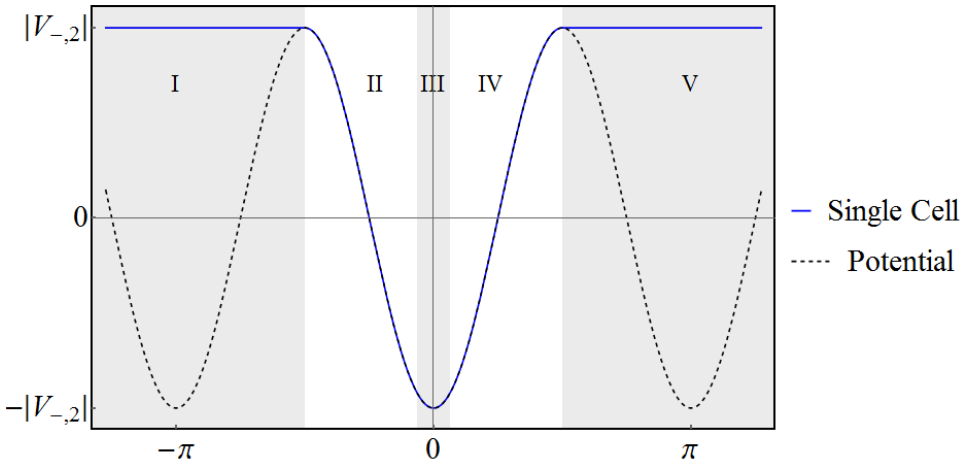


Figure 2.5: A single cell centered at $\gamma_- = 0$. The blue solid line is the single cell potential, while the potential is plotted in the dashed line. A cell is divided into five parts: two outside parts, two shoulder regions and one center part.

In the vicinity of $\gamma_- = 0$, we expand the potential in orders of $\gamma_-$, and keep up to the second order as $V_{-,2}(1 - 2\gamma_-^2)$. The quadratic term of the potential, with the kinetic term $\frac{1}{4}E_{C_-}(n_- - n_g)^2$, forms a Hamiltonian of a harmonic oscillator. For convenience we define the energy ratio,

$$\eta = \frac{|4V_{-,2}|}{|E_{C_-}/2|} = \frac{-8V_{-,2}}{E_{C_-}}. \tag{2.65}$$

We note that $\eta \gg 1$. The ground state wavefunction is easily obtained as,

$$\psi_{\text{WKB, center}} = \left(\frac{\eta}{\pi^2}\right)^{\frac{1}{8}} \exp\left(\frac{-\sqrt{\eta}}{2}\gamma_-^2\right), \tag{2.66}$$

with energy $E_{\text{WKB}} = V_{-,2}(1 - 2/\sqrt{\eta})$. Then we need to determine the connecting point $\gamma_{\text{connect}}$. The connection point should fulfill two requirements. First, it should be sufficiently small such that the harmonic oscillator ground state approximates the wavefunction in the center part. Second, it should be larger than the "turning point", where the potential

energy approaches the state energy and the WKB approximation fails. The turning point is determined by solving the equation,

$$V_{-,2}\cos(2\gamma_{\text{turn}}) = E_{\text{WKB}} = V_{-,2}\left(1 - \frac{2}{\sqrt{\eta}}\right). \tag{2.67}$$

Because $\eta$ is very large, the solution to the above equation satisfies $\gamma_{\text{turn}} \approx 1/\eta^{1/4}$, which is a small quantity. We can therefore select the connecting point $\gamma_{\text{connect}}$ in the range $(\gamma_{\text{turn}}, 1)$ such it satisfies the above requirements. However, as we will see in the following, we do not need to specify $\gamma_{\text{connect}}$ because the results do not explicitly depend on $\gamma_{\text{connect}}$. Before we present the details of the derivation, we review the two requirements of $\gamma_{\text{connect}}$. The first requirement guarantees the validity of approximating the wavefunction by ground state of harmonic oscillator. Moreover, it allows us to (approximately) equal $1 - 2\gamma_{\text{connect}}^2$ and $\cos(2\gamma_{\text{connect}})$. The second requirement brings us the relation $V^R_{-,\text{single}}(\gamma_-) - V_{-,2} \gg E_{\text{WKB}} - V_{-,2}$.

The WKB approximation is elaborated in many text books. We follow the steps in [48]. We firstly define

$$k(\gamma_-) = \left(\frac{4}{E_{C_-}}\left(E_{\text{WKB}} - V_{-,2}\cos(2\gamma_-)\right)\right)^{\frac{1}{2}}. \tag{2.68}$$

The wavefunction in the WKB approximation in the shoulder area $\gamma_{\text{connect}} < \gamma_- < \pi/2$ is given by

$$\psi_{\text{WKB,shoulder}} = \frac{\mathcal{A}}{\sqrt{k(\gamma_-)}}\exp\left(i\int_{\gamma_{\text{connect}}}^{\gamma_-} dr k(r)\right), \tag{2.69}$$

where $\mathcal{A}$ is a constant determined by the continuity of the wavefunctions at the connecting point. On one side of the connection point, the solution is the ground state of harmonic oscillator. The wavefunction at the connecting point is,

$$\psi_{\text{WKB,center}}(\gamma_{\text{connect}}) = \left(\frac{\eta}{\pi^2}\right)^{\frac{1}{8}}\exp\left(\frac{-\sqrt{\eta}}{2}\gamma^2_{\text{connect}}\right). \tag{2.70}$$

On the other side, the wavefunction from the WKB approximation at the connecting point is,

$$\psi_{\text{WKB,shoulder}}(\gamma_{\text{connect}}) = \frac{A}{k(\gamma_{\text{connect}})^{\frac{1}{2}}}. \tag{2.71}$$

Therefore, we can determine the value of $\mathcal{A}$,

$$\mathcal{A} = \left(\frac{\eta}{\pi^2}\right)^{\frac{1}{8}}\exp\left(-\frac{\sqrt{\eta}}{2}\gamma^2_{\text{connect}}\right)k(\gamma_{\text{connect}})^{\frac{1}{2}}. \tag{2.72}$$

After substituting $\mathcal{A}$ into equation 2.69 we obtain the expression of the wavefunction

$$\psi_{\text{WKB,shoulder}}(\gamma_-) = \left(\frac{\eta}{\pi^2}\right)^{\frac{1}{8}} \frac{k(\gamma_{\text{connect}})^{\frac{1}{2}}}{k(\gamma_-)^{\frac{1}{2}}} \exp\left(i\int_{\gamma_{\text{connect}}}^{\gamma_-} dr k(r) - \frac{\sqrt{\eta}}{2}\gamma_{\text{connect}}^2\right). \tag{2.73}$$

We first calculate the exponential term. The factor on the exponential can be significantly simplified based on the two requirements of $\gamma_{\text{connect}}$. Firstly, $\gamma_{\text{connect}}$ fulfills the relation $V^R_{-,\text{single}}(\gamma_-) - V_{-,2} \gg E_{\text{WKB}} - V_{-,2}$, therefore we can expand the integration term on the exponential,

$$i\sqrt{\frac{4}{E_{C_-}}(E_{\text{WKB}} - V_{-,2}\cos(2r))} \approx -\sqrt{\eta}\left(\sin r - \frac{1 - E_{\text{WKB}}/V_{-,2}}{4\sin r}\right). \tag{2.74}$$

We then substitute $E_{\text{WKB}} = V_{-,2}(1 - 2/\sqrt{\eta})$ into the equation and calculate the integral in the exponential in equation 2.73. The factor in the exponential becomes

$$\sqrt{\eta}(\cos(\gamma_-) - \cos(\gamma_{\text{connect}})) + \frac{1}{2}\log\left(\frac{\tan(\gamma_-/2)}{\tan(\gamma_{\text{connect}}/2)}\right) - \frac{\sqrt{\eta}}{2}\gamma_{\text{connect}}^2. \tag{2.75}$$

We expand $\cos(\gamma_{\text{connect}})$ to the second order and arrive at the simplified form of the exponential term, given by

$$\left(\frac{\tan(\gamma_-/2)}{\tan(\gamma_{\text{connect}}/2)}\right)^{\frac{1}{2}} \exp\left(\sqrt{\eta}(\cos(\gamma_-) - 1)\right). \tag{2.76}$$

Now we turn to the pre-factor in equation 2.73. We simplify it by the relation

$$\frac{k(\gamma_{\text{connect}})}{k(\gamma_-)} = \left(\frac{E_{\text{WKB}} - V_{-,2}\cos(2\gamma_{\text{connect}})}{E_{\text{WKB}} - V_{-,2}\cos(2\gamma_-)}\right)^{\frac{1}{2}} \approx \left(\frac{1 - \cos(2\gamma_{\text{connect}})}{1 - \cos(2\gamma_-)}\right)^{\frac{1}{2}}. \tag{2.77}$$

Here, the approximation is valid based on the relation $V^R_{-,\text{single}}(\gamma_-) - V_{-,2} \gg E_{\text{WKB}} - V_{-,2}$. To further simplify the expression, we apply the equation $1 - \cos(2x) = 2\sin^2(x) = 8\sin^2(x/2)\cos^2(x/2)$, and approximate $\cos(x) \approx 1$ when $x = \gamma_{\text{connect}}$. We can write the final form of the WKB approximation as

$$\psi_{\text{WKB,shoulder}}(\gamma_-) = \left(\frac{\eta}{\pi^2}\right)^{\frac{1}{8}} \frac{\exp(\sqrt{\eta}(\cos(\gamma_-) - 1))}{\cos(\gamma_-/2)}. \tag{2.78}$$

When $|\gamma_-| > \pi/2$, the potential is a constant and the wavefunction decays exponentially. The decay rate is determined by $\sqrt{(-V_{-,2} - E_{\text{WKB}})/(E_{C_-}/4)} = \sqrt{\eta - \sqrt{\eta}}$. We once again

use the continuity of the wavefunction to determine the amplitude. At the point $\gamma_- = (\pi/2)^-$, the amplitude is,

$$\psi_{\text{WKB,shoulder}}(\pi/2) = \left(\frac{16\eta}{\pi^2}\right)^{\frac{1}{8}} \exp(-\sqrt{\eta}). \tag{2.79}$$

Therefore, the wavefunction outside the well is described by,

$$\psi_{\text{WKB,outside}}(\gamma_-) = \left(\frac{16\eta}{\pi^2}\right)^{\frac{1}{8}} \exp\left(-\sqrt{\eta} - \sqrt{\eta - \sqrt{\eta}}(\gamma_- - \pi/2)\right). \tag{2.80}$$

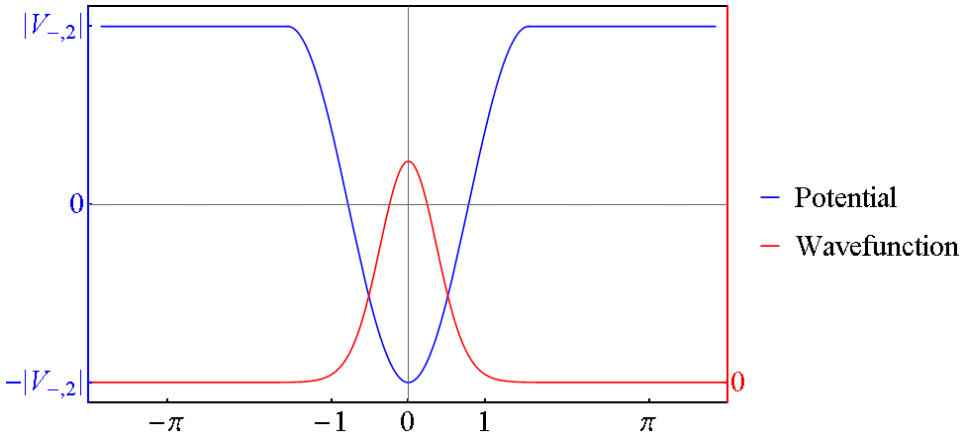


Figure 2.6: The potential and its solution based on WKB approximation in one cell. The blue line is the potential. The red line is the wavefunction.

In this subsection we have derived the WKB approximation of the wavefunction in a single well. The wavefunction is a piecewise function defined as

$$\psi_{\text{WKB}}(\gamma_-) = \left(\frac{\eta}{\pi^2}\right)^{\frac{1}{8}} \times \begin{cases} \exp\left(\frac{-\sqrt{\eta}}{2}\gamma_-^2\right) & |\gamma_-| \leq \gamma_{\text{connect}} \\ \exp(\sqrt{\eta}(\cos(\gamma_-) - 1))/\cos(\gamma_-/2) & \gamma_{\text{connect}} < |\gamma_-| \leq \pi/2 \\ \sqrt{2}\exp\left(-\sqrt{\eta} - \sqrt{\eta - \sqrt{\eta}}(|\gamma_-| - \pi/2)\right) & \pi/2 < |\gamma_-|. \end{cases} \tag{2.81}$$

The wavefunction is plotted in figure 2.6.

We next make a few remarks on this result. Firstly, it is important to mention that the functions in each interval are independent on the connecting point $\gamma_{\text{connect}}$. We achieve this

result by requiring $\gamma_{\text{connect}}$ to be small enough such that we are content to keep the lowest orders of Taylor expansion of $\cos(\gamma_{\text{connect}})$, and sufficiently large when compared with the turning point $\gamma_{\text{turn}}$. Secondly, one may consider the straightforward perturbation method of $\cos(2\gamma_-)$ potential instead of the WKB approximation. However, we emphasize the importance of the accuracy of the tail part of the wavefunction. The band structure is sensitive to the overlap of the neighboring wavefunctions, where the tail part is important. Perturbation theory results in a finite superposition of Fock states, which have $\exp(-Rx^2)$ decay and significantly deviate from the exponential decay. Therefore the WKB approximation is better than the direct perturbation approximation. The third remark is concerned with the energy approximation. Because the exponential decay rate is associated with the energy of the state, a small modification can lead to a large error. To estimate the error, we consider the upper bound and lower bound on the energy. The upper bond is exactly the energy $E_{\text{ub}} = E_{\text{WKB}}$, because the parabolic potential we used is no lower everywhere than the single well. Thus the energy of exact solution is less than $E_{\text{WKB}}$. The lower bond can be given by the Mathieu function solving equation 2.63. Similarly, because the periodic potential is no larger everywhere than the single well, the energy obtained from periodic potential must be smaller than or equal to the energy of ground state of a single well. The lower bound, which is given by the Mattieu function [45] in a periodic potential, is

$$E_{\text{lb}} = V_{-,2}\left(1 - \frac{2}{\sqrt{\eta}} + \frac{1}{4\eta} + \mathcal{O}\left(\frac{1}{\eta^{3/2}}\right)\right). \tag{2.82}$$

Therefore the error made in estimating the energy is less than $V_{-,2}/4\eta$. The maximum $|\gamma_-|$ we are interested is $3\pi/2$, when we consider the nearest neighbor effect. At this value, the upper bound of the error on the ratio of the amplitudes is given by

$$r = \frac{\exp\left(-\frac{3\pi}{2}\sqrt{\frac{-V_{-,2}-E_{\text{ub}}}{E_{C_-}/4}}\right)}{\exp\left(-\frac{3\pi}{2}\sqrt{\frac{-V_{-,2}-E_{\text{lb}}}{E_{C_-}/4}}\right)} \approx \exp\left(\frac{3\pi}{32}\frac{1}{\sqrt{\eta-\sqrt{\eta}}}\right). \tag{2.83}$$

Because the circuit has the relation $2|V_{-,2}| \gg E_{C_-}$, we have $\eta > 4$, and consequently $r < 1.23$. This ratio is in the worst-case scenario. In fact, $\eta$ can easily achieve 50 and limit the erroneous ratio within 1.05, which is acceptable.

### 2.4.2 Pi periodic potential and tight-binding approximation

In this subsection we establish the tight-binding model based on the wavefunction we obtained previously. Recall the equation 2.63, which defines the problem,

$$H_{-,\text{simplified}} = \frac{1}{4}E_{C_-}(n_- - n_{g_-})^2 + V_{-,2}\cos(2\gamma_-). \tag{2.63 revisited}$$

We assume that the superposition of the local ground states

$$\psi_k = \sum_R e^{ikR} \psi_{\mathrm{WKB}}(\gamma_- - R), \tag{2.84}$$

where $R = n\pi$ with integer $n$, satisfies the Schördinger equation

$$H_{-,\mathrm{simplified}} \left|\psi_k\right\rangle = E_k \left|\psi_k\right\rangle . \tag{2.85}$$

Here, the quasi-momentum $k$ is confined to the first Brillouin zone, $-1 < k < 1$. Associated with $k$, $E_k$ and $\psi_k$ are the eigenenergy and the wavefunction respectively. We rewrite the Hamiltonian, emphasizing the single well potential in equation 2.64, as

$$H_{-,\mathrm{simplified}} = \frac{1}{4} E_{C-} (n_- - n_{g-})^2 + V^{R=0}_{-,\mathrm{single}}(\gamma_-) + U^{R=0}, \tag{2.86}$$

where the single where potential describes the well located between $-\pi/2$ to $\pi/2$ while elsewhere is constant. The complementary potential $U$ is obtained as the total potential without that of a single well:

$$U^{R=0} = V_{-,2} \cos 2\gamma_- - V^{R=0}_{-,\mathrm{single}}(\gamma_-). \tag{2.87}$$

We take the scalar product of equation 2.85 with $|\psi_{\mathrm{WKB}}(\gamma_-)\rangle$. We obtain

$$E_{\mathrm{WKB}}(1+\gamma) + \alpha + \beta = E_k(1+\gamma). \tag{2.88}$$

Here we use the quantities $\alpha$, $\beta$ and $\gamma$ which are defined as

$$\alpha = \langle\psi_{\mathrm{WKB}}(\gamma_-)| \, U \left|\psi_{\mathrm{WKB}}(\gamma_-)\right\rangle , \tag{2.89}$$

$$\beta = \langle\psi_{\mathrm{WKB}}(\gamma_-)| \, U \overline{|\psi_{\mathrm{WKB}}(\gamma_-)\rangle}, \tag{2.90}$$

and

$$\gamma = \langle\psi_{\mathrm{WKB}}(\gamma_-) \overline{|\psi_{\mathrm{WKB}}(\gamma_-)\rangle} , \tag{2.91}$$

with $\overline{|\psi_{\mathrm{WKB}}(\gamma_-)\rangle} = |\psi_k\rangle - |\psi_{\mathrm{WKB}}(\gamma_-)\rangle$. We have assumed that the wavefunction at each well is localized, therefore we neglect the parameter $\gamma$. In addition, we only consider the nearest neighbor effect in $\beta$. Also note the compensating potential $U$ is zero when $|\gamma_-| < \pi/2$. Thus the quantity $\alpha$ can be neglected. We then obtain the expression of $E_k$ as,

$$E_k = E_{\mathrm{WKB}} + \beta. \tag{2.92}$$

We are content to keep the nearest neighbor effect and drop other terms, in which case $\beta$ can be simplified to

$$\beta = 2V_{-,2}\cos(k\pi)\int_{\pi/2}^{3\pi/2}\psi^*_{\mathrm{WKB}}(\gamma_-)(\cos(2\gamma_-)+1)\psi_{\mathrm{WKB}}(\gamma_- - \pi)d\gamma_-. \tag{2.93}$$

The integral is easy to calculate based on the result of WKB approximation. We have

$$\beta \approx -\cos(k\pi)\frac{16}{\sqrt{\pi}}\frac{V_{-,2}}{\eta^{\frac{1}{4}}}\exp(-2\sqrt{\eta}), \tag{2.94}$$

where we approximated $E_{\mathrm{WKB}} \approx -V_{-,2}$. Therefore we obtain the bandwidth of the first band, given by

$$w = -\frac{32}{\sqrt{\pi}}\frac{V_{-,2}}{\eta^{\frac{1}{4}}}\exp(-2\sqrt{\eta}). \tag{2.95}$$

We see that with the absence of the $2\pi$-periodic potential term $V_{-,1}\cos(\gamma_-)$, the bandwidth is exponentially suppressed by $\exp(-2\sqrt{\eta})$. In figure 2.7 we plot the energy in the first Brillouin zone.

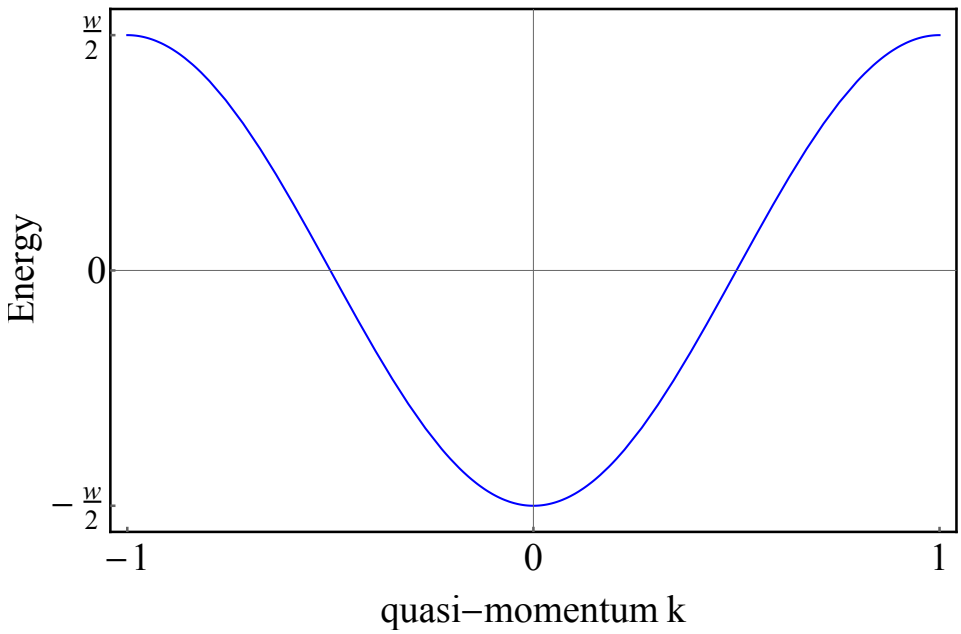


Figure 2.7: The first band of the $\pi$-periodic potential. The energy is scaled with $w$, which is defined in equation 2.95.

In superconducting materials, the wavefunction has to be periodic with period $2\pi$. In the frame of Bloch solution and in the absence of the offset charge this constrains the quasi-momentum to be an integer. Because the first Brillouin zone extends from $-1$ to 1, there can be two states in the first band. If the offset charge $n_{g_-} = 0$, the two states will be $k = 0$ and $k = \pm 1$. In the case where $n_{g_-} \neq 0$, the solution to the Schödinger equation can be obtained by apply the gauge transformation $\tilde{\psi} = e^{in_{g_-}\gamma_-}\psi$ and $\tilde{\psi}$ is $2\pi$-periodic. The relative quasi-momentum of Bloch wave is $-n_{g_-}$ and $-n_{g_-} \pm 1$. In either case where the offset charge $n_{g_-}$ is zero or not, the first band contains and only contains two solutions. The second band is near the first excited state energy of a single well and stays very far from the first band. Because the lowest two states are well-separated from other states, and the energy gap of two states is very small compared to any other energy scales in the system, we conclude that the system has a nearly-degenerate ground state.

The key to forming the nearly-degenerated states structure is to have the $\pi$-periodic potential. In the classical superconduction qubits, such as the transmon qubit and the flux qubit, the potential is $2\pi$-periodic, which is consistent with the wavefunction periodicity. Each band contains one state, and the qubit levels rely on the different levels of bands. However, in the zero-pi qubit, the symmetry of the circuit leads to a translation symmetry of $\pi$ rather than $2\pi$. As a result, the periodicity of the potential is reduced to $\pi$ and each band contains two states.

Until now, we only considered the $\pi$-periodic part and omitted the $2\pi$-periodic part of the potential. As discussed above, the $2\pi$-periodic part breaks the nearly-degenerate subspace and shifts the energy gap. Fortunately, the $2\pi$-periodic component is much smaller than the $\pi$-periodic component and can be treated by perturbation theory. The Hamiltonian containing the $\pi$-periodic part will be studied in the next subsection.

In the last part of this subsection, we check the validation of the WKB and tight-binding approximation. The solution to the problem defined by the Hamiltonian 2.63 can be expressed in terms of Mathieu function theory. The width of the first band can be found in the table [45]. The width expansion in orders of $1/\sqrt{\eta}$ is

$$w_{\text{Mathieu}} = -\frac{8}{\sqrt{\pi}} \frac{V_{-,2}}{\eta^{\frac{1}{4}}} \exp(-2\sqrt{\eta})(1 + \mathcal{O}(1/\sqrt{\eta})). \tag{2.96}$$

Compared with the result we obtained before, the approximation result perfectly matches the analytical result to the first order, as expected.

### 2.4.3 2Pi periodic potential and tight-binding approximation

After analyzing the Hamiltonian with merely the $\pi$-periodic component in the previous subsection, we include now the $2\pi$-periodic component. Recall the Hamiltonian in equation 2.62,

$$H_{-,\text{truncated}} = \frac{1}{4}E_{C-}(n_- - n_{g-})^2 + V_{-,1}\cos\gamma_- + V_{-,2}\cos(2\gamma_-), \qquad \text{(2.62 revisited)}$$

where the energy scales satisfy the relation $|V_{-,2}| \gg E_{C-} \gg |V_{-,1}|$. Because $|V_{-,1}|$ is very small compared to $|V_{-,2}|$, we simply keep using the wavefunction derived in WKB approximation result with $V_{-,1} = 0$, and apply the perturbation theory on the tight-binding model.

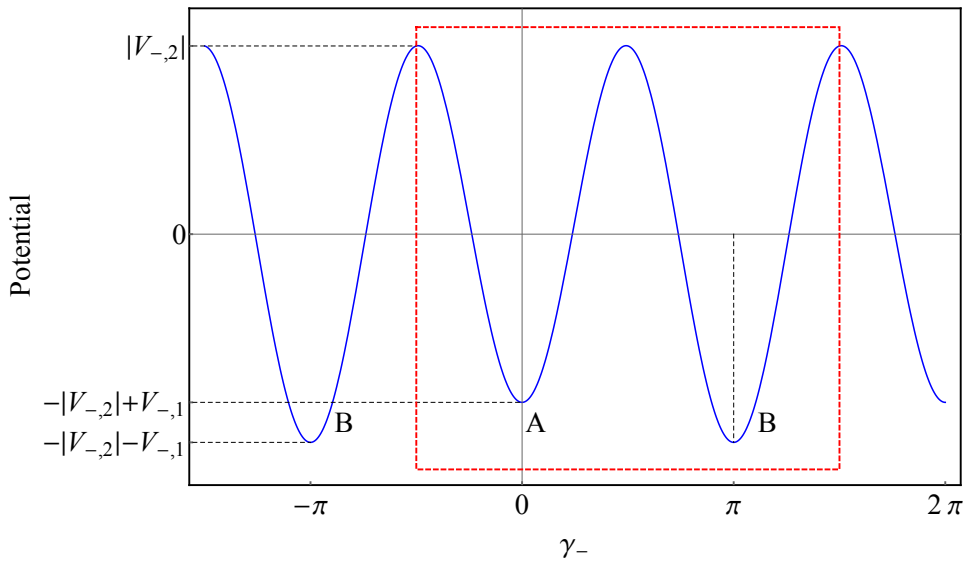


Figure 2.8: The potential in equation 2.62. The value of $|V_{-,1}|$ has been exaggerated compared to typical values for realistic parameters. The external flux is set to be 0. The presence of $V_{-,1}$ changes the energy of lowest point of each well, while the peak energy of the barrier does not change. We label the wells located at $2n\pi$ with "A", and $(2n+1)\pi$ with "B", where $n$ is an integer. The red box indicates a single cell of this $2\pi$-periodic potential.

As shown in the figure 2.8, the basic cell has the width of $2\pi$ and contains two different wells. We therefore apply the tight-binding approximation for a two-atom basis. We divide

the wells into two groups. One group, which we label by "A", are wells located at $2n\pi$, with $n$ an integer. In the group A, the ground state energy is

$$E_A = E_{\text{WKB}} + V_{-,1}. \tag{2.97}$$

We label the other group "B", with ground state energy

$$E_B = E_{\text{WKB}} - V_{-,1}. \tag{2.98}$$

According to the tight-binding approximation, we assume the solution to the equation 2.62 is

$$\psi_k = \sum_R e^{ikR} \left( A_k \psi_{\text{WKB}}(\gamma_- - R) + e^{ik\pi} B_k \psi_{\text{WKB}}(\gamma_- - R - \pi) \right), \tag{2.99}$$

where $k$ is the quasi-momentum, $R = 2n\pi$ with integer $n$ is the position of the cell, and $A_k$, $B_k$ are the coefficients of related wavefunctions in different groups. Note that the quasi-momentum $k$ has a range of $[-1/2, 1/2]$. Also, we denote the energy as $E_k$.

In order to obtain the band information, we apply $\langle \psi_{\text{WKB}}(\gamma_-)|$ and $\langle \psi_{\text{WKB}}(\gamma_- - \pi)|$ to the left of the equation $H_{-,\text{truncated}} |\psi_k\rangle = E_k \psi_k$, and keep the effect of nearest neighbor wells. We obtain two equations:

$$(E_{\text{WKB}} + V_{-,1})(A_k + B_k\gamma) + A_k\alpha + B_k\beta = E_k(A_k + B_k\gamma), \tag{2.100}$$

and

$$(E_{\text{WKB}} - V_{-,1})(B_k + A_k\gamma) + B_k\alpha + A_k\beta = E_k(B_k + A_k\gamma). \tag{2.101}$$

Here we use $\alpha$, $\beta$ and $\gamma$ to write the equations in compact form. They are defined slightly differently from the quantities defined in the previous subsection:

$$\alpha = \langle \psi_{\text{WKB}}(\gamma_-)| \, U \, |\psi_{\text{WKB}}(\gamma_-)\rangle \,, \tag{2.102}$$

$$\beta = 2\cos(k\pi) \, \langle \psi_{\text{WKB}}(\gamma_-)| \, U \, |\psi_{\text{WKB}}(\gamma_- - \pi)\rangle \,, \tag{2.103}$$

$$\gamma = 2\cos(k\pi) \, \langle \psi_{\text{WKB}}(\gamma_-)|\psi_{\text{WKB}}(\gamma_- - \pi)\rangle \,. \tag{2.104}$$

Here, we denote the compensating potential as $U = V_{-,2}\cos 2\gamma_- - V^{R=0}_{-,\text{single}}(\gamma_-)$, where the small component $V_{-,1}$ has been neglected. Again, because the wavefunctions are localized in the wells, we can safely drop out terms with $\gamma$. Moreover, we can neglect $\alpha$ because the wavefunction $\psi_{\text{WKB}}(\gamma_-)$ is localized in the cell, where the compensating potential $U = 0$.

$$\begin{pmatrix} E_{\text{WKB}} + V_{-,1} & \beta \\ \beta & E_{\text{WKB}} - V_{-,1} \end{pmatrix} \begin{pmatrix} A_k \\ B_k \end{pmatrix} = E_k \begin{pmatrix} A_k \\ B_k \end{pmatrix}. \tag{2.105}$$

The solution to this equation defines a two-level system, which encodes a qubit. Because $E_{\mathrm{WKB}}$ behaves as the zero-point energy, we can disregard it. We denote the two eigenvalues as $E_0$ and $E_1$. They are given by:

$$E_0 = -\sqrt{V_{-,1}^2 + \beta^2} \tag{2.106}$$

and

$$E_1 = +\sqrt{V_{-,1}^2 + \beta^2}. \tag{2.107}$$

Since the wavefunction in the superconducting circuit has to have a periodicity of $2\pi$, the quasi-momentum $k$ is determined by the offset charge $n_{g,-}$. We discuss this result in two cases. In the first case we set the bias flux bias such that $\cos f_x = 0$, thus $V_{-,1} = 0$. The potential is $\pi$-periodic, which we have discussed in the previous subsection. For completeness we restate the conclusion here: when $V_{-,1}$ vanishes, the system takes two states in its lowest band. The third state is far away from the two-level system, which leads to a nearly degenerate subspace. The eigenfunctions consist of localized ground states of each well. The band is shown in figure 2.9.

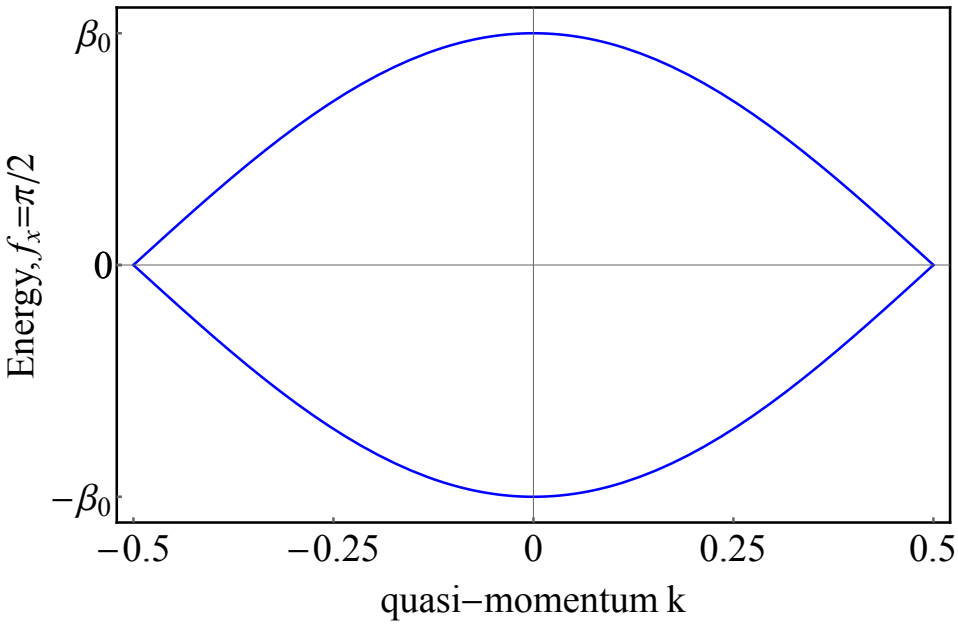


Figure 2.9: The band structure when the external flux $f_x = \pi/2$. We define $\beta_0 = |\beta/\cos(k\pi)|$ for simplicity. The dimensionless circuit parameters are $E_J = 1$, $E_{C_J} = 20$, $E_L = 1/150$ and $E_C = 1/35$. This band is identical to the band shown in the figure 2.7.

The second case we are interested in is $|V_{-,1}| \gg |\beta|$. This relation can be equivalently expressed by

$$2E_J|\cos f_x| \exp\left(-\frac{1}{8}\sqrt{\frac{E_{C_J}}{E_L}}\right) \gg |\cos(k\pi)|\frac{4}{\sqrt{\pi}}\frac{|V_{-,2}|}{\eta^{\frac{1}{4}}}\exp(-2\sqrt{\eta}), \tag{2.108}$$

where $\eta \approx 128E_J^2/(E_{C_J}E_C)$ and $V_{-,2} \approx 4E_J^2/E_{C_J}$. The relation is automatically fulfilled when $\cos f_x$ is different of zero even by small amounts due to the huge difference in the exponential factor. To be more specific, if we take the dimensionless circuit parameters $E_J = 1$, $E_{C_J} = 20$, $E_L = 1/150$ and $E_C = 1/35$, the threshold $f_{x,\text{threshold}}$ which leads to $|V_{-,1}| \geq 10|\beta|$ is

$$|f_{x,\text{threshold}} - \pi/2| = 5.4 \times 10^{-4}. \tag{2.109}$$

In this regime, the energy gap is

$$E_1 - E_0 \approx 2V_{-,1} + \frac{\beta^2}{V_{-,1}}. \tag{2.110}$$

The band is plotted in figure 2.10.

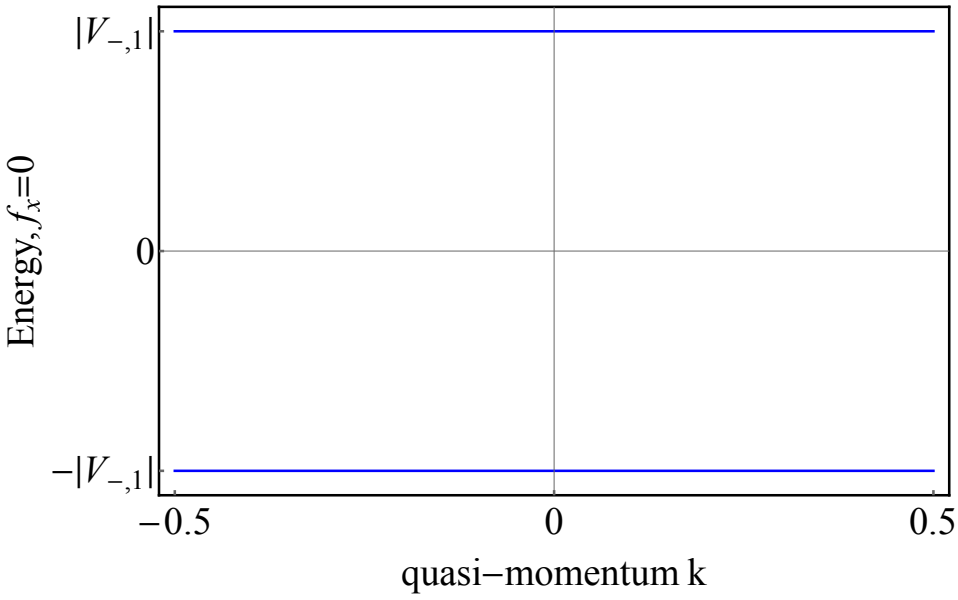


Figure 2.10: The band structure when the external flux $f_x = 0$. The dimensionless circuit parameters are $E_J = 1$, $E_{C_J} = 20$, $E_L = 1/150$ and $E_C = 1/35$. The dependence on the quasi-momentum is so small that it is invisible in the figure.

We note that compared to the first case, the band is shorter and only one state is possible for each band. The gap is of the order of $V_{-,1}$, which is significantly larger than the gap in the first case, which is of the order of $\beta$. Compared to the gap, the bandwidth is negligible. Although the gap of the lowest two states is larger, we can still take the two levels as a nearly degenerate subspace. The wavefunction in this case is very different from the previous one. To have a compact expression, we define

$$\cot 2\theta = \frac{V_{-,1}}{\beta}. \tag{2.111}$$

The two solutions are,

$$\begin{pmatrix} A_{k,1} \\ B_{k,1} \end{pmatrix} = \begin{pmatrix} \sin\theta \\ \cos\theta \end{pmatrix}, \tag{2.112}$$

and

$$\begin{pmatrix} A_{k,2} \\ B_{k,2} \end{pmatrix} = \begin{pmatrix} \cos\theta \\ \sin\theta \end{pmatrix}. \tag{2.113}$$

When $|V_{-,1}| \gg \beta$, $\theta$ approaches $\pi$ and either $A_k$ or $B_k$ is small in the solution. Therefore, the solution consists of ground state of wells in $R = 2n\pi$ or $R = 2n\pi + \pi$, with $n$ an integer.

When $|V_{-,1}|$ is comparable to $|\beta|$, the band structure is shown in figure 2.11. However, the external flux $f_x$ is hard to confine in such a small region in experiment.

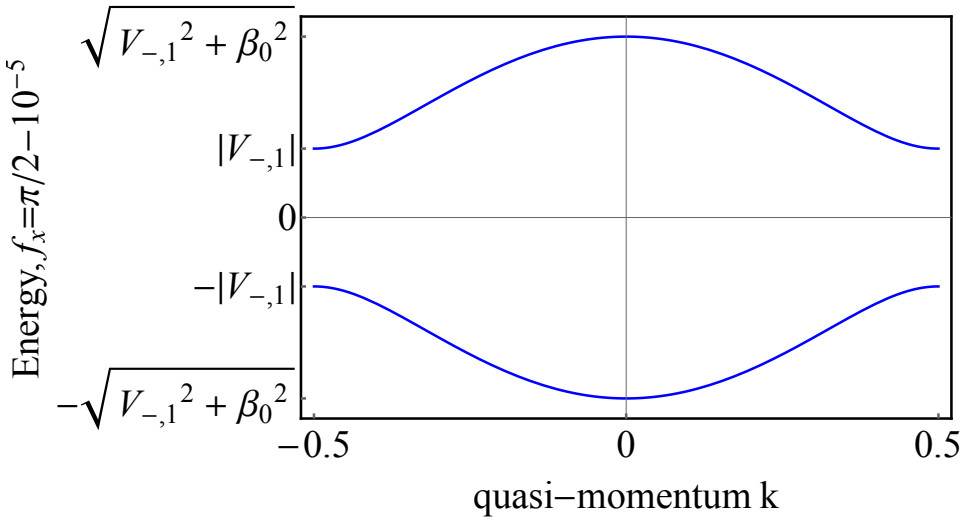


Figure 2.11: The band structure when the external flux $f_x = \pi/2 - 1 \times 10^{-5}$. We define $\beta_0 = |\beta/\cos(k\pi)|$ for simplicity. The dimensionless circuit parameters are $E_J = 1$, $E_{C_J} = 20$, $E_L = 1/150$ and $E_C = 1/35$.

In this section we derived a very important equation to the zero-pi qubit. Equation 2.105 gives the energies of the two-fold nearly-degenerate subspace of the zero-pi qubit. The two-level system is controlled by the external flux $f_x$ and the offset charge $n_{g-}$. We will discuss the properties of noise in the next sections.

Before concluding, we review the Born-Oppenheimer approximation, which was one important step in these calculations. We can now check whether dropped terms are truly negligible. We recall the equation

$$\langle \Psi_{ml} | H_{\text{drop}} | \Psi_{nk} \rangle = -\frac{E_{C-}}{4} \left( 2 \langle \psi_{ml} | \langle f_l | \frac{\partial}{\partial \gamma_-} | f_k \rangle \frac{\partial}{\partial \gamma_-} | \psi_{nk} \rangle + \langle \psi_{ml} | \langle f_l | \frac{\partial^2}{\partial \gamma_-^2} | f_k \rangle | \psi_{nk} \rangle \right). \tag{2.41 revisited}$$

Here, the state $|f_k\rangle$ and the state $|\psi_{nk}\rangle$ describes the wavefunction of $\gamma_+$ and $\gamma_-$ respectively. We only need to consider the dropped term in the nearly degenerate subspace, because other states are far from the qubit states in the spectrum, and tunneling between those states and the qubit states are suppressed by the large energy gap. When dealing with the nearly-degenerate subspace, we set $k = l = 0$, and the integration only goes near $\gamma_- = n\pi$ with an integer $n$ because the wavefunctions are localized in the wells. Moreover, the wavefunction $|f_0\rangle$ depends on $\cos(\gamma_-)$, which has zero derivative around $n\pi$. Therefore we neglect the first term in the bracket. For the second term in the bracket, $\langle f_0 | \partial^2/\partial\gamma_-^2 | f_0 \rangle$ is a slow varying term and can be taken as a constant in the wavefunction integration. The second term becomes $\langle \psi_{m0} | \psi_{n0} \rangle$ and has no net contribution to the Hamiltonian. These considerations establish the validity of the Born-Oppenheimer approximation.

## 2.5 Simulations

We pause the theoretical analysis and turn our attention to the numerical simulation in this section. The numerical results on one hand verify the derivations we have had above. And more importantly, they provide a visualization of the spectrum and the wavefunctions of the qubit, which help us deepen the understanding of the system. This section is planned as following: firstly we introduce the methods concerned with the basis and the matrix elements. Secondly, we show the numerical results on the spectrum and the wavefunctions, and compare them with the theoretical result we obtained in the previous section.

Essentially we aim at solving the Schrödinger equation for the Hamiltonian defined by equation 2.37,

$$H_{+-} = \frac{1}{4} E_{C_J} (n_+ - n_{g+})^2 + \frac{1}{4} E_{C-} (n_- - n_{g-})^2 + E_L (\gamma_+ - f_x)^2 - 2E_J \cos\gamma_- \cos\gamma_+. \tag{2.37 revisited}$$

A conventional method is to express the Hamiltonian in the Cooper-pair number basis $\{(n_+, n_-)\}$. The basis is discrete and can be naturally expressed in matrix form. However, because of the existence of the inductance, the $2\pi$-periodicity of $\gamma_+$ is broken and hence the number operator $n_+$ does not have an integer spectrum. Instead, we consider the Fock basis to express the $n_+$ part, leading to a discrete representation. The Fock basis corresponds to the eigenstates of the Hamiltonian defined by

$$H = \frac{1}{4}E_{C_J}(n_+ - n_{g+})^2 + E_L(\gamma_+ - f_x)^2. \tag{2.114}$$

We label each eigenstate by a positive integer $n_{\text{ho}}$. Therefore, we can use the integer pairs $(n_{\text{ho}}, n_-)$ to label the state in the basis. Expressed in the $\{(n_{\text{ho}}, n_-)\}$ basis, the Hamiltonian becomes,

$$H_{+-} = \hbar\omega_c a^\dagger a + \frac{1}{4}E_{C_-}(n_- - n_{g-})^2 - \frac{1}{2}E_J(b + b^\dagger)(D(iA)e^{if_x} + D(-iA)e^{-if_x}). \tag{2.115}$$

Here, the ladder operators $a$ and $a^\dagger$ are associated with the Fock state in $\gamma_+$ space, while operators $b$ and $b^\dagger$ shifting the state label $n_-$ by -1 and 1 respectively. Note that the operator $b$ is not a ladder operator. Rather, it follows the rule

$$b\,|n_-\rangle = |n_- - 1\rangle\,. \tag{2.116}$$

In the last term of the Hamiltonian $H_{+-}$ in equation 2.115, the displacement operator $D(iA)$ is defined as,

$$D(\alpha) = e^{\alpha a - \alpha^* a^\dagger}, \tag{2.117}$$

and its value in matrix can be determined with the help of equation 2.45, which we restate here,

$$D(\alpha)\,|n\rangle = |n, \alpha\rangle = \sum_{m=0}^{\infty}\left(\frac{n!}{m!}\right)^{\frac{1}{2}}\alpha^{m-n}e^{-\frac{|\alpha|^2}{2}}\mathcal{L}_n^{m-n}\,|m\rangle\,. \tag{2.45 revisited}$$

Also we used $\hbar\omega_c = \sqrt{E_{C_J}E_L}$, and $A = (E_{C_J}/E_L)^{1/4}/2$ in the expression of the Hamiltonian to help simplify the equation. The matrix elements can be straightforwardly calculated.

To obtain reliable results, the size of the matrix has to be carefully chosen. Ideally, an infinite large matrix can fully reflect the reality. However, a compromise must be reached which reflects the limits of computational power. In this problem, we truncate the high energy states, because we are interested in the lowest states, and therefore the basis states with high energy are expected to play a small role. We use two matrices with different size to represent the subspaces $\gamma_+$ and $\gamma_-$. We intentionally set the size differently to maximize

the accuracy while keeping the computing task manageable. The sizes are determined according to the convergence of the simulation result. We examine the energy gap of the lowest two states at $f_x = \pi/4$ and $n_{g_-} = 0$, which is the smallest energy gap we are interested. We plot the energy gap against the matrix sizes of $\gamma_+$ and $\gamma_-$, which is shown in figure 2.12. The energy gap displays a negligible change with basis size when the matrix sizes are larger than 70 and 30 respectively. Practically, we set the sizes of matrices to be $100 \times 100$ for both $\gamma_-$ and $\gamma_+$, because the time of computation for these sizes is less than 1 s, which does not constrain us.

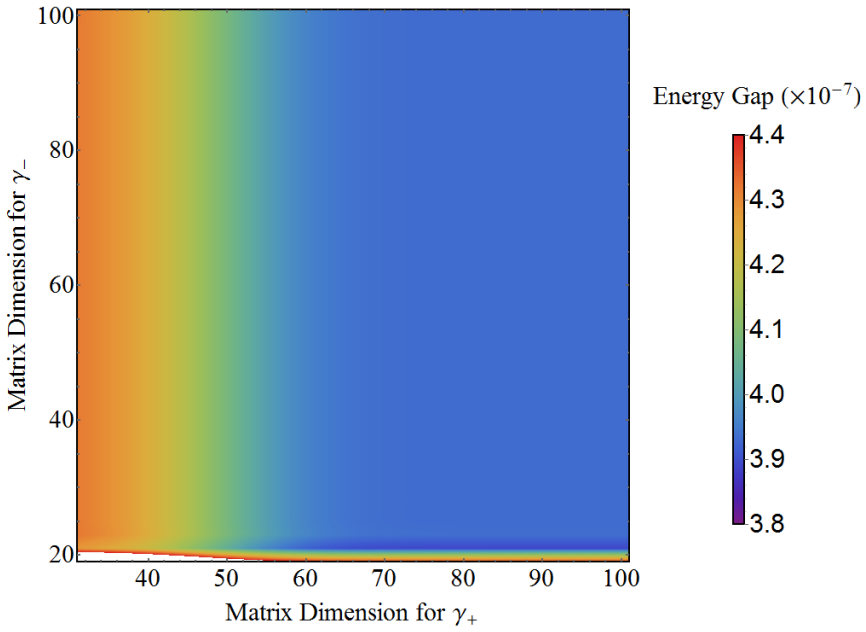


Figure 2.12: The energy gap between the lowest two states. The dimensionless circuit parameters are $E_J = 1$, $E_{C_J} = 20$, $E_L = 1/150$, and $E_C = 1/35$. We set external flux $f_x = \pi/2$ thus $V_{-,1}$ vanishes. We also set the offset charge $n_{g_-} = 0$. The gap converges to $3.93 \times 10^{-7}$ when the matrix size is larger than 70 and 30 respectively.

There are four energies that need to be specified: Josephson energy $E_J$, capacitance energy of the Josephson junction $E_{C_J}$, capacitance energy of the capacitors $E_C$, and inductance energy $E_L$. In the numerical simulation we use the dimensionless energies: $E_J = 1$, $E_{C_J} = 20$, $E_L = 1/150$, and $E_C = 1/35$. These parameters can be achieved by a circuit with $2 \times 10^{-3}$ μm$^2$ Niobium Josephson junctions [49]. The critical current density is 64.4 μA/μm$^2$ and the capacitance density is 60.5 fF/μm$^2$ [50]. The capacitance of the large

capacitor is thus 84.74 fF, which is achieved in the transmon qubit [51]. The inductance of the inductor is 0.38 µH. The inductance is slightly larger than but comparable to the reported value in a fluxonium qubit [12]. The numbers are selected based on three considerations. First, they are viable with the current technologies. Second, parameters should be in the range that the approximations are satisfied. Third, the circuit achieve a good protection to the qubit.

With the selected parameters of circuit elements, we simulate the spectrum and wavefunctions with different combinations of $f_x$ and $n_{g_-}$. Because the $\gamma_{\text{ho}}$ is isolated from $\gamma_+$ and $\gamma_-$, we do not include it in the calculation. Fixing the offset charge $n_{g_-} = 0$, we plot the spectrum of lowest six states against the external flux in the figure 2.13.

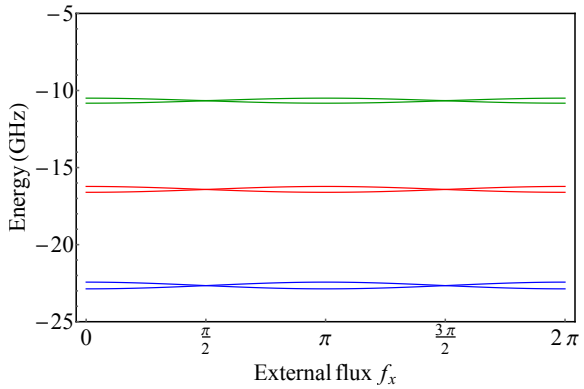


Figure 2.13: The energy spectrum, including the lowest six levels. We fix the offset charge $n_{g_-} = 0$ and plot over the external flux.

The energy gap between the first excited state and the second excited state is $\sim 6.25$ GHz, while the theory gives $\Delta E_{02} \approx \sqrt{2|E_{C_-} V_{-,2}|} = 7.12$ GHz. To further compare the simulation result with the approximation, we plot the energy gap between the first two states over external flux in figure 2.14.

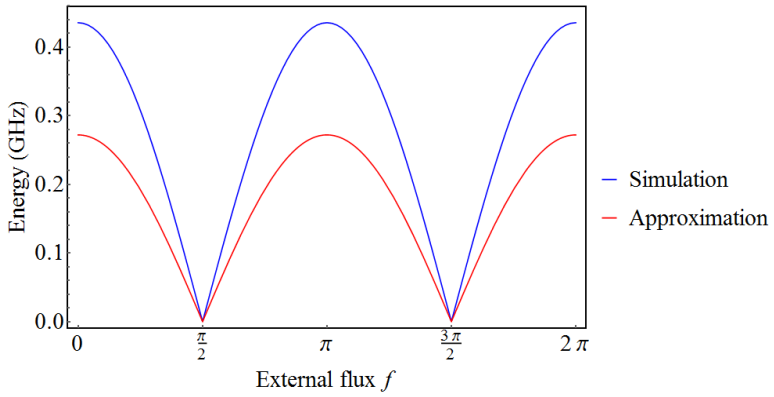


Figure 2.14: The energy gap of the lowest two levels against the external flux. The offset charge is fixed $n_{g_-} = 0$. The blue lines shows the result of simulation, and the red line shows the result from theoretical analysis in equation 2.105.

An interesting case is when external flux $f_x = \pi/2$, the $V_{-,1}$ vanishes and the energy gap can be tuned by $n_{g_-}$. The energy gap is plotted against offset charge $n_{g_-}$ in figure 2.15. Note that the energy gap in this case is in the order of 20 kHz, which is significantly smaller than the energy gap between first and second excited states, which is larger than 6.25 GHz.

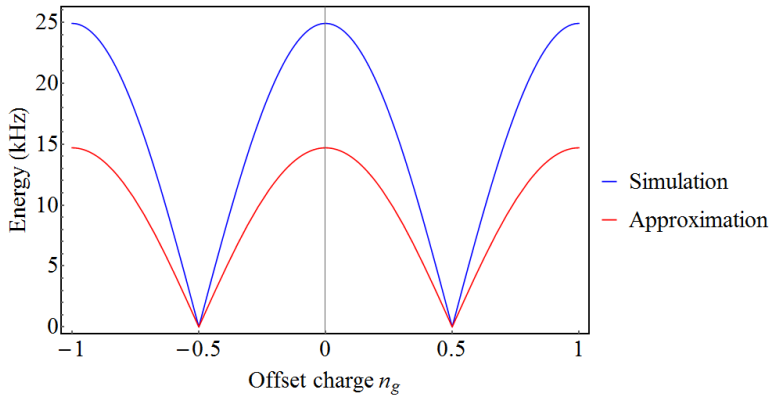


Figure 2.15: The absolute value of the energy gap of the lowest two levels against the offset charge. The external flux is fixed $f_x = \pi/2$. The blue lines shows the result of simulation, and the red line shows the result from theoretical analysis in equation 2.105.

The energy gap predicted by the approximation is smaller than the simulation result. The deviation mainly comes from the inaccuracy of the BO approximation. We assumed

the state in $\gamma_+$ space always stays in the ground state, based on the assumption that the energy to excite the system is large compared to the energy splitting of lowest levels. However, the energy gap between the ground state and the first excited state of $\gamma_+$ space is about 23.36 GHz, which is just a few times larger than the energy gap between the ground state to the second excited state, which is 6.25 GHz. Thus the tunneling process involves excited states in $\gamma_+$ space, whose contribution is not considered in the BO approximation but not negligible.

At last, we plot the wavefunctions of the lowest two states in the figure 2.16. The wavefunctions have two patterns: when the external flux $f_x = 0$, the wavefunction is located near either $\gamma_- = 0$ *or* $\gamma_- = \pi$; when the external flux $f_x = \pi/2$, the wavefunction is located near $\gamma_- = 0$ *and* $\gamma_- = \pi$.

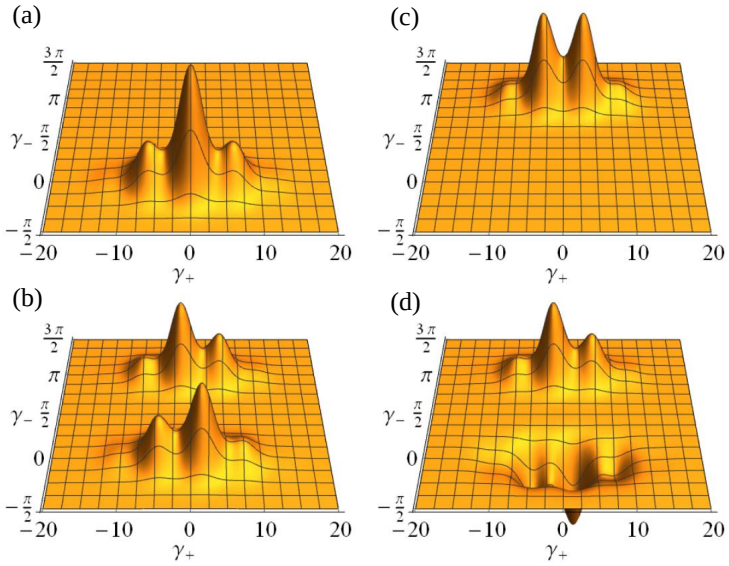


Figure 2.16: The wavefunction of the lowest two states. (a),(b): $f_x = 0$ and $n_{g_-} = 0$. (c)(d): $f_x = \pi/2$ and $n_{g_-} = 0$.

## 2.6 Flux and charge noise

In this section we analyse the decoherence processes in the zero-pi qubit. In the following subsections, we calculate the dephasing time and relaxation time of the zero-pi qubit due to flux noise and charge noise, at and away from the flux sweet spot.

### 2.6.1 Decoherence at the flux sweet spot

Dephasing is caused by processes which induce changes to the transition frequency of the qubit. In Section 2.1 we showed that the offset charge coupled to inductors does not affect the spectrum, thus the offset charge fluctuation on $n_{g_+}$ and $n_{g_{\text{ho}}} = n_{g_3} + n_{g_4}$ does not lead to the pure dephasing. To calculate the dephasing induced by $n_-$ and the flux noise, we start from equation 2.105. We neglect the zero-point energy and replace $k$ with $-n_g$ to obtain

$$\begin{pmatrix} V_{-,1} & \beta \\ \beta & -V_{-,1} \end{pmatrix} \begin{pmatrix} A_k \\ B_k \end{pmatrix} = E_k \begin{pmatrix} A_k \\ B_k \end{pmatrix}. \qquad \text{(2.105 revisited)}$$

We express the energy $V_{-,1}$ and $\beta$ in terms of the circuit parameters:

$$V_{-,1} = 2E_J \cos f_x e^{-\frac{1}{8}\sqrt{E_{C_J}/E_L}} \tag{2.118}$$

and

$$\beta \approx -3.8 \cos(k\pi) E_C e^{-8\sqrt{2}\sqrt{\frac{E_J^2}{E_C E_{C_J}}}} \left(\frac{E_J^2}{E_C E_{C_J}}\right)^{3/4}. \tag{2.119}$$

Here, we approximate $E_{C_-} = \frac{E_C E_{C_J}}{E_C + E_{C_J}} \approx E_C$. We also approximate $V_{-,2} = E_0^{(2)}/2\cos^2\gamma_- \approx -\frac{4E_J^2}{E_{C_J}}$ according to equation 2.53. We tolerate the accuracy loss associated with these approximations in order to establish a simple relation between circuit parameters and qubit parameters.

We estimate the decoherence times based on the parameters we applied in the simulation section, which are $E_J/h = 64$ GHz, $E_{C_J}/h = 1280$ GHz, $E_C/h = 1.83$ GHz, and $E_L/h = 0.427$ GHz. These parameters yield $V_{-,1}/h = 0.13$ GHz$\times \cos f_x$, and $\beta/h = 3.34$ kHz $\times \cos(2\pi n_g)$. A "sweet point" is $f_x = 0$, where the first order sensitivity of the flux noise is eliminated. Moreover, the charge noise is also suppressed by a factor of $\beta/V_{-,1}$ [52], which is also optimized when $f_x = 0$. There is also a "sweet point" for the offset charge. However, because the dependence on the offset charge is so weak that the influence of the offset charge noise is negligible, and tuning to the "sweet point" is unnecessary. For convenience we denote the energy $V_{-,1}$ at $f_x = 0$ by $\frac{1}{2}\Delta$, and we also use the parameter $\beta_0 = |\beta/\cos(k\pi)|$.

We consider the case of the flux sweet spot. We expand the Hamiltonian up to second order in the flux fluctuations:

$$H = \frac{\Delta}{2}\left(\sigma_z + \frac{f_x^2}{2}\sigma_z + \frac{2\beta_0}{\Delta}\cos(\pi n_{g_-})\sigma_x\right). \tag{2.120}$$

Because the factor $\frac{2\beta_0}{\Delta} = 2.5 \times 10^{-5} \ll 1$, the dephasing induced by the offset charge noise of the $n_-$ part is negligible. For the flux noise, the dephasing process is in the situation of quadratic longitudinal coupling. The flux noise is taken to be $1/f$ noise, that is its power spectral density (PSD) is given by

$$S_f(\omega) = F_0^2/|\omega|, \tag{2.121}$$

where $F_0$ is the magnitude of the noise. We take $S_f(\omega)$ to be the double-sided PSD. The effect of quadratically coupled $1/f$ noise on the coherence function $P(t)$ is described by [52]:

$$|P(t)| = \left[1 + \left(\frac{\Delta}{h} F_0^2 t \ln \frac{1}{\omega_{\rm ir} t}\right)\right]^{-1/4}, \tag{2.122}$$

when $\Delta F_0^2 t/h \ll 1$. The infrared cutoff $\omega_{\rm ir}$ is set as the inverse of the total experiment time, and we use $2\pi \times 10^{-4}$. The representative value of $F_0$ is $3.5 \times 10^{-6}$ (converted from the upper bound in [53]). With the numbers above, we find at 1 s, the phase information is well-protected:

$$|P(t)| = 0.9991. \tag{2.123}$$

The dephasing time $T_2^*$, corresponding to significant loss of coherence, can be estimated as [54]

$$T_2 \approx \left|\pi^2 F_0^2 \frac{\Delta}{4\hbar}\right|^{-1} = 40 \text{ s}. \tag{2.124}$$

We now discuss relaxation at the flux sweet spot. The total relaxation time $T_1$ due to flux and charge is given by

$$\frac{1}{T_1} = \frac{1}{T_1^{f_x}} + \frac{1}{T_1^{n_{g_+}}} + \frac{1}{T_1^{n_{g_{\rm ho}}}} + \frac{1}{T_1^{n_{g_-}}}, \tag{2.125}$$

where the first rate on the right hand side correspond to flux induced relaxation and the last three rates correspond to charge induced relaxation. We argue that none of these sources has a significant contribution to energy relaxation. We start with the analysis of the last term. For the charge noise coupling to the $n_-$, the coupling factor is significantly smaller than the energy gap of the qubit, by a factor of $10^5$. Therefore, the influence of $T_{n_{g_-}}$ is negligible. The degree of freedom $n_{\rm ho}$ is decoupled from the core part. Thus its dynamics does not affect the qubit. The relaxation process through $n_+$ is more complicated. Based on the result in Section 2.1, the charge noise in the inductor is equivalent to the charge

noise on the neighbor island with a position-related factor. Therefore we can estimate the relaxation in $n_+$ channel by

$$\frac{1}{T_1^{n_{g_+}}} = \frac{E_{C_J}^2}{2\hbar^2} S_{n_{g_+}}(\Delta/\hbar) \left|\langle g| \, n_+ \, |e\rangle\right|^2 . \tag{2.126}$$

Here $S_{n_{g_+}}(\Delta/\hbar)$ is the PSD of the effective charge noise at the qubit frequency, and $|g\rangle$ and $|e\rangle$ are the qubit states. According to the theoretical analysis, $|g\rangle$ and $|e\rangle$ have the same wavefunctions in $\gamma_+$ space, which we denote as $|\psi\rangle$. Because the wavefunction is a real function of $\gamma_+$. We also know that $\langle n\rangle$ must be real, which can be written as,

$$\langle\psi| \, n_+ \, |\psi\rangle = -i \, \langle\psi| \, \frac{\partial}{\partial\gamma_+} \, |\psi\rangle . \tag{2.127}$$

Because $|\psi\rangle$ is a real function of $\gamma_+$, $\frac{\partial}{\partial\gamma_+}|\psi\rangle$ must be real. Hence the value of $\langle n\rangle$ must be 0, and the $n_{g_+}$ noise also have no contribution to the relaxation. As a result, we approximate the relaxation as,

$$\frac{1}{T_1} = \frac{1}{T_1^{f_x}}. \tag{2.128}$$

The flux noise also does not induce the relaxation in the first order approximation result. The system is coupled to the external flux noise though $\gamma_+$ and $\gamma_{\text{ho}}$, see equation 2.36. The relaxation does not occur through $\gamma_{\text{ho}}$ as the degree of freedom has been decoupled from the qubit levels. The relaxation time through $\gamma_+$ is given by

$$\frac{1}{T_1^{f_x}} = \frac{E_L^2}{\hbar^2} S_f(\Delta/\hbar) \left|\langle g| \, \gamma_+ \, |e\rangle\right|^2 . \tag{2.129}$$

According to the BO approximation result in equation 2.38, we can calculate $\langle g| \, \gamma_+ \, |e\rangle$ as

$$\langle g| \, \gamma_+ \, |e\rangle = \int d\gamma_- \psi_{00}^*(\gamma_-)\psi_{10}(\gamma_-) \int d\gamma_+ f_0^*(\gamma_+;\gamma_-)\gamma_+ f_0(\gamma_+;\gamma_-). \tag{2.130}$$

The second integration can be evaluated up to the first order approximation from equation 2.48 and 2.130:

$$\int d\gamma_+ f_0^*(\gamma_+;\gamma_-)\gamma_+ f_0(\gamma_+;\gamma_-) \approx f_x + \left(\frac{E_{C_J}}{E_L}\right)^{1/4} \left(\langle 0^{(0)}| \, a \, |0^{(1)}\rangle\right), \tag{2.131}$$

where $|0^{(0)}\rangle$ and $|0^{(1)}\rangle$ are the zeroth and first order correction to the ground state in $\gamma_+$ space. At the "sweet point", both $f_x$ and $\left(\langle 0^{(0)}| \, a \, |0^{(1)}\rangle\right)$ are zero and no relaxation is induced in the flux channel.

We have estimated the dephasing and the relaxation of the zero-pi qubit at the "sweet point" where $f_x = 0$. Neither the flux noise nor the charge noise contributes to the relaxation process, while the dephasing time is 40 s. The result shows that the zero-pi qubit is well-protected against the flux noise and the charge noise.

### 2.6.2 Estimate for the dephasing process and relaxation process away from the flux sweet spot

In this subsection we estimate the dephasing and the relaxation times when the qubit is biased away from the "sweet point". We take for definitiveness $f_x = \pi/4$. When away from the "sweet point", the flux qubit has linear coupling component to the spectrum and also introduce relaxation. The estimate of dephasing time at $f_x = \pi/4$ is,

$$T_2 \approx \frac{\sqrt{2\pi}}{F_0}\left(\frac{\sqrt{2}\Delta}{4\hbar}\right)^{-1} = 1.2 \text{ ms}. \tag{2.132}$$

The charge noises estimation does not change while we reevaluate of the flux noise contribution. We revisit 2.131,

$$\int d\gamma_+ f_0^*(\gamma_+;\gamma_-)\gamma_+ f_0(\gamma_+;\gamma_-) \approx f_x + \left(\frac{E_{C_J}}{E_L}\right)^{1/4}\left(\langle 0^{(0)}|\, a\, |0^{(1)}\rangle\right). \qquad \text{(2.131 revisited)}$$

At $f_x = \pi/4$ we have

$$\left(\frac{E_{C_J}}{E_L}\right)^{1/4}\left(\langle 0^{(0)}|\, a\, |0^{(1)}\rangle\right) = \frac{\sqrt{2}E_J}{2E_L}\exp\left(-\frac{1}{4}\sqrt{\frac{E_{C_J}}{E_L}}\right)\cos(\gamma_-). \tag{2.133}$$

Then we can evaluate 2.43,

$$\langle g|\, \gamma_+\, |e\rangle = \frac{\sqrt{2}E_J}{2E_L}\exp\left(-\frac{1}{4}\sqrt{\frac{E_{C_J}}{E_L}}\right)\int d\gamma_- \psi_{00}^*(\gamma_-)\cos(\gamma_-)\psi_{10}(\gamma_-). \tag{2.134}$$

The integration can be calculated by the WKB approximation but an approximation can be given with ease. We neglect the overlap of the wavefunctions in different wells and approximate $\cos(\gamma_-)$ by a step function,

$$s(\gamma_-) = \begin{cases} 1, & \cos(\gamma_-) \geq 0, \\ -1, & \cos(\gamma_-) < 0. \end{cases} \tag{2.135}$$

The integration becomes $A^*_{k,1}A_{k,2} - B^*_{k,1}B_{k,2} = 2\sin 2\theta \approx \beta/V_{-,1}$, see equation 2.112 and 2.113. With the circuit parameters we give the estimation of relaxation,

$$\frac{1}{T_1^{f_x}} \approx 8 \times 10^{-18} \text{ Hz}, \tag{2.136}$$

indicating the relaxation contribution from the flux noise is negligible.

## 2.7 Conclusions

The zero-pi qubit is a qubit design that focuses on the protection against various noise sources. This qubit has a symmetric structure with identical pairs of Josephson junctions, capacitors, and inductors. Among the three degrees of freedom, one describes the harmonic oscillation of the LC component and can be decoupled from the other degrees of freedom, which are critical in forming the qubit levels. Of these two degrees of freedom, one has a large kinetic energy coefficient compared to the other one, allowing the use of the BO approximation to simplify the system into a one-dimensional problem. The one-dimensional problem is analog to a particle in a $\pi$-periodic potential with a $2\pi$-periodic perturbation. The qubit states are the lowest two states of this one-dimensional problem.

We calculated the dephasing time and relaxation time in the flux and charge channels. The qubit shows excellent isolation against charge noise sources. No charge noise channel can be a significant source for dephasing or relaxation processes. At the same time, the dephasing time due to the flux channel is about 40 s at the "sweet point" and over 1 ms when biased at $f_x = \pi/4$. Relaxation due to flux noise at the sweet spot is negligible, whereas $T_1^{f_x} = 10^{18}$ s at the bias point $f_x = \pi/4$. We conclude that the qubit shows high resistance against flux and charge noises, and has large anharmonicity, which are important characteristics of a good qubit.

We also showed a practical method to describe the qubit and its dynamics. By using a series of approximations we obtain the qubit Hamiltonian parameters and we show that approximations are well justified.

Only a few studies of the zero-pi qubit have been done up to this date. Our work demonstrates resistance against flux and charge noise, whereas previous work addressed the role of circuit parameter disorder [35] and the potential to carry protected qubit gates [36]. However, how to measure the qubit state while keeping its protection unbroken is an open question. In addition, the proposed protected gates [36] could not form a universal operation set, thus either we have to tolerate some unprotected gates or we need to find more protected gates.

# Chapter 3

# Floquet state dynamics

In this chapter, we study the qubit dynamics under strong driving. Sending monochromatic microwave pulses to the superconducting circuit is a standard method to perform qubit gates [18]. With weak signals, the qubit evolution is simple as its behavior can be described using rotating wave approximation (RWA) [55]. But weak signal has its drawback on gate speed. To achieve as many qubit gates as possible in a certain time, a fast and accurate qubit gate is desirable. One approach to realizing the fast gate is using strong driving signals, but strong driving breaks the rotating wave approximation (see Section 3.5). As a result, a qubit behaves more irregularly than that in the weak driving condition. Our study focuses on building a more general model that can express the qubit behavior in strong driving condition.

The Hamiltonian we use to describe a driven qubit is relatively simple. It contains a Hamiltonian of the qubit and an extra term expressing the microwave drive. Despite the simplicity of the Hamiltonian, the solution to the Schrödinger equation is time-dependent and very complicated. Moreover, directly solving the differential equation is a hard task. Instead, we apply the Floquet theory [56] which is a mathematical method for periodic differential equations. In the frame of Floquet theory, we can obtain the solution of the system by calculating the eigenvalues and eigenstates of the Floquet operator, and avoid solving the differential equation directly.

In Section 3.1 we review the Floquet theory and its application to a driven qubit. We realize the strong driving condition experimentally, and we introduce the experimental settings in Section 3.2. We also simulate the system to assist the analysis. The simulation results are presented in Section 3.3. In Section 3.4, we finalize the model that can explain what we observe in the experiment. The relation between our model and the model based

on RWA method is discussed in Section 3.5.

Note that for simplicity in this chapter we use the dimensionless unit where $\hbar = 1$.

## 3.1 Floquet theory

In this section we introduce the basics of the Floquet theory that we will use in the following sections. The Floquet theory was originally developed to solve periodic differential equations [56]. In quantum mechanics, this framework suitable to solve a system with a periodic time-dependent Hamiltonian. We consider the Schrödinger equation,

$$i\frac{d}{dt}\left|\psi(t)\right\rangle = H(t)\left|\psi(t)\right\rangle, \tag{3.1}$$

where the Hamiltonian is periodic in time and satisfies $H(t+T) = H(t)$. According to the Floquet theory, the solutions are in the form:

$$\left|\Psi_\alpha(t)\right\rangle = e^{-i\epsilon_\alpha t}\left|u_\alpha(t)\right\rangle. \tag{3.2}$$

The state $\left|\Psi_\alpha(t)\right\rangle$ is called Floquet state and the state $\left|u_\alpha(t+T)\right\rangle = \left|u_\alpha(t)\right\rangle$ is a periodic Floquet mode. The quasienergy $\epsilon_\alpha$ is a constant, and can be determined along with the Floquet modes by

$$\mathcal{H}\left|u(t)\right\rangle = \epsilon\left|u(t)\right\rangle, \tag{3.3}$$

where $\mathcal{H} = H(t) - i\frac{d}{dt}$.

If we start with a Floquet state $\left|\Psi_\alpha(t)\right\rangle = e^{-i\epsilon_\alpha t}\left|u_\alpha(t)\right\rangle$, we can obtain another set of quasienergy and Floquet mode by shifting the phase,

$$\left|\Psi'_\alpha(t)\right\rangle = e^{-i(\epsilon_\alpha + 2\pi/T)t}\left|u'_\alpha(t)\right\rangle, \tag{3.4}$$

where $\left|u'_\alpha(t)\right\rangle = e^{2i\pi t/T}\left|u_\alpha(t)\right\rangle$. Apparently $\left|\Psi'_\alpha(t)\right\rangle$ and $\left|\Psi_\alpha(t)\right\rangle$ are the same state, and the new quasienergy $\epsilon_\alpha + 2\pi/T$ is an alias of $\epsilon_\alpha$. In fact, each quasienergy is accompanied by an infinite set of alias. To properly label these states and energies, we use double subscripts for each quasienergy, i.e. $\epsilon_{\alpha,n}$. The subscript $\alpha$ is a positive integer and labels the physical states, while $n$ is an integer labels the alias. For each fixed $\alpha$, the quasienergy differs by $2\pi/T$ when the label $n$ differs by 1. For example,

$$\epsilon_{\alpha,n} = \epsilon_{\alpha,n-1} + 2\pi/T. \tag{3.5}$$

We select $\epsilon_{\alpha,0}$ in the First Brillouin zone $-2\pi/T < \epsilon_{\alpha,0} < 2\pi/T$. When $n = 0$ we omit the subscript $n$ for simplicity.

## 3.2 Experimental setup

We run an experiment to observe the qubit behavior in strong driving condition. We use a superconducting flux qubit as the driven system. The lowest two states of the flux qubit are close to each other, while the third state has a large energy gap to the lowest states. Thus flux qubit can be regarded as a two-state qubit system. Also, the flux qubit has a loop structure and can be tuned by the magnetic flux penetrating the loop, see Section 1.3.2 and [23] for more information on the flux qubit. The coupling between the qubit and the electromagnetic fields is strong, which allows us to reach the strong driving regime.

We couple the qubit with a transmission line resonator for measurement in a circuit quantum electrodynamics architecture [18]. The qubit-resonator system enters the dispersive regime when the cavity frequency significantly differs from the qubit frequency. In the dispersive regime, the cavity frequency is shifted by the qubit and the shift depends on the qubit state. Therefore we measure the cavity frequency to probe the state of the qubit.

The whole sample is enclosed in a copper box and cooled down to 35 mK in a dilution refrigerator. To minimize the environmental magnetic field noise, the box is surrounded by a three-layer high-permeability metal shield. The lower part of the fridge, where the sample is placed, is protected in addition by an active magnetic field compensation system. The signal for qubit control is generated directly by an arbitrary waveform generator (AWG), Tektronix AWG700002A. Using an AWG provides the full access to the signal encoding, which is very difficult in the usual method based on mixers. Moreover, this method avoids the band limit and noise induced by the mixers. The signal is sent through coaxial cables to the superconducting device, with attenuators and filters at each temperature stage. The signal output from the cavity is amplified by a low-noise high electron mobility transistor amplifier with a noise temperature of 4 K.

The sample is fabricated on a high-resistivity silicon substrate. The cavity and the control line are constructed by evaporation of a 190 nm thick aluminum layer, and the qubit is constructed by double shadow evaporation of a 40 nm and a 60 nm aluminum layers. The fundamental frequency of the cavity is $\omega_c = 2\pi \times 6.641$ GHz, and the coupling strength is $g = 2\pi \times 537$ MHz. The qubit frequency is $\omega_q = 2\pi \times 2.288$ GHz, and persistent current is $I_p = 690$ nA. Here the qubit frequency is the dressed qubit frequency, which is shifted from the bare qubit frequency by the qubit-cavity interaction. Scanning electron microscope (SEM) images are shown in figure 3.1.

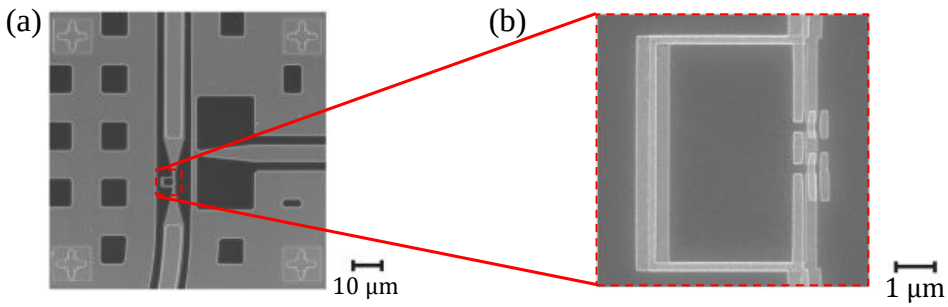


Figure 3.1: (a) SEM image of the qubit (red square) and the resonator. The qubit is controlled by the microwaves coupled to the antenna on the right. (b) SEM image of the qubit. The qubit consists of one large junction and three smaller junctions.

We bias the qubit at its symmetry point, i.e. magnetic flux in the loop is half of a magnetic quantum $\Phi_x = \Phi_0/2$. At the symmetry point, the relaxation time and dephasing time are $T_1 = 1.8$ μs and $T_2^* = 0.3$ μs respectively. The qubit is prepared in the ground state by free relaxation before the driving pulse arrives. The AWG synthesizes the pulse in the form of $A\cos(\omega_d t)$, where $A$ is the amplitude of the signal, in unit of energy, and $\omega_d$ is the driving frequency. At last, we send the probing signal to the cavity to learn the qubit state. Each cycle of relaxation, driving, and probing is repeated for $16,384$ times to average out the noise and determine the excited population of the qubit.

## 3.3 Simulation

The simulation of the qubit dynamics helps us track the qubit dynamics more closely. The first step to set up the simulation is to build the proper model. The qubit, along with the cavity, can be described by the Hamiltonian,

$$H = -\frac{1}{2}\omega_{\text{bare},q}\sigma_z + \omega_c a^\dagger a - \frac{g}{2}\sigma_x(a^\dagger + a), \tag{3.6}$$

where the Pauli matrices $\sigma_z$ and $\sigma_x$ are the operators defined in the qubit space, and the ladder operators $a$ and $a^\dagger$ affect the on the cavity states. The frequencies $\omega_{\text{bare},q}$, $\omega_c$ stands for the bare qubit frequency and the cavity frequency respectively, and $g$ is the coupling factor. Because in this sample the coupling factor $g$ is much smaller than the frequency difference $\Delta = |\omega_{\text{bare},q} - \omega_c|$, the system is in the dispersive regime and we obtained an

effective Hamiltonian by an approximated diagonalization of the Hamiltonian in equation 3.6[18],

$$H = \frac{1}{2}(\omega_{\text{bare},q} + \frac{g^2}{\Delta})\sigma_z + (\omega_c + \frac{g^2}{\Delta}\sigma_z)a^\dagger a. \tag{3.7}$$

The second part of the Hamiltonian indicates that the cavity frequency is affected by the qubit state, which is the theory fundament of qubit state measurements. The first part describes a dressed qubit, which is a two level-system contains ingredients of qubit and cavity. The frequency of the dressed qubit is denoted by $\omega_q$. In the experiment, we are actually manipulating and measuring the system mixed by the qubit and the cavity, but not the qubit along. The parameters are obtained based on fitting the experiment result. For convenience, we omit the word "dressed" and simple refer it as the qubit. The frequency of the qubit is $\omega_q = 2\pi \times 2.288$ GHz.

The validity of separating the cavity and qubit is verified by the simulation. We simulate a simplified model with a qubit alone, and a full system consists of a coupled qubit and a cavity. We simulate the system dynamics of both models under driving signals. The result is shown in figure 3.2. The difference between the simplified model and the full model is very small. We also monitor the photon number expectation value in the cavity, which is less than 0.05 and has a minimal influence on the dynamics. Since no significant difference is addressed between two models, we can safely adopt the simpler model, where the system consists of one qubit.

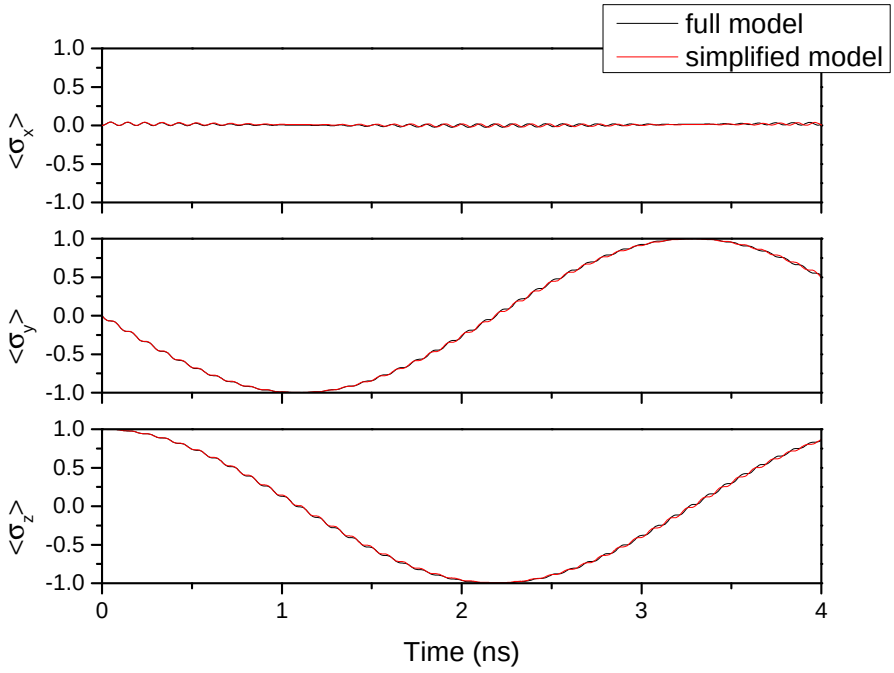


Figure 3.2: Simulation of qubit state tomography in full model and simplified model. The driving amplitude is 0.2288 GHz, which is 1/10 of the qubit frequency. The black line (full model) and the red line (simplified model) almost overlap perfectly.

Now we have arrived the Hamiltonian to simulate the qubit, and we are adding the driving signal. The signal is monochromatic and starts at time $t = 0$, and in the form of $\cos(\omega_d t)$. The time-dependent Hamiltonian for this system is,

$$H = -\frac{\omega_q}{2}\sigma_z + A\cos(\omega_d t)\sigma_x. \tag{3.8}$$

Here, $A$ is the driving amplitude in unit of energy, and $\omega_d$ is the driving frequency. We simulate the real-time dynamics of the qubit in driving in weak and strong driving regimes, and compare them with the experiment data. The result is shown in the figure 3.3. The experiment result and the simulation result match very well.

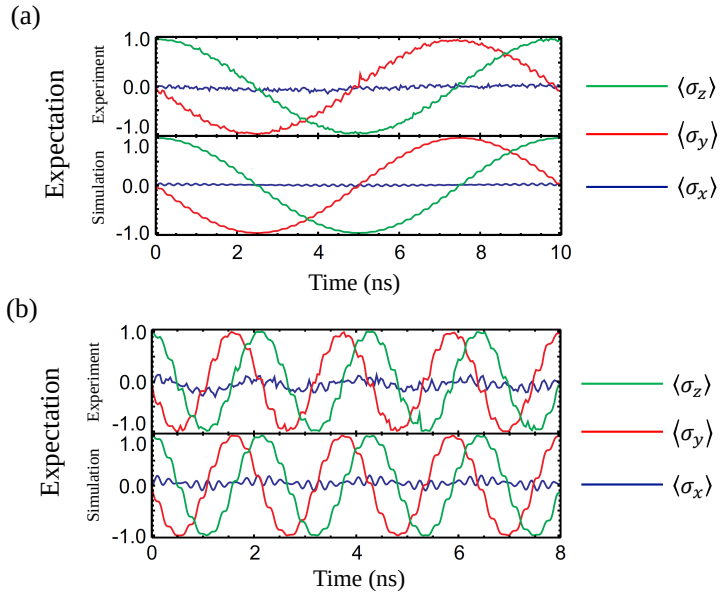


Figure 3.3: Qubit dynamics tomography obtained by experiment measurement and simulation. The amplitudes of the driving force are (a) $A = 2\pi \times 0.1$ GHz and (b) $A = 2\pi \times 0.46$ GHz.

We also apply the discrete Fourier transformation to the time-domain dynamics of the qubit states with different driving strength (figure 3.4). We do not comment on the physics behind these patterns now but leave it to the next section, and we emphasize that the simulation and the experiment results are very similar. As the consequence, the numerical model successfully reflects the real system behavior, and we can use the simulation to have a better understanding of the qubit system.

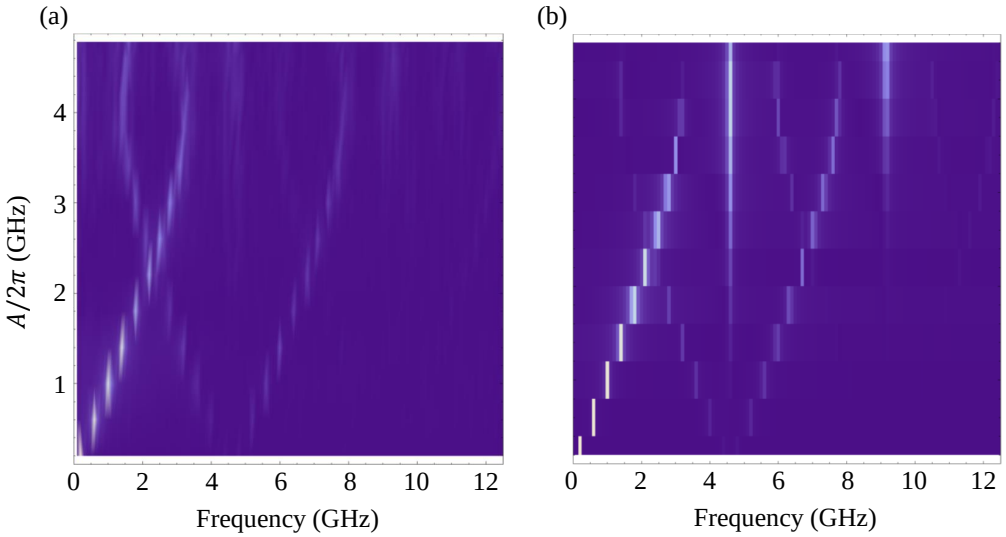


Figure 3.4: Fourier components extracted from the qubit dynamics in (a) experiment and (b) simulation. The lightness of an area reflects the magnitude of the corresponding Fourier component.

## 3.4 Theory

In this section we reveal the physics behind the link between the Fourier pattern in figure 3.4 and the model based on the Floquet theory. The Hamiltonian generating the pattern in given in 3.8, which we revisit here,

$$H = -\frac{\omega_q}{2}\sigma_z + A\cos(\omega_d t)\sigma_x. \qquad \text{(3.8 revisited)}$$

We use the qubit basis, where $|0\rangle$ and $|1\rangle$ represents the ground state and excited state respectively. And we thus define the differential equation,

$$\mathcal{H}\,|u\rangle = \epsilon\,|u\rangle\,, \tag{3.9}$$

where $\epsilon$ is the quasienergy and we define $\mathcal{H}$ as Floquet Hamiltonian,

$$\mathcal{H} = \left(-\frac{\omega_q}{2}\sigma_z + A\cos(\omega_d t)\sigma_x - i\frac{d}{dt}\right). \tag{3.10}$$

According to the Floquet theory, states evolve according to the Hamiltonian in equation 3.8 is a superposition of Floquet states. The number of Floquet states is determined by the dimensions of the Hamiltonian, which is two in our case. We denote $|\Psi_1(t)\rangle$ and $|\Psi_2(t)\rangle$ as the two Floquet states, corresponding to quasienergies $\epsilon_1$ and $\epsilon_2$ respectively, and they fulfill the expression,

$$|\Psi_i(t)\rangle = e^{-i\epsilon_i t} |u_i(t)\rangle , \tag{3.11}$$

where $i = 1, 2$ and the Floquet mode $|u_i(t)\rangle$ is $2\pi/\omega_d$- periodic in $t$ and are the eigenstates to the equation 3.9. We express the Floquet mode in the qubit basis, with time-dependent and periodic coefficients,

$$|u_i(t)\rangle = c_{i,0}(t) |0\rangle + c_{i,1}(t) |1\rangle . \tag{3.12}$$

Because $c_{i,j}(t)$ has a periodicity of $2\pi/\omega_d$, they can be expanded as

$$c_{i,j} = \sum_n d_{i,j,n} e^{in\omega_d t}. \tag{3.13}$$

Then we combine equations 3.12 and 3.13 and insert them in 3.9, which leads to a recurrence relation,

$$\begin{cases} -\frac{\omega_q}{2} d_{i,0,n} + \frac{A}{2} \left( d_{i,1,n+1} + d_{i,1,n-1} \right) - n\omega_d d_{i,0,n} = \epsilon_i d_{i,0,n}, \\ \frac{\omega_q}{2} d_{i,1,n} + \frac{A}{2} \left( d_{i,0,n+1} + d_{i,0,n-1} \right) - n\omega_d d_{i,1,n} = \epsilon_i d_{i,1,n}. \end{cases} \tag{3.14}$$

Before we write the recurrent relation in matrix form, categorizing these coefficients is very helpful to next steps. The coefficients can be placed into two groups and only elements in each group are related by the recurrent relation, while no linked between elements in different groups. An easy way to determine the belonging of an element is to look at the sum of the last two indexes: if it is odd, the element belongs one group which we name "odd"; otherwise it goes to the other group called "even". For example, $d_{i,0,2}$ are in the "even" group while $d_{i,2,3}$ are in the "odd" group. For a fixed index $i$, two groups are isolated from the recurrence relation to each other and each group can be solved individually. As a result, we have two set of recurrent relations at hand and we express them in two matrices. The matrix for group "even" is,

$$M_{\text{even}} = \begin{pmatrix} \ddots & & & & & & \\ & -\frac{\omega_q}{2} - (n-1)\omega_d & \frac{A}{2} & & & & \\ & \frac{A}{2} & \frac{\omega_q}{2} - n\omega_d & \frac{A}{2} & & & \\ & & \frac{A}{2} & -\frac{\omega_q}{2} - (n+1)\omega_d & \frac{A}{2} & & \\ & & & \frac{A}{2} & \frac{\omega_q}{2} - (n+2)\omega_d & & \\ & & & & & \ddots & \end{pmatrix}. \tag{3.15}$$

The basis for the shown part is $d_{i,1,n-1}$, $d_{i,0,n}$, $d_{i,1,n+1}$, $d_{i,0,n+2}$. The matrix for group "odd" is very similar but the sign of $\omega_q$ changes,

$$M_{\text{odd}} = \begin{pmatrix} \ddots & & & & & & & \\ & \frac{\omega_q}{2} - (n-1)\omega_d & & \frac{A}{2} & & & & \\ & & \frac{A}{2} & & -\frac{\omega_q}{2} - n\omega_d & & & \\ & & & \frac{A}{2} & & \frac{\omega_q}{2} - (n+1)\omega_d & & \\ & & & & \frac{A}{2} & & -\frac{\omega_q}{2} - (n+2)\omega_d & \\ & & & & & & & \ddots \end{pmatrix}. \tag{3.16}$$

The basis for the shown part is $d_{i,1,n-1}$, $d_{i,0,n}$, $d_{i,1,n+1}$, $d_{i,0,n+2}$. The eigenvalues of the two matrices are closely related. To see this, we firstly define two matrices,

$$\Omega_1 = \begin{pmatrix} & & & & & \iddots & \\ & & & & 1 & & \\ & & & 1 & & & \\ & & 1 & & & & \\ & \iddots & & & & & \end{pmatrix}. \tag{3.17}$$

and

$$\Omega_2 = \begin{pmatrix} \ddots & & & & & & \\ & 1 & & & & & \\ & & -1 & & & & \\ & & & 1 & & & \\ & & & & -1 & & \\ & & & & & \ddots & \end{pmatrix}. \tag{3.18}$$

Apparently these two matrices $\Omega_1$ and $\Omega_2$ are all orthogonal, i.e. $\Omega\Omega^\dagger = \Omega^\dagger\Omega = \mathbb{1}$. Matrices representing the relation of group "odd" and group "even" can be related through the transformation,

$$M_{\text{even}} = -\Omega_2\Omega_1 M_{\text{odd}}\Omega_1^\dagger\Omega_2^\dagger. \tag{3.19}$$

Therefore, if $\lambda$ is an eigenvalue of matrix $M_{\text{even}}$, we must have

$$0 = \det(M_{\text{even}} - \lambda\mathbb{1}) = -\det\left(\Omega_2\Omega_1(M_{\text{odd}} + \lambda\mathbb{1})\Omega_1^\dagger\Omega_2^\dagger\right). \tag{3.20}$$

And thus $-\lambda$ is an eigenvalue of $M_{\text{odd}}$. Another way to link $M_{\text{even}}$ and $M_{\text{odd}}$ is by adding $\omega_d\mathbb{1}$,

$$M_{\text{odd}} + \omega_d\mathbb{1} = M_{\text{even}}. \tag{3.21}$$

Repeating once more we recover the original matrix,

$$M_{\text{odd}} + 2\omega_d \mathbb{1} = M_{\text{odd}}. \tag{3.22}$$

From these equations, we can tell $M_{\text{even}}$ has eigenvalues $\lambda + 2k\omega_d$ and $-\lambda + (2k+1)\omega_d$ with integer $k$, while $M_{\text{odd}}$ has eigenvalues $-\lambda + 2k\omega_d$ and $\lambda + (2k+1)\omega_d$. For each matrix, there must be one and only one eigenvalue falls in the first Brillouin zone $(-\omega_d/2, \omega_d/2)$, and they are additive inverse because of equation 3.20. We recognize these two eigenvalues as quasienergies $\epsilon$ and $-\epsilon$, corresponding to the eigenvalue found in $M_{\text{even}}$ and $M_{\text{odd}}$ respectively. We know that the number of quasienergies equals the dimension of the Hamiltonian, which is two. Therefore we have found all the quasienergies. Note there is one exception that the matrix has eigenvalue 0, two eigenstate can be mixed up and not confined in $M_{\text{even}}$ or $M_{\text{odd}}$. But this case does not affect our conclusion, and we will discuss it later.

We denote $\epsilon_{\text{even}}$ and $\epsilon_{\text{odd}}$ to the quasienergy found in $M_{\text{even}}$ and $M_{\text{odd}}$ respectively. The eigenvector associated with $\epsilon_{\text{even}}$ contains only elements in group "even", while the other eigenvector has only elements in group "odd". Therefore we can write one Floquet mode derived in "even" group as,

$$|u_{\text{even}}\rangle = f_{\text{even},0}(t)\,|0\rangle + e^{i\omega_d t} f_{\text{even},1}\,|1\rangle \tag{3.23}$$

where $f_{\text{even},0}(t) = \sum_{k=-\infty}^{\infty} d_{\text{even},0,2k} e^{2ik\omega_d t}$ and $f_{\text{even},1}(t) = \sum_{k=-\infty}^{\infty} d_{\text{even},1,2k+1} e^{2ik\omega_d t}$. Note we extracted a factor $e^{i\omega_d t}$ in $f_{\text{even},1}(t)$ and put it explicitly in the equation. It clearly shows that both $f_{\text{even},0}(t)$ and $f_{\text{even},1}(t)$ are periodic functions with angular frequency $2\omega_d$. We draw the similar conclusion on the Floquet mode derived in group "odd",

$$|u_{\text{odd}}\rangle = e^{i\omega_d t} f_{\text{odd},0}(t)\,|0\rangle + f_{\text{odd},1}\,|1\rangle\,, \tag{3.24}$$

where $f_{\text{odd},0}(t) = \sum_{k=-\infty}^{\infty} d_{\text{odd},0,2k+1} e^{2ik\omega_d t}$, $f_{\text{odd},1}(t) = \sum_{k=-\infty}^{\infty} d_{\text{odd},0,2k} e^{2ik\omega_d t}$. For any state that evolves under the driving signal can be expressed by a superposition of Floquet modes,

$$|\psi(t)\rangle = \alpha\,|\Psi_1(t)\rangle + \beta\,|\Psi_2(t)\rangle = \alpha e^{i\epsilon t}\,|u_{\text{even}}\rangle + \beta e^{-i\epsilon t}\,|u_{\text{odd}}\rangle\,. \tag{3.25}$$

Furthermore, we can express it in qubit basis,

$$|\psi(t)\rangle = \left(\alpha e^{i\epsilon t} f_{\text{even},0} + \beta e^{-i\epsilon t} e^{i\omega_d t} f_{\text{odd},0}\right)|0\rangle + \left(\alpha e^{i\epsilon t} e^{i\omega_d t} f_{\text{even},1} + \beta e^{-i\epsilon t} f_{\text{odd},1}\right)|1\rangle\,. \tag{3.26}$$

The probability we obtaining $|1\rangle$ in the measurement is,

$$|\,\langle\psi(t)|1\rangle\,|^2 = |\alpha f_{\text{even},1}|^2 + |\beta f_{\text{odd},1}|^2 + 2\Re\left(\alpha^* \beta e^{i(\omega_d - 2\epsilon)t} f^*_{\text{even},1} f_{\text{odd},1}\right). \tag{3.27}$$

The first two terms are both periodic functions with angular frequency $2\omega_d$. These two terms together contribute to the straight light lines at $2n\omega_d$ with integer $n$ in figure 3.4. The last term lights up the lines at $2n\omega_d \pm (\omega_d - 2\epsilon)$ with integer $n$. We compare the result predicted by this theoretical model and the simulation result in figure 3.5. The model explains all the bright lines appearing in the Fourier space contour plot, thus help us understand the qubit behavior in the strong driving condition.

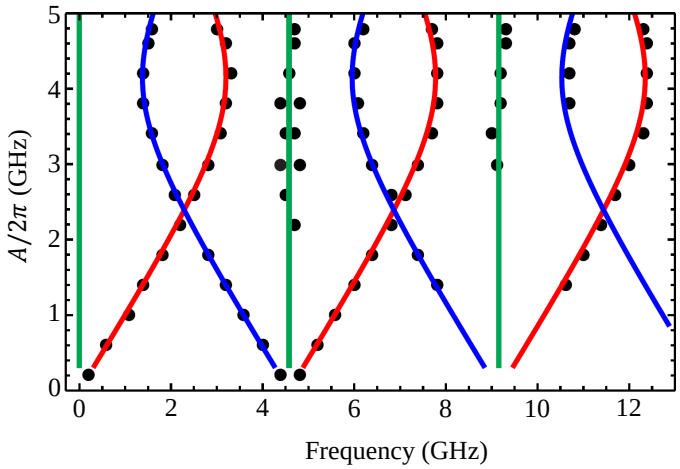


Figure 3.5: Fourier component peaks and theoretical predictions. The black dots shows the peaks which can be observed in the experiment. The solid lines shows $2n\omega_d$ in green, $(2n-1)\omega_d + 2\epsilon$ in red and $(2n+1)\omega_d - 2\epsilon$ in blue.

## 3.5 Relation to rotating wave approximation

In this section we calculate the rotating wave approximation in the resonance case, and show how the RWA is connected to the model we built. We revisit the Hamiltonian of the driven system,

$$H = -\frac{\omega_q}{2}\sigma_z + A\cos(\omega_d t)\sigma_x. \qquad \text{(3.8 revisited)}$$

In the resonance case, the driving frequency $\omega_d = \omega_q$. We choose the frame that rotates at the qubit frequency. The Hamiltonian in the rotating frame becomes,

$$H_{\text{rot}} = \frac{A}{2}\left(1 + \cos(2\omega_q t)\right)\sigma_x - \frac{A}{2}\sin(2\omega_q t)\sigma_y. \tag{3.28}$$

In the rotating wave approximation, we omit the high frequency terms, assuming their effect averages out in the qubit evolution. Therefore the approximated Hamiltonian is,

$$H_{\text{RWA}} = \frac{A}{2}\sigma_x. \tag{3.29}$$

As the result, the measurement gives $|1\rangle$ with probability

$$p = \frac{1}{2}\left(1 - \cos(At)\right), \tag{3.30}$$

given the initial state $|0\rangle$. Now we go back to the model based on Floquet state. The quasienergies can be obtained from matrix in 3.15. With small $A$, the quasienergy can be approximated as,

$$\epsilon = \frac{1}{2}(\omega_q - A). \tag{3.31}$$

Moreover, eigenstates shows $f_{\text{odd},i} \approx 1/\sqrt{2}$, for $i = 0, 1$ and $f_{\text{even},0} = 1/\sqrt{2}$, $f_{\text{even},1} = 1/\sqrt{2}$. We take these numbers into equation 3.27 and we get,

$$|\langle\psi(t)|1\rangle|^2 = |\alpha|^2 + |\beta|^2 + \Re(\alpha^*\beta e^{iAt}). \tag{3.32}$$

If we set initial state as $|\psi(0)\rangle = |0\rangle$, we have $-\alpha = \beta = 1/\sqrt{2}$. Thus we recover the probability function,

$$|\langle\psi(t)|1\rangle|^2 = \frac{1}{2}\left(1 - \cos(At)\right). \tag{3.33}$$

We clearly see that when $A$ is small, the RWA is the first order approximation of the solution in the model based on Floquet theory. When $A$ gets larger, the approximation to the quasienergy and eigenstates do not hold, and the RWA also breaks down.

## 3.6 Conclusion

We designed and executed an experiment where the driving frequency is significantly exceeding the qubit frequency. When the driving signal is strong, we observed deformation in

the Rabi oscillation curve, which is unexpected in the weak driving regime. The simulation confirmed the deformation is not coming from noise. Moreover, the deformation shows a specific pattern if we plot it in the Fourier space, showing the curve contains frequencies $2n\omega_d$ and $(2n+1)\omega_d \pm 2\epsilon$. We built a model based on Floquet theory, which successfully explains the pattern. We also showed in the resonance case, the approximation in the weak driving condition appears as the first order effect of our model.

Our model explains the possible frequencies in qubit Rabi oscillation, and also provides an alternative way to calculate the qubit evolution. This method is precise and valid in the regime where the RWA breaks down.

# Chapter 4

# Concluding Summary

The work presented in this thesis focuses on two topics: a qubit design that emphasizes the protection against different sources of noise, and qubit dynamics in the strong driving regime. These two topics are both aiming at the same goal: improve the efficiency of processing quantum information.

The design of the zero-pi qubit has shown its robustness against both charge noise and flux noise. Also, we have shown that the qubit has a large anharmonicity. These characters make the zero-pi qubit a promising candidate for scalable quantum computing. We derived an effective Hamiltonian of the qubit, which is a powerful model for further studies, especially for creating efficient and protected qubit gates and measurement protocols.

We have also presented the theoretical analysis of qubit evolution under strong driving conditions. The model successfully explains the qubit behavior in a concise form, and overcomes the failure of rotating-wave approximation, making it a natural way to describe the system under strong driving fields. The model can be applied to diagnose the accuracy in controlling the fast qubit evolution.

# APPENDICES

# Appendix A

# Born–Oppenheimer approximation

The Born-Oppenheimer (BO) approximation is a technique originally designed for electron-nuclear problem. The electron is much higher in speed than the nuclear. Thus the nuclear is considered fixed to electrons, and is interfered through an average but not the exact portion of the electron. The fundament that holds the approximation is that the distribution of the electron wavefunction is insensitive to the nuclear possible position. Generally, the BO approximation fits for any problem that involves a rapid part acts like an electron and an inertial part acts like a nuclear.

## A.1 Basis

We take a electron-nuclear system as the example. For simplicity we consider a one-dimensional model. The Hamiltonian has the form,

$$H = -\frac{\hbar^2}{2m}\frac{\partial^2}{\partial x^2} - \frac{\hbar^2}{2M}\frac{\partial^2}{\partial^2} + V(x, X), \tag{A.1}$$

where $\frac{\partial^2}{\partial x^2}$ and $\frac{\partial^2}{\partial X^2}$ are the partial derivatives on the position of the nuclear and the electron respectively. The nuclear mass $M$ is much larger than the electron mass $m$. The electron and the nuclear interacts through the potential $V(x, X)$. Then we select the basis $\{|\psi_{nk}\rangle\}$, which is defined as

$$|\psi_{nk}(x, X)\rangle = |F_{nk}(X)\rangle\,|f_k(x; X)\rangle\,. \tag{A.2}$$

Here, we decompose the state $|\psi_{nk}(x, X)\rangle$ into two parts: $|F_{nk}(x)\rangle$ and $|f_k(x; X)\rangle$. The state $|f_k(x; X)\rangle$ is the wavefunction of the electron with the position of nuclear as a parameter.

It is the $k^{\text{th}}$ eigenstate of the Hamiltonian,

$$H_{\text{electron}} = -\frac{\hbar^2}{2m}\frac{\partial^2}{\partial x^2} + V(x, X). \tag{A.3}$$

We denote the eigenenergy as $\mathcal{E}_{\|}(X)$, which is a function on $X$. The other component of $|\psi\rangle$ is $|F_{nk}(x)\rangle$, which is the wavefunction of the nuclear. It is the eigenstate of the Hamiltonian,

$$H_{\text{nuclear}} = -\frac{\hbar^2}{2M}\frac{\partial^2}{\partial X^2} + \mathcal{E}(X)_k, \tag{A.4}$$

with eigenenergy $E_{nk}$. The potential here, $\mathcal{E}_k(X)$, is the eigenenergy of $|f_k(x; X)\rangle$. We conclude that every state in the basis $\{|\psi_{nk}\rangle\}$ is associated with an energy $E_{nk}$. The state with lowest energy is the approximation to the ground state of the electron-nuclear system.

Now we show that the basis is an orthonormal complete basis. The orthonormality is straightforward:

$$\begin{aligned}
&\langle\psi_{ml}(x, X)|\psi_{nk}(x, X)\rangle \\
=&\iint F^*_{ml}(X)F_{nk}(X)f_l(x; X)f_k(x; X)dxdX \\
=&\int F^*_{ml}(X)F_{nk}(X)\delta_{l,k}dX \\
=&\delta_{mn}\delta_{lk}.
\end{aligned} \tag{A.5}$$

To prove the completeness, we choose an arbitrary state $|\varphi(x, X\rangle$, and show that the state can be expanded in terms of $|\psi(x, X)\rangle_{nk}$. Firstly, with any fixed $X = X'$, $\{f_k(x, X')\}$ is a complete basis because it is the eigenstates of the Hamiltonian. Thus can we expand $|\varphi(x, X)\rangle$ in terms of $f_k(x, X')$

$$\varphi(x, X) = \sum_k \alpha_k(X)f_k(x; X) \tag{A.6}$$

where $\alpha$ is the expansion coefficient which depends on $X$ and $k$. For any fixed subscript $k$, the set $|F_{nk}(X)\rangle$ is a complete basis on space $X$. Therefore we expand $\alpha_k$ as

$$\alpha_k(X) = \sum_n \beta_{nk}F_{nk}(X). \tag{A.7}$$

And we obtain the expansion of an arbitrary state $|\varphi\rangle\,(x, X) = \sum_{nk}\beta_{nk}F_{nk}(X)f_k(x; X)$.

## A.2 Perturbation term

The states $|\psi_{nk}(x,X)\rangle$ in the basis can be regard as the zero-th order approximation of the solution to the Hamiltonian. In this section we show the perturbation term. In the previous section we have proved that the basis is orthonormal and complete. Thus we can show the perturbation term in the basis by calculating $\Delta H = \langle\psi_{ml}| H |\psi_{nk}\rangle - \delta_{mn}\delta_{kl}E_{nk}$. We have

$$\begin{aligned}\langle\psi_{ml}| H |\psi_{nk}\rangle = \langle\psi_{ml}| \left(-\frac{\hbar^2}{2M}\frac{\partial^2}{\partial X^2} + H_{\text{electron}}\right) |\psi_{nk}\rangle \times \delta_{kl} \\ - \frac{\hbar^2}{2M}\left(2\langle F_m| \frac{\partial}{\partial X} |F_n\rangle \langle f_l| \frac{\partial}{\partial X} |f_k\rangle + \langle F_m| \left(\langle f_l| \frac{\partial^2}{\partial X^2} |f_k\rangle\right) |F_n\rangle\right). \quad \text{(A.8)}\end{aligned}$$

The first term equals $\delta_{mn}\delta_{kl}E_{nk}$. Thus the perturbation term is,

$$\Delta H = -\frac{\hbar^2}{2M}\left(2\langle F_m| \frac{\partial}{\partial X} |F_n\rangle \langle f_l| \frac{\partial}{\partial X} |f_k\rangle + \langle F_m| \left(\langle f_l| \frac{\partial^2}{\partial X^2} |f_k\rangle\right) |F_n\rangle\right). \quad \text{(A.9)}$$

# References


[1] Chris Mack et al. Fifty years of moore's law. *Semiconductor Manufacturing, IEEE Transactions on*, 24(2):202–207, 2011.

[2] Richard P Feynman. Simulating physics with computers. *International journal of theoretical physics*, 21(6/7):467–488, 1982.

[3] David Deutsch. Quantum theory, the church-turing principle and the universal quantum computer. In *Proceedings of the Royal Society of London A: Mathematical, Physical and Engineering Sciences*, volume 400, pages 97–117. The Royal Society, 1985.

[4] Michele Mosca. Quantum algorithms. In *Encyclopedia of Complexity and Systems Science*, pages 7088–7118. Springer, 2009.

[5] Michael A Nielsen and Isaac L Chuang. *Quantum computation and quantum information*. Cambridge university press, 2010.

[6] Thaddeus D Ladd, Fedor Jelezko, Raymond Laflamme, Yasunobu Nakamura, Christopher Monroe, and Jeremy L OBrien. Quantum computers. *Nature*, 464(7285):45–53, 2010.

[7] MH Devoret and RJ Schoelkopf. Superconducting circuits for quantum information: an outlook. *Science*, 339(6124):1169–1174, 2013.

[8] Mika A Sillanpää, Jae I Park, and Raymond W Simmonds. Coherent quantum state storage and transfer between two phase qubits via a resonant cavity. *Nature*, 449(7161):438–442, 2007.

[9] J-L Orgiazzi, C Deng, D Layden, R Marchildon, F Kitapli, F Shen, M Bal, FR Ong, and A Lupascu. Flux qubits in a planar circuit quantum electrodynamics architecture: quantum control and decoherence. *arXiv preprint arXiv:1407.1346*, 2014.

[10] Chen Wang, Yvonne Y Gao, Ioan M Pop, Uri Vool, Chris Axline, Teresa Brecht, Reinier W Heeres, Luigi Frunzio, Michel H Devoret, Gianluigi Catelani, et al. Measurement and control of quasiparticle dynamics in a superconducting qubit. *Nature communications*, 5, 2014.

[11] Jens Koch, M Yu Terri, Jay Gambetta, Andrew A Houck, DI Schuster, J Majer, Alexandre Blais, Michel H Devoret, Steven M Girvin, and Robert J Schoelkopf. Charge-insensitive qubit design derived from the cooper pair box. *Physical Review A*, 76(4):042319, 2007.

[12] Vladimir E Manucharyan, Jens Koch, Leonid I Glazman, and Michel H Devoret. Fluxonium: Single cooper-pair circuit free of charge offsets. *Science*, 326(5949):113–116, 2009.

[13] JQ You, Y Nakamura, and Franco Nori. Fast two-bit operations in inductively coupled flux qubits. *Physical Review B*, 71(2):024532, 2005.

[14] A Spörl, T Schulte-Herbrüggen, SJ Glaser, V Bergholm, MJ Storcz, J Ferber, and FK Wilhelm. Optimal control of coupled josephson qubits. *Physical Review A*, 75(1):012302, 2007.

[15] Christopher M Dawson and Michael A Nielsen. The solovay-kitaev algorithm. *arXiv preprint quant-ph/0505030*, 2005.

[16] Michael Tinkham. *Introduction to superconductivity*. Courier Corporation, 2012.

[17] Terry P Orlando and Kevin A Delin. *Foundations of applied superconductivity*, volume 224. Addison-Wesley Reading, MA, 1991.

[18] Alexandre Blais, Ren-Shou Huang, Andreas Wallraff, SM Girvin, and R Jun Schoelkopf. Cavity quantum electrodynamics for superconducting electrical circuits: An architecture for quantum computation. *Physical Review A*, 69(6):062320, 2004.

[19] Michel H Devoret, A Wallraff, and JM Martinis. Superconducting qubits: A short review. *arXiv preprint cond-mat/0411174*, 2004.

[20] Brian David Josephson. Possible new effects in superconductive tunnelling. *Physics letters*, 1(7):251–253, 1962.

[21] Yu Nakamura, Yu A Pashkin, and JS Tsai. Coherent control of macroscopic quantum states in a single-cooper-pair box. *Nature*, 398(6730):786–788, 1999.

[22] Vincent Bouchiat, D Vion, Ph Joyez, D Esteve, and MH Devoret. Quantum coherence with a single cooper pair. *Physica Scripta*, 1998(T76):165, 1998.

[23] TP Orlando, JE Mooij, Lin Tian, Caspar H van der Wal, LS Levitov, Seth Lloyd, and JJ Mazo. Superconducting persistent-current qubit. *Physical Review B*, 60(22):15398, 1999.

[24] I Chiorescu, Y Nakamura, CJP Ma Harmans, and JE Mooij. Coherent quantum dynamics of a superconducting flux qubit. *Science*, 299(5614):1869–1871, 2003.

[25] AA Houck, Jens Koch, MH Devoret, SM Girvin, and RJ Schoelkopf. Life after charge noise: recent results with transmon qubits. *Quantum Information Processing*, 8(2-3):105–115, 2009.

[26] JA Schreier, Andrew A Houck, Jens Koch, David I Schuster, BR Johnson, JM Chow, Jay M Gambetta, J Majer, L Frunzio, Michel H Devoret, et al. Suppressing charge noise decoherence in superconducting charge qubits. *Physical Review B*, 77(18):180502, 2008.

[27] F Motzoi, JM Gambetta, P Rebentrost, and Frank K Wilhelm. Simple pulses for elimination of leakage in weakly nonlinear qubits. *Physical review letters*, 103(11):110501, 2009.

[28] Peter H Handel. Quantum approach to 1 f noise. *Physical Review A*, 22(2):745, 1980.

[29] JQ You and Franco Nori. Superconducting circuits and quantum information. *arXiv preprint quant-ph/0601121*, 2006.

[30] Andreas Wallraff, David I Schuster, Alexandre Blais, L Frunzio, R-S Huang, J Majer, S Kumar, Steven M Girvin, and Robert J Schoelkopf. Strong coupling of a single photon to a superconducting qubit using circuit quantum electrodynamics. *Nature*, 431(7005):162–167, 2004.

[31] F Yoshihara, K Harrabi, AO Niskanen, Y Nakamura, and JS Tsai. Decoherence of flux qubits due to 1/f flux noise. *Physical review letters*, 97(16):167001, 2006.

[32] Roger H Koch, David P DiVincenzo, and John Clarke. Model for 1/f flux noise in squids and qubits. *Physical review letters*, 98(26):267003, 2007.

[33] Alexei Kitaev. Protected qubit based on a superconducting current mirror. *arXiv preprint cond-mat/0609441*, 2006.

[34] Mahn-Soo Choi, MY Choi, Taeseung Choi, and Sung-Ik Lee. Cotunneling transport and quantum phase transitions in coupled josephson-junction chains with charge frustration. *Physical review letters*, 81(19):4240, 1998.

[35] Joshua M Dempster, Bo Fu, David G Ferguson, DI Schuster, and Jens Koch. Understanding degenerate ground states of a protected quantum circuit in the presence of disorder. *Physical Review B*, 90(9):094518, 2014.

[36] Peter Brooks, Alexei Kitaev, and John Preskill. Protected gates for superconducting qubits. *Physical Review A*, 87(5):052306, 2013.

[37] Uri Vool, Ioan M Pop, Katrina Sliwa, Baleegh Abdo, Chen Wang, Teresa Brecht, Yvonne Y Gao, Shyam Shankar, Michael Hatridge, Gianluigi Catelani, et al. Nonpoissonian quantum jumps of a fluxonium qubit due to quasiparticle excitations. *Physical review letters*, 113(24):247001, 2014.

[38] Samuele Spilla, Fabian Hassler, Anna Napoli, and Janine Splettstoesser. Dephasing due to quasiparticle tunneling in fluxonium qubits: a phenomenological approach. *arXiv preprint arXiv:1503.04489*, 2015.

[39] C David Sherrill. The born-oppenheimer approximation. *School of Chemistry and Biochemistry, Georgia Institute of Technology*, 2005.

[40] Jun John Sakurai and Jim J Napolitano. *Modern quantum mechanics*, pages 355–363. Pearson Higher Ed, 2014.

[41] FAM De Oliveira, MS Kim, PL Knight, and V Buek. Properties of displaced number states. *Physical Review A*, 41(5):2645, 1990.

[42] Eric W Weisstein. Laguerre polynomial. *MathWorld–A Wolfram Web Resource, http://mathworld.wolfram.com/LaguerrePolynomial.html*.

[43] Stephen Wolfram. *Mathematica: a system for doing mathematics by computer*. Addison Wesley Longman Publishing Co., Inc., 1991.

[44] Eric W Weisstein. Incomplete gamma function. *MathWorld–A Wolfram Web Resource, http://mathworld.wolfram.com/IncompleteGammaFunction.html*.

[45] Frank WJ Olver. *NIST handbook of mathematical functions*. Cambridge University Press, 2010.

[46] NW Ashcroft and ND Mermin. Solid state physics (saunders college)(1976). pages 175–190.

[47] Charles Kittel. *Introduction to solid state physics*, chapter 7. Wiley, 2005.

[48] Jun John Sakurai and Jim J Napolitano. *Modern quantum mechanics*, pages 110–116. Pearson Higher Ed, 2014.

[49] John M Martinis and RH Ono. Fabrication of ultrasmall nb-alox-nb josephson tunnel junctions. *Applied physics letters*, 57(6):629–631, 1990.

[50] M Maezawa, M Aoyagi, H Nakagawa, I Kurosawa, and S Takada. Specific capacitance of nb/alox/nb josephson junctions with critical current densities in the range of 0.1–18 ka/cm2. *Applied physics letters*, 66(16):2134–2136, 1995.

[51] Hanhee Paik, DI Schuster, Lev S Bishop, G Kirchmair, G Catelani, AP Sears, BR Johnson, MJ Reagor, L Frunzio, LI Glazman, et al. Observation of high coherence in josephson junction qubits measured in a three-dimensional circuit qed architecture. *Physical Review Letters*, 107(24):240501, 2011.

[52] Yuriy Makhlin and Alexander Shnirman. Dephasing of solid-state qubits at optimal points. *arXiv preprint cond-mat/0308297*, 2003.

[53] Daniel Sank, R Barends, Radoslaw C Bialczak, Yu Chen, J Kelly, M Lenander, E Lucero, Matteo Mariantoni, A Megrant, M Neeley, et al. Flux noise probed with real time qubit tomography in a josephson phase qubit. *Physical review letters*, 109(6):067001, 2012.

[54] G Ithier, E Collin, P Joyez, PJ Meeson, D Vion, D Esteve, F Chiarello, A Shnirman, Yu Makhlin, Josef Schriefl, et al. Decoherence in a superconducting quantum bit circuit. *Physical Review B*, 72(13):134519, 2005.

[55] Edwin T Jaynes and Frederick W Cummings. Comparison of quantum and semiclassical radiation theories with application to the beam maser. *Proceedings of the IEEE*, 51(1):89–109, 1963.

[56] Jon H Shirley. Solution of the schrödinger equation with a hamiltonian periodic in time. *Physical Review*, 138(4B):B979, 1965.